

Neutron Yield Measurement of ^{nat}C Neutron Yield Measurement of $^{nat}\text{C}(d,n)$ Reaction for Radioisotopes Production and Development of PHITSbased Dosimetry System for Medical Application

パトワリ, エムディ, カウサー, アハメッド

<https://hdl.handle.net/2324/4110539>

出版情報 : Kyushu University, 2020, 博士 (工学), 課程博士
バージョン :
権利関係 :

Neutron Yield Measurement of $^{nat}\text{C}(d,n)$ Reaction
for Radioisotopes Production and Development
of PHITS-based Dosimetry System
for Medical Application

Md Kawchar Ahmed PATWARY

Department of Advanced Energy Engineering Science (AEES)
Interdisciplinary Graduate School of Engineering Sciences (IGSES)
Kyushu University, JAPAN

2020

*Dedicated to my beloved **Parents** and dear **Professors***

Tadahiro **KIN**

Yukinobu **WATANABE**

Abstract

In recent years, intensive accelerator-based neutron sources with deuteron-induced reactions have been proposed for the production of medical radioisotopes (RIs). We focused on neutrons generated via the $C(d,n)$ reactions, because they have advantages of neutron intensity and energy adjustability. To estimate the production amount and purity of produced RIs, accurate double-differential thick-target neutron yield (DDTTNY) is necessary. For the RI productions, deuteron having a few to 50 MeV is used to generate the neutrons, but experimental DDTNYS of the $C(d,n)$ reaction in the range have not been measured systematically. Moreover, in the accelerator-based RI production method, new RIs are proposing for diagnosis and therapy. To avoid from negative effects of normal organ/tissue during the diagnosis or therapy, accurate prediction of absorbed dose is very important. External and internal doses of inhalation and ingestion can be precisely predicted by using conventional models or the latest Monte Carlo based method. However, the precise dose calculation method of “administrated medical RIs” has not been established yet. Nowadays, the dose prediction is given by Monte Carlo calculations using models of the human body. Hence, the calculation of absorbed doses requires the precise human body geometry. Also, there is no established prediction method of the radiation dose of the clinical staff and the patient’s family from the administrated patient. The dose can be measured by an expensive survey meter for the clinical staff, but after checking out of the hospital there is no way to measure the dose of the patient’s family.

To overcome the above situations, this thesis aimed two purposes: First, DDTNYS of the $C(d,n)$ reaction for 12, 20 and 30 MeV deuteron were measured, because around 25 MeV, available experimental data are lacked even though the energy is considered promising for some medical RIs production, such as ^{64}Cu . Furthermore, the reproducibility of DEURACS was surveyed in the measured region to reveal the reliability of the code. Then, the DDTNYS were used for estimation of RI production amount and purity of two applications, ^{132}Cs for environmental tracer and ^{47}Sc for medical use. Second, because some new RIs production is considered for the accelerator-based method, a universal dose calculation system is proposed. In the calculation system, Monte Carlo simulation code, PHITS is used with realistic voxel phantom, JF-103, and JM-103, and the dose of an administrated patient is derived by using the latest ICRP recommendations. Furthermore, to establish a calculation method of clinical staff and patient’s family dose, gamma-ray sources from administrated patients are recorded. The source can be used in Monte Carlo simulation code such as PHITS or GEANT4, to calculate the dose of them.

DDTTNY of the $^{nat}\text{C}(d,n)$ reaction at the incident energies of 12, 20, and 30 MeV were measured by using the multiple-foils activation method. Accelerated deuterons were bombarded on a ^{nat}C ($\varnothing 20$ mm, 4 mm^l) target so that neutrons were generated via the (d,n) reactions and irradiated multiple foils made of ^{nat}Ni , ^{nat}In , ^{27}Al , ^{59}Co , and ^{93}Nb immediately. The neutron energy spectra were unfolded by the GRAVEL code to derive the DDTNYS and were compared with the DEURACS calculations which showed that the DEURACS calculation reproduces the experimental angular distributions for 0° to 45° . By the inclusion of other experimental data, the systematics were derived for prediction of differential neutron yields at 0° and total neutron yield per incident deuteron over the wide range of deuteron energy. It is showed that this research can full fill the lack of nuclear data within the deuteron energy up to 30 MeV.

The deuteron accelerator-based neutron method was applied to produce RI. At first, a tracer ^{132}Cs ($T_{1/2} = 6.5\text{d}$) production experiment was conducted. This is produced by irradiating a 12-g of Cs_2CO_3 sample using accelerator-based neutrons by $1.2\ \mu\text{A}$ 30 MeV deuterons. The $^{133}\text{Cs}(n,2n)^{132}\text{Cs}$ reaction, initiated by irradiating 30 MeV deuterons on a thick $^{\text{nat}}\text{C}$ ($\varnothing 40\text{ mm}$, 4 mm^t), yielded 102.2 kBq/g of ^{132}Cs with a radioactive purity of 98% after 2-hour irradiation. A feasibility study of the produced ^{132}Cs of cesium absorptions to andosol, haplic fluvisol, and gleyic fluvisol soil particles finds almost 100% of the ^{132}Cs was distributed within 40 mm from the surfaces of all soil samples. It is concluding that ^{132}Cs can replace ^{137}Cs ($T_{1/2} = 30\text{y}$) as an environmental tracer. On the other hand, the production yields and purities of ^{47}Sc ($T_{1/2} = 3.5\text{ d}$), was estimated by PHITS using the measured DDTNYS at 12, 20, and 30 MeV deuterons. When irradiating 5-g of ^{47}Ti powder for 5 hours, ^{47}Sc were produced via $^{47}\text{Ti}(n,p)$ reaction and yielded a maximum $4.59 \times 10^{-5}\text{ MBq/g/}\mu\text{C}$ for neutron yields of 30 MeV deuterons. Based on the results from this proof-of-concept study, ^{47}Sc has the potentiality to produce in a suitable quality for theranostic clinical applications.

Finally, a new radiation dose calculation has been successfully implemented for patient dosimetry in nuclear medicine. The new PHITS-based computation was adjusted to a set of voxelized phantoms JM-103 and JF-103 which has completely different anatomical and physiological characteristics than the ICRP/ICRU reference adults, AM and AF. This improved dose calculation has been applied to investigate the absorbed dose for organ/tissue for internal dosimetry, the ambient dose equivalent, $H^*(10)$ for external dosimetry, and dosimetry in occupational exposure to an external source of radiation. In particular, for a theranostic RI ^{47}Sc , the absorbed doses are different than the similar calculation with AM and AF. This suggested that our developed dosimetry calculations can be recommended for the Japanese averages and also for the Asian personal. Moreover, together with the adoption of the new voxel phantoms, the updated definition of the sex-averaged effective dose has been implemented from ICRP 2007 recommendations. The accuracy of the calculations was compared with those determined by the ICRP.

Keywords: Accelerator-based neutron, DDTNYS, medical RIs, nuclear medicine, ICRP/ICRU adult reference computational phantoms, JM-103 and JF-103, radiation dosimetry, Monte Carlo simulation, PHITS, absorbed dose, ICRP 2007 recommendations, effective dose, $H^*(10)$.

Contents

List of Figures	iii
List of Tables	vii
Thesis Synopsis.....	xi
1. Introduction.....	1
1.1 Background	1
1.1.1 Accelerator-based neutron source	2
1.1.2 Experimental data availability of deuteron-induced nuclear reactions	4
1.1.3 Theoretical approach to deuteron-induced nuclear reactions	5
1.1.4 DDTTNY measurement method.....	5
1.1.5 Dose calculation	6
1.1.6 General features of the ICRP/ICRU adult reference computational voxel phantoms	7
1.1.7 PHITS-based Japanese voxel phantoms.....	9
1.2 Motivations and Objectives.....	11
1.3 Thesis Structure.....	12
2. Thick Target Neutron Yields of Accelerator-Based Neutron Source.....	14
2.1 Experiment.....	15
2.1.1 Irradiation conditions	16
2.1.2 γ -ray measurement of irradiated sample	18
2.2 Data Analysis	19
2.2.1 Activity determination at the end of irradiation.....	19
2.2.2 Derivation of nuclide production.....	21
2.2.3 Production rate.....	21
2.2.4 Unfolding process.....	23
2.3 Results and Discussion	25
2.3.1 Double-differential thick-target neutron yield.....	26
2.3.2 Systematic Uncertainty Evaluation.....	27
2.3.3 Angular differential neutron yields.....	30
2.3.4 Deuteron energy dependency of total neutron yield	34
2.4 Conclusion	37
3. Radioisotope Production by Accelerator-based Neutrons	38
A. Production of ^{132}Cs environmental tracer.....	38
A. 3.1 Background.....	38
A. 3.2 ^{132}Cs production experiment.....	41
A. 3.3 Feasibility study of ^{132}Cs tracer for environmental study.....	46
A. 3.4 Summary	48
B. Application to Medical Radioisotope Production.....	48
B. 3.1 Background.....	48
B. 3.2 Production of radioisotopes with accelerator neutrons by deuterons	49
B. 3.3 Production amount and purities of radioisotopes	50
B. 3.4 Summary.....	58

3.2 Conclusion	59
4. Radiation Dose to Patient	60
4.1 Dose quantities in radiological protection.....	62
4.2 Internal dose calculations.....	63
4.2.1 Anatomical models	65
4.2.2 Japanese reference adult phantoms	67
4.2.3 PHITS simulation for dose estimation	69
4.2.4 Absorbed doses to organs and tissues	71
4.3 Biological effects and effective dose calculations.....	75
4.4 Dose coefficients for intravenous administration of radiopharmaceuticals	82
4.5 Uncertainty in internal dosimetry	94
4.6 Conclusion	95
5. Radiation Dose from Patient.....	96
5.1 Operational quantities for area monitoring	97
5.2 $H^*(10)$ for safety issues: a PHITS study.....	98
5.3 Universal radiation source calculation of RI administrated patient: “dump” file..	101
5.3.1 Reading ‘dump files’ for $H^*(10)$ calculation	104
5.4 Conclusion	106
6. Dosimetry of Occupational Exposure from ^{132}Cs	107
6.1 Materials and methods.....	108
6.1.1 Source of external exposure	108
6.1.2 Dosimetric methodology and reference phantoms.....	110
6.2 Results of dose estimations	110
6.3 Conclusion	114
7. Summary and Future Outlook.....	115
7.1 Summary and Conclusions.....	115
7.2 Suggestions for Future Work	119
References	121
Acknowledgements	140

List of Figures

<u>Figure</u>	<u>Page</u>
1.1 Schematic diagram of neutron production by deuteron-induced reaction. -----	3
1.2 Number of experimental data of deuteron incident TTNY published in EXFOR. (Figure is cited from ref. [30].) -----	4
1.3 Coronal and sagittal images of (a) the male (b) the female reference computational phantom published in the ICRP Publication 110. [44] -----	9
2.1 An outline of the JAEA tandem accelerator system and beamline facility, excerpted from ref. [53]. -----	15
2.2 (a) Photograph and (b) schematic view of the experimental setup.	17
2.3 The production rate for the interesting reactions (figure shows the production rate for the reactions produced by 30 MeV incident deuteron energy and for multiple-foils position at 0°). -----	22
2.4 Initial guess neutron spectrum calculated with DEURACS. For incident deuteron energy (a) 12 MeV, (b) 20 MeV, and (c) 30 MeV.	24
2.5 Relationship between the number of iteration and χ^2 . This example figure was determined for 30 MeV incident deuteron energy and at 10° of multiple-foil position. In this case, the number of iterations has been selected at the point where the curve tends to progress smoothly. This process of selection suggested that the number of iterations should be '10' in the case mentioned for this figure. -----	25
2.6 Measured DDTTNYs from thick ^{nat} C target, incident by (a) 12 MeV and compared with the published data of Weaver <i>et al.</i> at 11.99 MeV of deuteron [61], (b) 20 MeV and compared with the published data of Weaver <i>et al.</i> at 18.09 MeV of deuteron [61], (c) 30 MeV deuteron and compared with the published data of Shin <i>et al.</i> at 33 MeV of deuteron [62]. -----	28
2.7 Calculation/Experiment of number of atoms. -----	29

2.8	Comparison between the unfolding neutron spectrum and the initial guess neutron spectrum calculated with DEURACS at 12, 20, and 30 MeV deuteron energies and neutron emission angle at 0°. -----	30
2.9	Angular distribution of neutron yields for 12 MeV, 20 MeV, and 30 MeV deuterons. -----	31
2.10	Angle-differential neutron yield as a function of angle to beam axis for different neutron energy ranges for (a) 12 MeV, (b) 20 MeV, and (c) 30 MeV deuterons. -----	32
2.11	Energy-integrated thick target neutron yield as a function of incident deuteron energy. For minimum neutron energy 2 MeV, the yield was calculated at an angle 0° to the beam axis, only. -----	34
2.12	Neutron yields for deuteron-induced reactions on ^{nat} C target up to $\theta = 45^\circ$ for various deuteron energies, representing the integrals of our work of 12, 20, and 30 MeV (red closed circle) and a few others from the literatures for carbon target. The fitting curve (blue curve) is only to guide the eye. -----	35
3.1	Decay schemes of (a) ¹³⁷ Cs and (b) ¹³² Cs. Due to its short half-life, ¹³² Cs is a promising tracer of ¹³⁷ Cs. -----	40
3.2	Neutron-induced reaction cross-section of ¹³³ Cs. The threshold energy of the ¹³² Cs production cross-section is approximately 9 MeV; from that point, the cross-section increases with neutron energy to its maximum at approximately 17 MeV. -----	41
3.3	Schematic view of 930 AVF cyclotron and it's 32-course facilities in the CYRIC. (Excerpted from ref. [84].) -----	42
3.4	(a) Carbon target, and (b) photograph and schematic view of the irradiation setup. -----	44
3.5	γ -ray spectrum of the Cs ₂ CO ₃ sample irradiated with accelerator-based neutrons. -----	45
3.6	Measuring the vertical distribution of ¹³² Cs activity in soil samples. Distributions were measured in three types of soil samples: haplic fluvisol, andosol, and gleyic fluvisol soil. -----	46
3.7	Vertical distributions of ¹³² Cs activity in the three soil samples. The measured points are the relative activities of ¹³² Cs at the respective soil depths. The activity distribution remains steady after 40 mm. -----	47
3.8	Schematic diagram of medical RI production by accelerator-based neutrons method with deuterons. -----	50

3.9	Nuclear data for production of ^{47}Sc from (a) ^{46}Ca via $^{46}\text{Ca}(n,\gamma)^{47}\text{Ca} \rightarrow ^{47}\text{Sc}$ and (b) from ^{47}Ti via $^{47}\text{Ti}(n,p)^{47}\text{Sc}$. -----	52
3.10	Excitation function of neutron-induced reactions on ^{47}Ti . The red line shows the production reaction of ^{47}Sc . Green arrow indicates the maximum production cross-section point for the corresponding neutron energy approximately 14 MeV. The experimental values of $^{47}\text{Ti}(n,p)^{47}\text{Sc}$ cross-section were taken from the Experimental Nuclear Reaction Data library (EXFOR) [29]. -----	53
3.11	Schematic diagram of the ^{47}Ti target irradiation system used in the simulation. -----	55
3.12	Dependence of ^{47}Sc production, radioactive purity, and isotope purity on incident deuteron energy. -----	58
4.1	Schematic of RIT. RIT delivers radiation directly to the tumor-specific antigen of a specific cancer type. (Excerpted from ref. [122].) -----	60
4.2	Radiation dose quantities define by the ICRP and the ICRU. -----	63
4.3	3D anterior view of the whole body of the JM-103 and JF-103. ---	70
4.4	A schematic diagram for the internal radiation dose calculation with PHITS simulation. -----	72
4.5	Effective dose coefficients (mSv/MBq) for clinically relevant and frequently used radiopharmaceuticals with radiolabeled (a) ^{18}F and (b) $^{99\text{m}}\text{Tc}$. -----	81
5.1	An illustration how a patient can be a source of external exposure to hospital staffs or take carers after the nuclear medicine treatment; (a) administration of radiopharmaceuticals to the patient for the treatment of any specific disease, (b) biodistribution of radiopharmaceuticals in the whole body of the patient after a certain period, (c) as time goes, patient acts as a source of external radiation exposure, and (d) emission of γ -rays from the patient body parts. -----	100
5.2	Information of the particles can be dumped when crossing a cylindrical peripheral enclosing surface from the patient after nuclear medicine applications. -----	102
5.3	Particle information dumped in a file. This information was recorded in the case of ^{47}Sc therapy and showing as an example from all other 'dump' files. -----	103

5.4	Schematic view of the geometry of PHITS simulation for $H^*(10)$ calculation inside an ICRU sphere. -----	104
6.1	Schematic view of the demonstration of how a researcher exposed to an external radiation source during handling radioactive substances for research purposes. -----	109

List of Tables

<u>Table</u>	<u>Page</u>
1.1 Main characteristics of the AM and AF computational phantoms. [44] -----	8
1.2 Masses of selected organs and tissues of the JM-103, JF-103 [47], AM and AF phantoms [44], and the averages of adult Japanese [48]. Values in parentheses are the ratios of masses of JM-103, JF-103, AM, and AF to averages of adult Japanese. -----	10
2.1 Properties of the activation foils used in the experiment. These samples are available commercially and collected from the Nilako corporation [54]. -----	18
2.2 A detailed list of the number of atoms produced at the EOI. -----	20
2.3 Reaction and energy threshold of the reaction. -----	22
2.4 Total neutron yields of energy ($= E_n$) higher than 4 MeV per 100 incident deuterons, ($n/100d$), and the integral of the yield per steradian per 100 incident deuterons, ($n/sr/100d$), and for maximum $\theta = 45^\circ$ in our measurements. -----	36
3.1 Simulation results of ^{47}Sc production yield from 5 g of ^{47}Ti target.	55
3.2 Production amount of $^{46,47}\text{Sc}$ and ^{47}Sc radioactive purity at each incident deuteron energy. -----	56
3.3 Production amount of $^{45,46,47}\text{Sc}$ isotopes and isotopic purity of ^{47}Sc at each incident deuteron energy. ‘ - ‘means ^{45}Sc cannot produce at 12 MeV incident deuteron energy. -----	57
4.1 A comparative scenario between the main physical characteristics of JM-103 & JF-103 developed at JAEA [47] and the adult male (AM) & adult female (AF) reference computational phantoms developed by the ICRP/ICRU [44]. -----	68

4.2	Absorbed doses (mGy/MBq) and the effective dose (mSv/MBq) per administered activity of theranostic radionuclide ^{47}Sc (physical half-life, $T_{1/2} = 3.3492$ d) for the proposed internal dosimetry calculation method with the Japanese phantoms JM-103 and JF-103. Results obtained with ICRP/ICRU computational reference phantoms are also given. ‘–’ and ‘×’ indicating the value of absorbed dose cannot calculate due to sex dependency and in the estimation method, respectively. -----	73
4.3	Tissue weighting factors w_T for different organs [46]. -----	76
4.4	The effective dose from emergent medical radionuclide used in imaging and/or therapeutic nuclear medicine and the difference in % concerning the effective dose presented in the ICRP publications. ‘×’ indicates that the calculated effective dose cannot compare to ICRP reference value because there is no published data. -----	78
4.5	Values of E/A_0 generated using developed calculation in the present study and those generated using DCAL [167], and ratios of E/A_0 for intravenous administration of ^{18}F and $^{99\text{m}}\text{Tc}$ RI. -----	81
4.6	Absorbed dose coefficients (mGy/MBq) in different organs/tissues for positron emitter ^{18}F (physical half-life = 1.83 h, [56]). ICRP published values of absorbed dose coefficients (mGy/MBq) for 2- ^{18}F -fluoro-2-deoxy-D-glucose (^{18}F -FDG) from the ICRP Publication 128 [165] have been noted for comparing to the values obtained in this research. ‘-’ means absorbed dose in the respective organs cannot be obtained due to the physiological characteristic of the reference phantom. -----	83
4.7	Absorbed dose coefficients (mGy/MBq) in different organs/tissues for positron emitter ^{68}Ga (physical half-life = 1.129 h [56]). ^{68}Ga is used mostly for ^{68}Ga -PSMA-PET/CT imaging. ICRP published values of absorbed dose coefficients (mGy/MBq) for ^{68}Ga -labelled ethylenediaminetetraacetic acid (^{68}Ga -EDTA) from the ICRP Publication 128 [165] have been noted for comparing to the values obtained in this research. ‘-’ means absorbed dose in the respective organs cannot be obtained due to the physiological characteristic of the reference phantom. -----	84

- 4.8 Absorbed dose coefficients (mGy/MBq) for ^{99m}Tc (physical half-life = 6.0072 h [56]). ICRP published values of absorbed dose coefficients (mGy/MBq) for ^{99m}Tc -labelled methoxy-isobutyl-isonitrile (^{99m}Tc -MIBI- Resting subject and ^{99m}Tc -MIBI-Exercise) from the ICRP Publication 128 [165] have been noted for comparing to the values obtained in this research. ‘-’ means absorbed dose in the respective organs cannot be obtained due to the physiological characteristic of the reference phantom. ----- 85
- 4.9 Absorbed dose coefficients (mGy/MBq) for theranostic ^{64}Cu (physical half-life = 12.701 h [56]). ICRP published values of absorbed dose coefficients (mGy/MBq) for ^{64}Cu -Ion from the ICRP Publication 53 [169] have been noted for comparing to the values obtained in this research. ‘-’ means absorbed dose in the respective organs cannot be obtained due to the physiological characteristic of the reference phantom. ‘×’ means absorbed dose in the respective organs is not available in the ICRP publication. 86
- 4.10 Absorbed dose coefficients (mGy/MBq) for therapeutic RI ^{67}Cu (physical half-life = 2.58 d, β^- decay [56]). ICRP published values of absorbed dose coefficients (mGy/MBq) for ^{67}Cu -Ion from the ICRP Publication 53 [169] have been noted for comparing to the values obtained in this research. ‘-’ means absorbed dose in the respective organs cannot be obtained due to the physiological characteristic of the reference phantom. ‘×’ means absorbed dose in the respective organs is not available in the ICRP publication. 87
- 4.11 Absorbed dose coefficients (mGy/MBq) for ^{123}I (physical half-life = 13.2235 h [56]). ICRP published values of absorbed dose coefficients (mGy/MBq) for ^{123}I -Iodide (Thyroid, high uptake) from the ICRP Publication 128 [165] have been noted for comparing to the values obtained in this research. ‘-’ means absorbed dose in the respective organs cannot be obtained due to the physiological characteristic of the reference phantom. ----- 88
- 4.12 Absorbed dose coefficients (mGy/MBq) for theranostic RI ^{131}I (physical half-life = 8.0252 d [56]). ICRP published values of absorbed dose coefficients (mGy/MBq) for ^{131}I -Iodide (Thyroid uptake 55%) from the ICRP Publication 53 [169] have been noted for comparing to the values obtained in this research. ‘-’ means absorbed dose in the respective organs cannot be obtained due to the physiological characteristic of the reference phantom. ‘×’ means absorbed dose in the respective organs is not available in the ICRP publication. ----- 89

4.13	Absorbed dose coefficients (mGy/MBq) for ^{90}Y (physical half-life = 2.67 d [56]). ^{90}Y is using in radioembolization (or selective internal radiation therapy) for primary or metastatic liver cancer treatment [180]. ‘-’ means absorbed dose in the respective organs cannot be obtained due to the physiological characteristic of the reference phantom. -----	90
4.14	Absorbed dose coefficients (mGy/MBq) for ^{152}Tb (physical half-life = 17.5 h [56]). ^{152}Tb is identified for PET or SPECT imaging and even it can combine to other terbium RIs (<i>e.g.</i> , ^{161}Tb ; β^- decay) for the potential theranostic application in nuclear medicine. Müller <i>et al.</i> showed the first-in-human application of ^{152}Tb -PSMA-617 for PET/CT imaging of prostate cancer [181]. ‘-’ means absorbed dose in the respective organs cannot be obtained due to the physiological characteristic of the reference phantom. -----	91
4.15	Absorbed dose coefficients (mGy/MBq) for ^{161}Tb (physical half-life = 6.89 d [56]). ^{161}Tb is an interesting RI for cancer treatment, showing an alternative to the clinically applied conventional RI ^{177}Lu (physical half-life = 6.647 d, β^- or Auger electron decay [56]) for PSMA-targeted radionuclide therapy of prostate cancer [182] [183]. ‘-’ means absorbed dose in the respective organs cannot be obtained due to the physiological characteristic of the reference phantom. -----	92
4.16	Absorbed dose coefficients (mGy/MBq) for ^{166}Ho (physical half-life = 1.12 d, β^- decay [56]). The various therapeutic applications of ^{166}Ho is reviewed by Klaassen <i>et al.</i> [184]. Among them, ^{166}Ho -microspheres ($^{166}\text{HoMS}$) shows prominent to treat for patients with locoregional recurrences of head and neck squamous cell carcinoma (HNSCC) [185]. ‘-’ means absorbed dose in the respective organs cannot be obtained due to the physiological characteristic of the reference phantom. -----	93
5.1	ICRP Publication 60 & 103 and IAEA recommended annual dose limits. -----	97
5.2	PHITS simulated ambient dose equivalent, $H^*(10)$, for the area or workplace monitoring for safety issues from further radiation exposure. -----	105
6.1	Absorbed dose to organ/tissue of a person for an occupational exposure of ^{132}Cs . This physical quantity can proceed to calculate the protection quantity, ‘the sex-averaged effective dose’ based on ICRP Publication 103. ‘-’ means absorbed dose in the respective organs cannot be obtained due to the physiological characteristic of the reference phantom. -----	112

Thesis Synopsis

In recent years, intensive accelerator-based neutrons sources with deuteron-induced reactions have been proposed for various applications, especially, production of medical radioisotopes (RIs). We focused on neutrons generated via the $C(d,n)$ reactions, because they have advantages of neutron intensity and energy adjustability. Moreover, because high energy neutrons to be applied for RIs productions are strongly focused on forward emission angle, a simple irradiation system having a low quantity of shielding is possible in actual applications. To estimate the production amount and purity of produced RIs, accurate double-differential thick-target neutron yield (DDTTNY) is necessary. It is also required to design shielding of the irradiation system. For the RI productions, deuteron having a few to 50 MeV is used to generate the neutrons, but experimental DDTNYS of the $C(d,n)$ reaction in the range have not been measured systematically. Besides, the lack of experimental data leads to the uncertainty of the production amount and purity of produced RIs. For the RI production applications, neutron energy adjustment is promising to reduce byproducts' contribution, thus the uncertainty is sometimes cause of difficulty of optimization of deuteron energy for the neutron energy adjustment.

In the accelerator-based RI production method, new RIs are proposing for medical use for diagnosis and therapy. To avoid from negative effects of normal organs and tissues during the diagnosis or therapy, accurate prediction of absorbed dose is very important. External radiation doses like X-ray, CT, or IMRT therapy can be precisely predicted by using conventional models or the latest Monte Carlo based method, and also the internal dose of inhalation and ingestion can be determined by using dose coefficients listed in ICRP Publication 119. In contrast to that, however, the precise dose calculation method of "administrated medical RIs" has not been established yet. Nowadays, the dose prediction is given by Monte Carlo calculations using the ICRP/ICRU recommended AM and AF phantoms which are based on the organ masses according to the ICRP Publication 89 having statistics for Western Europeans and North Americans. In other words, because the phantoms are different from Asian reference personals, we cannot obtain precise dose prediction by using these estimations. Also, there is no established prediction method of the radiation dose of the clinical staff and the patient's family from the administrated patient. The dose can be measured by an expensive survey meter for the clinical staff, but after checking out of the hospital there is no way to measure the dose of the patient's family.

To overcome the above situations, this thesis has two purposes: First, DDTNYS of the $C(d,n)$ reaction for 12, 20 and 30 MeV deuteron were measured, because around 25 MeV, available experimental data are lacked even though the energy is considered promising for some medical RIs production, such as ^{64}Cu . Furthermore, the reproducibility of DEURACS was surveyed in the measured region to confirm the reliability of the code. Then, the DDTNYS were used for estimation of RI production amount and purity of two applications, ^{132}Cs for environmental tracer and ^{47}Sc for medical use. Second, because some new RIs production is considered for the accelerator-based neutron method, a universal dose calculation system is proposed. In the calculation system, Monte Carlo simulation code, PHITS is used with realistic voxel phantom, JF-103, and JM-103, and the dose of an administrated patient is derived by using the latest ICRP recommendations. Furthermore, to establish a calculation method of clinical staff and patient's family dose, γ -ray sources from administrated patients are recorded. The

source can be used in Monte Carlo simulation code such as PHITS or GEANT4, to predict the dose of them.

This thesis introduces the background of the study and motivation of this work in the first chapter.

After that, Chapter 2 is devoted to experimental measurements of the thick-target neutron yield by using deuteron induced accelerator-based neutron source and the multiple-foil activation method. The experiments were conducted at the tandem accelerator facility of the Japan Atomic Energy Agency. Deuterons having 12, 20, or 30 MeV kinetic energy were separately incident on a thick target neutron converter made of ^{nat}C ($\varnothing 20$ mm, 4 mm^t). So that neutrons were generated via the (*d,n*) reactions. Multiple-foil made of ^{nat}Ni , ^{nat}In , ^{27}Al , ^{59}Co , and ^{93}Nb were placed at 0°, 10°, 20°, 30°, and 45° from the deuteron beam direction and were exposed to neutron irradiation for different time durations with different beam currents. Neutron spectra were unfolded for each incident deuteron energy and each neutron emission angle by using GRAVEL code. The results were compared with the theoretical calculations with DEURACS, and they showed that the DEURACS calculation reproduces the experimental DDTNYS at 12, 20, and 30 MeV of deuteron energy from 0° to 45° of neutron emission angle. Results showed that DEURACS can be used to interpolate the lacking experimental DDTNY. Moreover, a detailed comparison of yields to other available published data are also explained in this chapter. It is showed that this research can full fill the lack of nuclear data within the mentioned deuteron energy range.

In Chapter 3, the application of accelerator-based neutron to RIs production is discussed. This chapter is categorized into two parts. At first, an environmental tracer ^{132}Cs ($T_{1/2} = 6.5$ d) production experiment is described. This is produced by irradiating a 12-g of Cs_2CO_3 sample using accelerator-based neutrons by 1.2 μA of 30-MeV deuterons. The ^{132}Cs production experiment was conducted at the Cyclotron and Radioisotopes Center (CYRIC) of Tohoku University, Japan. The $^{133}\text{Cs}(n,2n)^{132}\text{Cs}$ reaction, initiated by irradiating 30 MeV deuterons on a thick ^{nat}C ($\varnothing 40$ mm, 4 mm^t), yielded 102.2 kBq/g of ^{132}Cs with a radioactive purity of 98% after 2-hour irradiation. Also, a feasibility study on andosol, haplic fluvisol, and gleyic fluvisol soil explains that ^{132}Cs can be used as an alternative tracer of ^{137}Cs ($T_{1/2} = 30\text{y}$) for environmental radioactive monitoring. Moreover, the production yields and purities of an emergent theranostic medical RI, ^{47}Sc is estimated by PHITS simulation by using measured DDTNYS of 12, 20, and 30 MeV deuterons. When irradiating 5 g of ^{47}Ti powder for 5 hours, ^{47}Sc were produced via $^{47}\text{Ti}(n,p)$ reaction and yielded a maximum 4.59×10^{-5} MBq/g/ μC for neutron yields of 30 MeV deuterons. Based on the results from this proof-of-concept study, ^{47}Sc has the potentiality to produce in a suitable quality for theranostic clinical applications.

PHITS-based internal dosimetry for organ/tissue absorbed dose estimation is reported in Chapter 4. An improved internal dosimetric calculation with the realistic Japanese reference voxel phantoms, JM-103 and JF-103 based on CT images of the real patients, have been implemented in PHITS. The novelty of our calculation system is applicability to any administrated RIs and any RIs using or to be used in the research field (e.g. tracer). The program uses the radionuclide decay database of ICRP Publication 107 and considers the ICRP recommended 83 different source regions irradiating 47 target tissues, defining the effective dose as presented in both of the ICRP Publications 60 and 103. This

calculation system applies to all of the RIs. In this thesis, we calculated the dose for many RIs including ^{132}Cs and ^{47}Sc which is newly proposed. This is the case study of the adsorbed dose calculation with RIs having prospects. An extension of the developed dose calculation method is applied to estimate the sex-averaged effective dose based on the tissue weighting factors in ICRP 2007 recommendations; are presented for ^{47}Sc with other frequently used medical RIs e.g., ^{18}F , $^{99\text{m}}\text{Tc}$, ^{90}Y , etc. Dosimetric results were showed that our developed dosimetry calculations can be recommended for the Japanese averages and also for the Asian personal. Also, this chapter presents the dose coefficients for intravenous administration for several emergent medical RIs (e.g., $^{64,67}\text{Cu}$, $^{152,161}\text{Tb}$, ^{166}Ho , etc.), and compared with data published in the ICRP Publication 53 and 128. From these aspects, the present results can play an important role as a guideline for patient-specific dosimetry.

Chapter 5 and Chapter 6 are designated for the PHITS-based external dosimetry with our developed computational framework. In Chapter 5, an operational quantity for the area or workplace monitoring called the ambient dose equivalent, $H^*(10)$, is expressed according to the latest ICRU definition. This is done by using the universal γ -ray source calculation. This procedure successfully applied to $H^*(10)$ estimation for a post-treated patient with ^{47}Sc -, ^{64}Cu -, $^{64}\text{Cu}/^{67}\text{Cu}$ -theranostics. The calculation results showed significance to the radiation safety issues especially for the clinical staff who works in the nuclear medicine department, and as well as the person who will take care of the patient after therapeutic or theranostic applications. The universal γ -ray source is one example of applications of our developed dose calculation system. If the calculation system is updated, we can calculate the universal γ -ray source with the same method using the updated one. Next, Chapter 6 set out the estimation of the absorbed dose coefficients for organs/tissues of a researcher for the occupational exposure from an external radiation source. This is also an application of our improved PHITS-based dosimetric calculation. As of practical experience, during dealing with radioactive ^{132}Cs an occupational radiation worker may expose to external radiation emitted by Cs radionuclides. This chapter explains the absorbed dose to all individual body parts of the researcher rather than an overall dose estimation with a personal dosimeter. Therefore, an occupational radiation worker can take necessary precautions to save the critical body parts by ensuring personal safety.

Finally, Chapter 7 summarized the present thesis work and pointed out the possible prospective future outlook.

1. Introduction

1.1 Background

Radioisotopes (RIs) are currently used in many fields. They are playing an important role in the industry [1] agriculture [2,3], nuclear medicine [4], and as well as research [5]. For example, ^{147}Pm is using for nondestructive investigation of the material thickness and density [6], ^{60}Co has potential application for the prevention of germination of potatoes [7], and $^{99\text{m}}\text{Tc}$ & ^{131}I in diagnosis and therapy applications in nuclear medicine [8-10]. However, the medical RIs accounts for the majority of applications [11].

RIs have been conventionally produced via nuclear reaction by using reactor-based neutron and charged particle obtained by the accelerator. RIs produced in reactors represent a large percentage of the total use of RIs due to several factors. The reactor offers an immense volume for irradiation, simultaneous irradiation of several samples, the economy of production, and therefore the possibility to supply a large form of RIs. In reactors, neutron-rich RIs are produced via the fission reaction of ^{235}U or the thermal neutron capture reaction by a sample nucleus [12]. The ^{235}U fission reaction represents by the following formula:



where A and B indicate fission fragments. As a result of this fission, neutrons are multiplied after the reaction. The multiplied neutrons are absorbed by other ^{235}U , which causes a chain reaction of fission reactions. The neutrons generated in this ^{235}U fission reaction are fast neutrons with an average of about 2 MeV.

Moreover, the first major advance occurred in 1934 with the invention of the cyclotron by Ernest Lawrence in Berkeley, California. By directing a beam of fast-moving deuterons at a carbon target, Lawrence induced a reaction that resulted in the formation of a RI with a half-life of 10 min. Particle accelerators and, particularly, cyclotrons, were vital in the preparation of RIs during the year from 1935 to the end of World War II. After World War II, reactors were accustomed to produce radioactive elements, and also the use of accelerators for this purpose became less common. Because the techniques for using radiotracers could not completely satisfy the growing demand and, therefore, accelerators were needed to provide new RIs.

Because of the neutron-rich nuclei of produced radionuclides, they decay by emitting β -rays and/or γ -rays. Radiopharmaceuticals containing electron-emitting radionuclides are useful in radioimmunotherapy (RIT), and those containing γ -rays emitting radionuclides are used for single-photon emission computed tomography (SPECT) in nuclear medicine (NM) imaging. Noted that, reactor-based RI production amount is attractive; however, constructing a new reactor, especially

only for the production of medical RIs, would be unfeasible or extremely difficult. Even there are problems to a stable supply of RIs due to trouble of a nuclear reactor for an unexpected failure or a disaster, and the limitation of half-life in long time transportation.

To solve these problems, there is a RIs production method using an accelerator neutron source [13]. By using this method, various RIs can be produced stably on site. Also, RI that has been difficult to produce in the other reaction method can be produced, so it has attracted attention in recent years.

1.1.1 Accelerator-based neutron source

Accelerator-based neutron sources include proton-induced reactions, spallation reactions, fusion reactions, and deuteron-induced reactions. At present, the following are considered as accelerator neutron sources for RI production.

- Proton-induced ${}^7\text{Li}(p,n)$ and ${}^9\text{Be}(p,n)$ reaction [14,15]

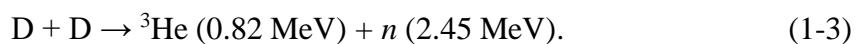
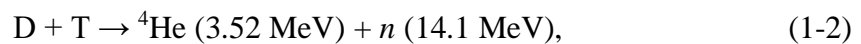
The ${}^7\text{Li}(p,n)$ and ${}^9\text{Be}(p,n)$ reaction are characterized by a low threshold value and a high cross-section for protons with low energy. This neutron source is used in boron neutron capture therapy (BNCT). BNCT utilizes the ${}^{10}\text{B}(n,\alpha)$ reaction, which requires low energy neutrons to occur efficiently. Therefore, the neutrons generated using the ${}^7\text{Li}(p,n)$ reaction and ${}^9\text{Be}(p,n)$ reaction are used as thermal and epithermal neutrons by the moderator.

- Nuclear fragmentation reaction with intense proton and deuteron beams [16]

When a few GeV protons or deuterons are incident on a heavy target such as lead or mercury, a spallation reaction occurs. In this reaction, a plurality of protons and neutrons, or deuteron and helium which are composite particles are emitted from the target nucleus. As a result, this reaction is characterized by high neutron intensity. As an example, the neutrons obtained by this reaction are expected to be applied to an accelerator-driven subcritical reactor, which can apply to use for transmutation. However, high-energy neutrons produce many byproducts in RI production.

- D-D and D-T fusion reactions [17]

A nuclear fusion reactor is a type of nuclear reactor that uses to generate electricity. When deuteron interacts with deuterium or tritium, the following nuclear fusion reaction occurs



The neutrons emitted in these reactions have strong monochromaticity because they are emitted with energy according to the Q value of the nuclear reaction. In RI production, it can be used to investigate the characteristics of nuclide production for each neutron energy. Besides, since it is an exothermic reaction, it shows a high reaction cross-section at incident energy as low as several hundred keV and has the feature that it is easy to obtain high-energy neutrons. Therefore, even a very small accelerator can generate neutrons.

- Deuteron-induced $^{\text{nat}}\text{C}(d,n)$, $^9\text{Be}(d,n)$, etc. reaction [13]

Deuterons are nuclei in which one proton and one neutron are weakly coupled. Irradiation of $^{\text{nat}}\text{C}$ or ^9Be with accelerated deuterons causes deuteron elastic breakup reactions, inelastic breakup reaction, and stripping reactions to obtain high-intensity neutrons. The neutron converter is set thicker than the range of deuterons. The neutron yield distribution emitted from the thick neutron converter is called thick target neutron yield (TTNY). This reaction can adjust TTNY by changing incident deuteron energy, and the production of by-products can be suppressed. In RI production, research is being conducted to utilize this feature to efficiently produce RI [18-26]. Figure 1.1 shows a conceptual diagram of neutron production by the deuteron-induced reaction.

Therefore, among these accelerator-based neutron sources, deuteron-induced reactions on $^{\text{nat}}\text{C}$ and ^9Be is promising. The amount of generated neutrons in the deuteron-induced reaction is larger than that in the proton-induced reaction to the light nuclei (e.g. $^{\text{nat}}\text{C}$ or ^9Be) used in the quasi-monochromatic neutron source, and the energy of the produced neutrons can be adjusted by changing the energy of the incident deuteron [27,28].

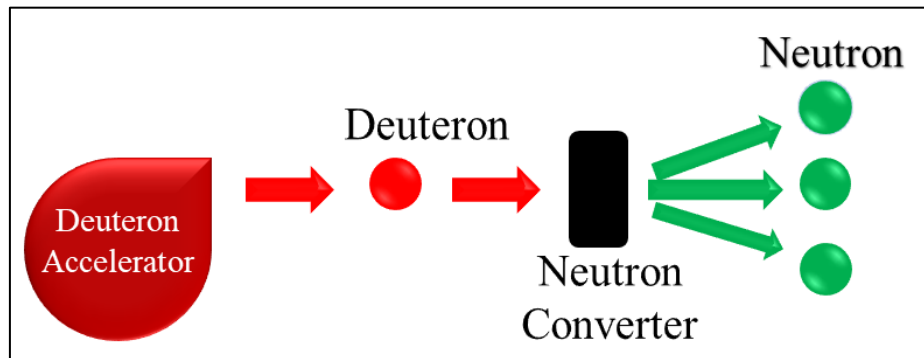


Fig. 1.1: Schematic diagram of neutron production by deuteron-induced reaction.

1.1.2 Experimental data availability of deuteron-induced nuclear reactions

Currently, many experimental data are maintained in the Experimental Nuclear Reaction Database (EXFOR) [29] by the Nuclear Data Department of the International Atomic Energy Agency (IAEA). Figure 1.2 shows the number of experimental data on the deuteron incident neutron production reaction as a function of incident deuteron energy, which is published in EXFOR. It can be seen that the experimental data of deuteron induced reaction on C is scarce in TTNY. Also, experimental data are measured concentrating on neutron converter (Li, Be, C) which are important for the evaluation of neutron source performance, and the measured incident energy range is also limited.

Figure 1.2 shows that the incident energy range is limited for neutron converters such as Be and C. Since there is little data on the neutron spectrum, which is the differential quantity, it is difficult to evaluate the integrated amount such as the activation quantity with high accuracy. Also, for the design of the irradiation system and estimation of the production yield of RI and its purity, accurate double-differential thick target neutron yields (DDTTNYs) are required [31]. There are, but, data for thick target especially C is not enough available within the energy region.

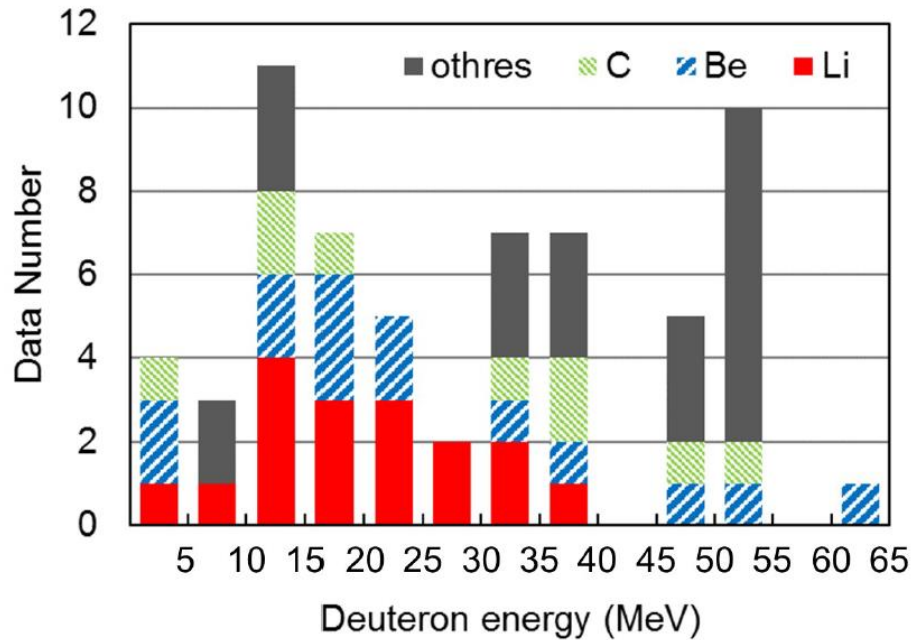


Fig. 1.2: Number of experimental data of deuteron incident TTNY published in EXFOR. (Figure is cited from ref. [30].)

1.1.3 Theoretical approach to deuteron-induced nuclear reactions

In recent years, it has become popular to use of Monte Carlo transport calculation codes such as Particle and Heavy Ion Transport code System (PHITS) [32], Monte Carlo N-Particle code (MCNP) [33], and Geant [34] for DDTTNY estimations. In these calculation codes, nuclear reactions are described using a file that contains nuclear reaction information. The accuracy of transport calculations greatly depends on the nuclear data. However, the nuclear data of the deuteron-induced reaction has not been sufficiently prepared and expanded, which is a major issue in the design and development of the deuteron accelerator neutron source.

Moreover, several theoretical model codes correspond to the deuteron reaction have been proposed so far. An example of a code system dedicated to the deuteron-induced reactions, deuteron-induced reaction analysis code system (DEURACS) [35]. In particular, DEURACS can analyze (d, xn) reactions using the experimental data of DDTTNY and showed that the experimental data can be well reproduced [35]. However, as mentioned earlier, the experimental data on the neutron production reaction is scarce, so the verification is not sufficient, which is a major obstacle to the improvement of the model. Therefore, systematic measurements of the DDTTNY by ourselves are necessary especially for the RI production study.

1.1.4 DDTTNY measurement method

There are a few traditional DDTTNY measurement methods, e.g. the multiple-foil activation method, the time-of-flight (TOF) method, an organic liquid scintillator detector method, and the method with Bonner sphere detector. With the TOF and liquid scintillator unfolding methods, DDTTNYs of each neutron emission angle should be measured one by one. We can increase the number of detectors and put them at multi-angles to shorten experiment time. However, even for that case, we cannot measure all angles at once, because neutron intensity is drastically changed with emission angle. In contrast, we can obtain DDTTNYs at all neutron emission angles at once by using the multiple-foil activation method. Therefore, it is ideal for the systematic measurements.

In the multiple-foil activation method, the number of produced atoms is measured by γ -ray detection using high purity germanium (HPGe) detector after the irradiation experiment. The relation between the number of atoms produced, N_i , of a certain nuclide i , and the DDTTNY, $\phi(E)$, of the neutron energy E can be expressed by the following equation [36].

$$N_i = \int R_i(E)\phi(E)dE, \quad (1-4)$$

where $R_i(E)$ is a production rate function, which can be uniquely obtained from the reaction cross-section and irradiation conditions, and is a function of neutron energy E . It is impossible to derive the neutron spectrum from the integral equation of Eq. (1-4). In the actual analysis, this integral equation should be treated in the discrete form as follows:

$$\begin{pmatrix} N_x \\ N_y \\ \vdots \\ N_i \\ \vdots \\ N_n \end{pmatrix} = \begin{pmatrix} R_{x,E_1} & R_{x,E_2} & \cdots & R_{x,E_j} & \cdots & R_{x,E_m} \\ R_{y,E_1} & R_{y,E_2} & \cdots & R_{y,E_j} & \cdots & R_{y,E_m} \\ \vdots & \vdots & \ddots & \vdots & & \vdots \\ R_{i,E_1} & R_{i,E_2} & \cdots & R_{i,E_j} & \cdots & R_{i,E_m} \\ \vdots & \vdots & & \vdots & \ddots & \vdots \\ R_{n,E_1} & R_{n,E_2} & \cdots & R_{n,E_j} & \cdots & R_{n,E_m} \end{pmatrix} \begin{pmatrix} \phi_{E_1} \\ \phi_{E_2} \\ \vdots \\ \phi_{E_j} \\ \vdots \\ \phi_{E_m} \end{pmatrix}, \quad (1-5)$$

here, N_k represents the amount of produced nuclide k , $R(k,E_i)$ represents the production rate of nuclide k concerning the neutron energy group E_i , and $\phi(E_i)$ represents the neutron yield of E_i . In general, the number of activation reactions of interest (n) is less than the number of neutron energy groups (m). So that $\phi(E_i)$ cannot be directly determined. Therefore, a computational technique is required to unfold the neutron spectrum and can be acquired by solving the inverse problem. In the field of neutron measurement, the process of solving the inverse problem is called unfolding.

To date, many unfolding codes have been developed. For example, GRAVEL [37], MAXED [38], MIEKE [37], RooUnfold-Bayes [39], and ANN [40] are using depends on their initial input conditions. However, there is no standard method for selecting these codes or deriving conditions for inverse problem solutions, and it depends on the trial and error and experience of each researcher. GRAVEL is a conventional unfolding code for neutron spectrum measurement by the multiple-foil activation method. This is a spectrum adjustment code, and an initial guess spectrum is required which can calculate by using DEURACS [35]. An unfolded neutron data can apply to the study of RI production respective of the field of application.

1.1.5 Dose calculation

RIs are promising due to its growing demand in our life. Due to the radioactive characteristics of RIs, they emit radiation. The medical use of radiation is now pervasive and routine. Diagnostic radiology, nuclear medicine, and RIT have all evolved into advanced techniques and are thought to be essential tools across all branches and specialties of medicine for the advanced use of RIs. To protect a human body from excessive radiation dose, the measurement of radiation dose *i.e.* radiation dosimetry is essential. The International Commission on Radiological Protection (ICRP) jointly with the International Commission on Radiation Units and Measurements (ICRU) have set necessary recommendations for radiation

dosimetry. Estimation of the radiation dose quantities (physical, protection, and operational quantities) is suggested for the internal and the external dosimetry. To control radiation effects on the human body, it is necessary to take into account the consequences of exposure on multiple parts of the body. Thus, protection quantities are calculated based on absorbed doses for organs/tissues in the human body. They cannot be measured directly with instruments. Moreover, to indicate effects on the human body, operational quantities are defined. Operational quantities include the ambient dose equivalent used in the area or workplace monitoring. It can provide a conservative estimation of protection quantity, the effective dose, when applying appropriate conversion coefficients given in the ICRP publication [41]. These conversion coefficients were derived in different body geometry of the human body models and for various charged or neutral particle irradiation. Ultimately, a human body model is required for both internal and external radiation dosimetry.

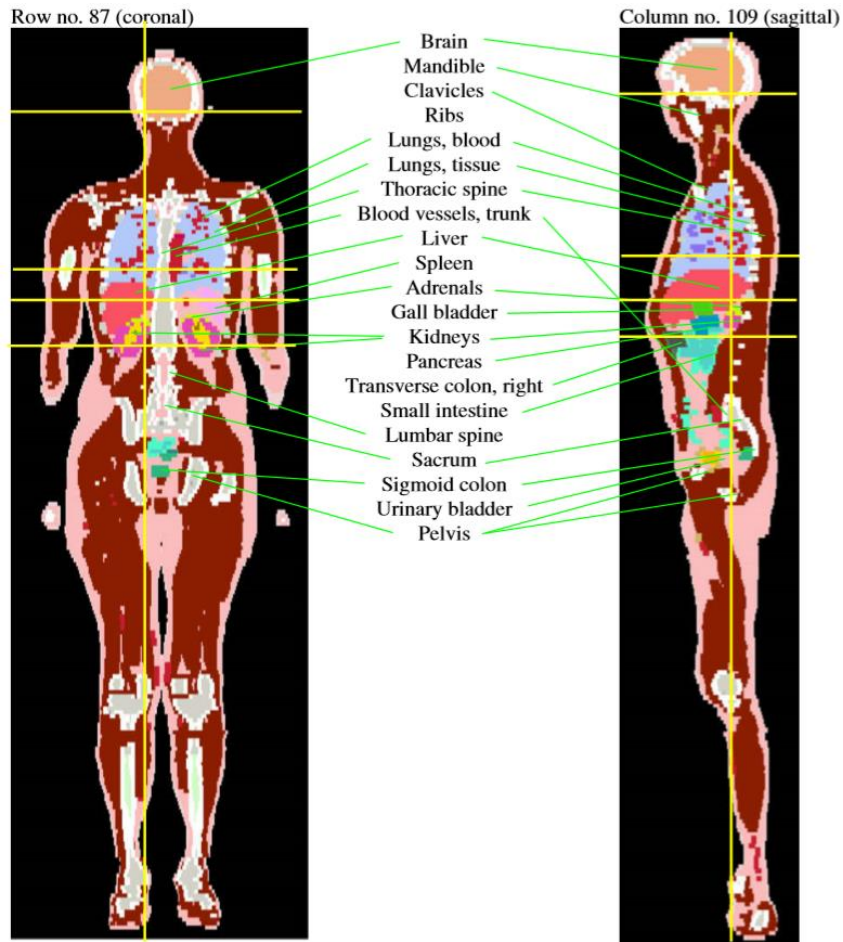
1.1.6 General features of the ICRP/ICRU adult reference computational voxel phantoms

The ICRP jointly with the ICRU has developed the human body models from reference persons resembling an adult male of 73 kg and a female of 60 kg. These mathematical models are referred to as phantoms in this thesis. Later, ICRP updated the basic anatomical and physiological data for the reference person in 2002 [42,43], and therefore new mathematical models had been created. Phantoms for adults based on tomographic images from a real adult male (AM) and adult female (AF), rather than mathematical models, were published in 2009 [44]. These phantoms resembled the predefined anatomical values regarding height and weight and the organs and tissues were adjusted according to the specifications given in the publication of anatomical reference values [43]. The main characteristics of both AM and AF are summarized in Table 1.1, and graphical representations are shown in Fig. 1.3.

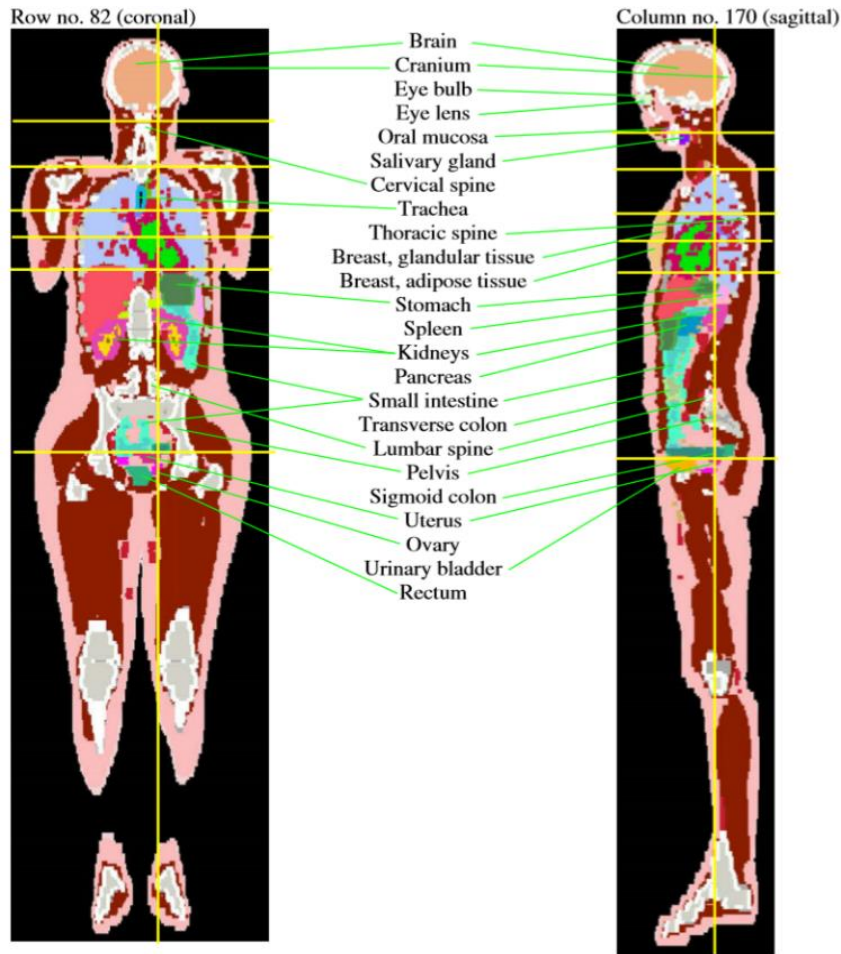
Calculations of the radiation dosimetry are based on biokinetic models of the body and its various organs/tissues. In the case of person-specific dosimetry for a patient, these models must be similar as possible to the patient anatomy. Also, the accuracy is improved if the model reflects the structure of the organs/tissues and can consider the location of, particularly sensitive cells. Since an updated set of reference values for basic anatomical and physiological data was given in ICRP Publication 89 for both male and female subjects of six different ages (newborn, 1, 5, 10, and 15 years, and adult) based on statistics for Western Europeans and North Americans [44] and are different from Asian reference personals. So that, dose estimations with the ICRP reference phantoms may not reflect the proper investigation for the Asian peoples.

Table 1.1: Main characteristics of the AM and AF computational phantoms. [44]

Property	AM	AF
Height (cm)	176	163
Weight (kg)	73	60
Number of (non-zero) voxels (millions)	1.95	3.89
Slice thickness (voxel height, mm)	8	4.84
Voxel in-plane resolution (mm)	2.13714	1.775
Voxel volume (mm ³)	36.54	15.25
Number of columns	254	299
Number of rows	127	137
Number of slices	220	346



(a)



(b)

Fig. 1.3: Coronal and sagittal images of (a) the male (b) the female reference computational phantom published in the ICRP Publication 110. [44]

1.1.7 PHITS-based Japanese voxel phantoms

In recent years, the Japan Atomic Energy Agency (JAEA) developed Monte Carlo particle transport simulation code PHITS executable the Japanese voxel phantoms to clarify the effects of anatomical characteristics of Japanese on dose assessments. These realistic human phantoms have been developed based on medical images such as CT imaging of actual persons [45]. The voxel size of these phantoms is $0.98 \times 0.98 \times 1.0 \text{ mm}^3$. Also, the tissue segmentations of the new Japanese adult male and female phantoms were based on ICRP Publication 103 [46]. Then, these phantoms are called as JM-103 and JF-103 phantoms, respectively;

which has body sizes and organ masses that are near the Japanese averages and would give more precise dosimetric results.

Table 1.2: Masses of selected organs and tissues of the JM-103, JF-103 [47], AM and AF phantoms [44], and the averages of adult Japanese [48]. Values in parentheses are the ratios of masses of JM-103, JF-103, AM, and AF to averages of adult Japanese.

Organ and tissue	Mass (kg)				Japanese averages	
	JM-103	JF-103	AM	AF		
					Male	Female
Adipose	14.192(1.02)	13.815(1.06)	20.458(1.47)	23.596(1.82)	13.900	13.000
Adrenal	0.015(1.04)	0.012(0.92)	0.014(1.00)	0.013(1.00)	0.014	0.013
Gall bladder	0.008(1.02)	0.006(1.03)	0.014(1.74)	0.010(1.71)	0.008	0.006
Hard bone	7.304(1.62)	4.866(1.43)	5.500(1.22)	4.000(1.18)	4.500	3.400
Kidney	0.333(1.04)	0.271(0.97)	0.310(0.97)	0.275(0.98)	0.320	0.280
Liver	1.462(0.91)	1.311(0.94)	1.800(1.13)	1.400(1.00)	1.600	1.400
Lung	1.215(1.01)	0.978(1.07)	1.208(1.01)	0.950(1.04)	1.200	0.910
Marrow (active)	1.192(1.19)	0.956(1.23)	1.170(1.17)	0.899(1.15)	1.000	0.780
Marrow (inactive)	2.526(1.94)	1.911(1.93)	2.480(1.91)	1.800(1.82)	1.300	0.990
Muscle	28.198(1.03)	20.212(1.01)	29.000(1.05)	17.500(0.88)	27.500	20.000
Skin	2.189(0.91)	1.898(1.05)	3.728(1.55)	2.721(1.51)	2.400	1.800
Spleen	0.139(1.00)	0.110(0.92)	0.150(1.07)	0.130(1.08)	0.140	0.120
Stomach	0.141(1.01)	0.106(0.97)	0.150(1.07)	0.140(1.27)	0.140	0.110

Table 1.2 shows the masses of selected organs and tissues of the JM-103, JF-103 [47], AM and AF [44], along with adult Japanese averages [48]. The masses of most organs and tissues of JM-103 and JF-103 agree with Japanese averages within 10%. Therefore, dose estimations with these reference voxel phantoms may give the proper investigation for the Japanese and as well as the Asian.

1.2 Motivations and Objectives

Taking into consideration mentioned in the above circumstances, it is necessary to calculate the systematic measurement of unfolding DDTTNY at various incident deuteron energy. By using the obtained unfolding DDTTNYs, RIs can produce to aim a variety of applications. RI promising for environmental radioactivity monitor and suitable to use as an alternative environmental tracer or becoming prominent to nuclear medicine applications can produce with optimum production yield. However, the production method is the direct incident of the raw material or any theoretical simulation process. According to the field of application, RIs are made concern due to their radioactive characteristics of radiation emission. So that, the measurement of radiation dose to the human body is mandatorily important. It can be done according to the international guideline of radiation dosimetry provided by the ICRP, ICRU, or national requirements. Since in the dosimetry calculation (for both internal and external dosimetry) an appropriate human body model is required. For this purpose, the ICRP reference adult phantoms, AM and AF, are commended by the ICRP and ICRU. In contrast, these phantoms having different anatomical and physiological properties that may not reply an exact dosimetric results for the Asian. Therefore, this research motivated to investigate the internal and the external radiation doses i.e. radiation quantities (protection and operational) with more realistic phantoms which can estimate dosimetric investigations for the Japanese and as well as the Asiatic references. This research mainly aimed to calculate the radiation doses for the Japanese voxel reference phantoms, JM-103 and JF-103, in accordance with the latest ICRP recommendations published in the ICRP Publication 103, and with the ICRU definitions. To obtain more accurate dosimetry results, the approach was to use a combination of detailed biokinetic data of RIs from ICRP Publication 107 to be used in voxel phantoms, JM-103 and JF-103, for implementing with Monte Carlo particle transport simulation, named, PHITS. Beside of these investigations with newly implemented PHITS-based dosimetric methods, especially, it can also calculate the quantity called the ambient dose equivalent (i.e. $H^*(10)$) for area or workplace monitoring to keep secure the hospital staffs and the associated carers from excessive external radiation dose. The special feature of this calculation is the use of dumped information of particle transport from the body surface of a patient after the clinical trials of nuclear medicine administration. To do the tasks mentioned above, the specific purposes of this research are therefore as follows:

- To measure the DDTTNY of accelerator-based neutron by 12, 20, and 30 MeV of incident deuteron energy and to optimize the trend of neutron yields with the incident deuteron energy and the neutron emission angle.
- To produce RIs using the measured thick target neutron yields, having promising applications as an environmental tracer and as theranostic radiopharmaceuticals in nuclear medicine.

- To develop an improved method of internal dosimetry by using a Monte Carlo based code PHITS simulation, which could perform absorbed dose calculations on the new Japanese voxel phantoms and to estimate the effective dose based on the tissue weighting factors in ICRP Publication 103.
- To create a PHITS-based dosimetric method for safety issues for the hospital staff and associated carers, which could perform by using the information on particles recorded in a file named, 'dump' file.
- To estimate the absorbed dose to the organs/tissues of a researcher due to the occupational exposure of external radiation source.
- To enable a radiation dosimetry method to make PHITS simulations with voxel phantoms, JM-103 and JF-103, more user friendly.

1.3 Thesis Structure

This thesis is composed of seven chapters including this introduction. Chapter 2 to Chapter 6 precisely explains all the objectives of the thesis. At a glance, this thesis is based on the research results of (a) the accelerator-based neutron source and its application to RIs production, and (b) PHITS-based internal and external radiation dosimetry. In particular:

Chapter 2 is devoted to the measurement of the thick-target neutron yield by using deuteron induced accelerator-based neutron source and the multiple-foil activation method. 12, 20, and 30 MeV deuterons were separately incident on a thick target made of ^{nat}C and the emitted neutrons irradiated ^{nat}Ni , ^{nat}In , ^{27}Al , ^{59}Co , and ^{93}Nb foil those were placed at 0° , 10° , 20° , 30° , and 45° from the deuteron beam direction. Neutron spectra were unfolded for each incident deuteron energy and each neutron emission angle by using an iterative, initial guess depended GRAVEL code. A detailed comparison of yields to other available published data are also explained in this chapter.

In Chapter 3, the application of accelerator-based neutron for RIs production is discussed. This chapter is categorized into two parts. At first, a tracer ^{132}Cs production experiment is described; which is produced by irradiating a 12-g of Cs_2CO_3 sample using accelerator-based neutrons by 30 MeV deuterons. Also, a feasibility study on andosol, haplic fluvisol, and gleyic fluvisol soil is explaining that ^{132}Cs can be used as an alternative tracer of ^{137}Cs for environmental radioactive monitoring. Later, the production yields and purities of an emergent theranostic medical RI, ^{47}Sc is estimated by PHITS simulation. Unfolding results of neutron yields for each of 12, 20, and 30 MeV incident deuteron energy have been used for PHITS simulation to produce ^{47}Sc .

A PHITS-based internal dosimetric computational framework for organ/tissue absorbed dose estimation is reported in Chapter 4. An improved internal dosimetric calculation with the Japanese reference voxel phantoms, JM-103 and JF-103, has been implemented in PHITS simulation. An extension of the developed dose calculation method is applied to estimate the effective dose based on the tissue weighting factors in ICRP Publication 103; they are presented for ^{47}Sc together with other prominent medical RIs. It is noted that, this chapter also presents dose coefficients for intravenous administration for several RIs used in nuclear medicine. Moreover, a comparative scenario between the present calculation results and the internal dosimetric results with ICRP/ICRU reference phantoms, AM and AF, are given in the chapter too.

Chapter 5 and Chapter 6 are designated for the PHITS-based external dosimetry. In Chapter 5, an operational quantity for area or workplace monitoring called the ambient dose equivalent, $H^*(10)$, is expressed according to the ICRU definition. The calculation is newly done by using the PHITS ‘dump’ file option. So that the calculation results are useful to the radiation safety issues especially for the hospital staff who works in the nuclear medicine department, and as well as the person who will take care of the patient after therapeutic or theranostic application. This chapter successfully validated $H^*(10)$ estimation by reading the created ‘dump’ files when a patient treated by ^{47}Sc -theranostic. On the other hand, Chapter 6 set out the estimation of the absorbed dose coefficients for organs/tissues of a researcher for the occupational exposure from an external radiation source. From practical experience, during dealing with radioactive ^{132}Cs a researcher may expose to external radiation emitted by ^{132}Cs . This chapter explains the dose to all individual body parts of the researcher rather than an overall dose estimation with a personal dosimeter.

Finally, Chapter 7 gives a summary and conclusions, and the perspective of the future work are also described.

2. Thick Target Neutron Yields of Accelerator-Based Neutron Source

Now a day, demand for high-intensity neutron sources in various neutron application fields are increasing. Special attention has been focused on deuteron accelerator-based neutron source in the International Fusion Materials Irradiation Facility (IFMIF) [49], Neutron for Science (NFS) at the Système de Production d'Ions Radioactifs en Ligne de 2e génération (SPIRAL2) [50], and in radiotherapy [51,52]. Moreover, neutron sources have been proposed for the medical radioisotopes (RIs) production. For example, Nagai *et al.* proposed a production method of ^{99}Mo , which is the mother nuclide of the most used medical RI, $^{99\text{m}}\text{Tc}$ [13,24]. In some other applications, the production method and estimation of the production yield of RIs used for diagnosis and therapy in nuclear medicine have been also proposed by using the accelerator-based neutron source [18,19,23].

It is also noted that, in the design of deuteron accelerator facilities, it is important to estimate neutron yields and induced radioactivity based on reliable experimental data. So that information of the DDTNYS for deuteron incidence as the neutron source term is important for the accurate neutron yield estimation. However, data availability of deuteron-induced reactions is not enough to fulfill the requirements. Also, theoretical models of deuteron induced reaction cannot be verified systematically in deuteron energy and neutron emission angles. In such a case, more experiments should be carried out with higher-energy incident deuterons at least from a few MeV to around 50 MeV.

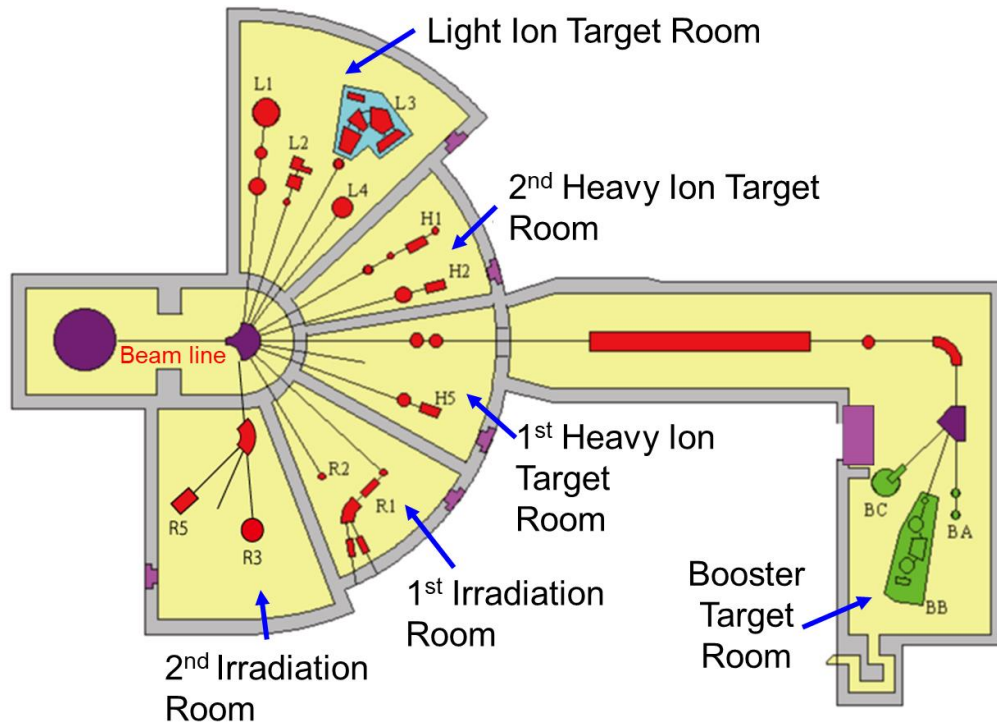


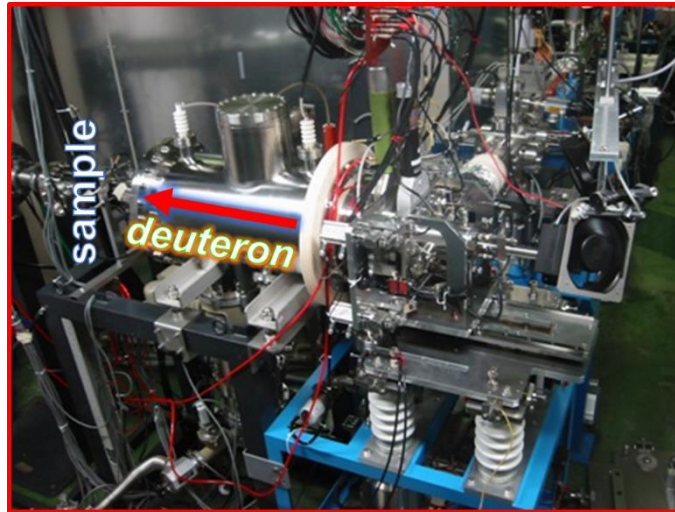
Fig. 2.1: An outline of the JAEA tandem accelerator system and beamline facility, excerpted from ref. [53].

2.1 Experiment

The purpose of the experiments was a systematic measurement of the neutron spectra, called DDTNYS for 12, 20, and 30 MeV deuterons on ^{nat}C by means of the multiple-foils activation method. The experiments were conducted at the tandem accelerator facility at JAEA. The JAEA-Tokai tandem accelerator can generate the highest acceleration voltage (18 MV) of an electrostatic accelerator in Japan and is one of the highest in the world. It was established to provide multi-purpose use of accelerators, use of difficult-to-handle high-level RIs, and RI study for general education and training. This accelerator is capable of accelerating deuterons to the maximum beam current 3 μA with the small beam size (1 mm \varnothing). Figure 2.1 shows a schematic diagram of an overview of the JAEA tandem accelerator facility. Moreover, detail of the experimental steps is given in the following sub-sections.

2.1.1 Irradiation conditions

Deuterons were accelerated to the incident energy of 12, 20, and 30 MeV by the accelerator and bombarded on a carbon target of 4-mm thick and 20 mm in diameter. This carbon target has a purity of 99.99% (supplier: The Nilaco Corporation, Tokyo, Japan [54]). The target thickness was sufficient to stop completely the incident deuteron ions and it was confirmed by following SRIM-2013.00 calculations [55] (*e.g.* deuteron range in ^{nat}C is about (2.51 ± 0.10) mm for maximum deuteron energy, 30 MeV). Following that, accelerator-based neutrons were generated via the $^{nat}\text{C}(d,n)$ reactions. Generated neutrons passed through a vacuum collimator, and they irradiated multiple foils placed on the stage 10 cm downstream from the neutron source. Irradiated multiple foils made of ^{nat}Ni , ^{nat}In , ^{27}Al , ^{59}Co , and ^{93}Nb . Irradiation was performed on a multi-layered foil composed of the above-mentioned metal foils. The experimental setup is illustrated in Fig. 2.2.



(a)

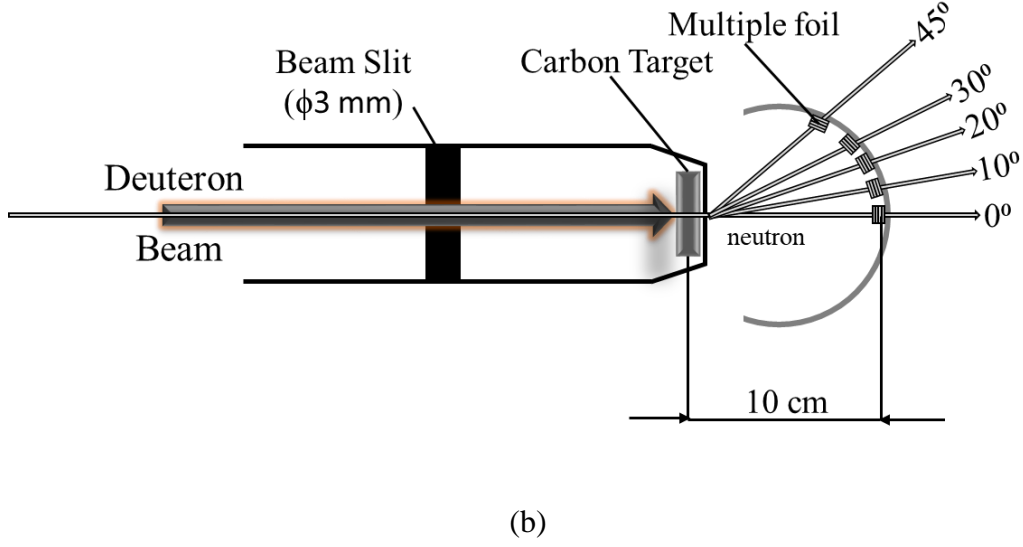


Fig. 2.2: (a) Photograph and (b) schematic view of the experimental setup.

The foils were placed at 0°, 10°, 20°, 30°, and 45° from the deuteron beam direction. Their dimensions, the amount used in the experiment, and isotopic natural abundances are listed in Table 2.1. The beam current was recorded every 10 seconds using MCS (Multi-Channel Scalar). The current was measured using the carbon target as a Faraday cup. The foils were irradiated for different time with different beam current for each incident deuteron energy. By which means, during 300 min with an average beam of 250 nA, 300 min with an average beam of 210 nA, and 250 min with an average beam of 150 nA for 12, 20, and 30 MeV of deuteron energy, respectively. The beam intensities were determined to achieve a small focal size of 3 mm for each deuteron energy.

Table 2.1: Properties of the activation foils used in the experiment. These samples are available commercially and collected from the Nilako corporation [54].

Sample	Isotope & Natural Abundance* (%)	Sample size	Sample weight (mg)		
			$E_d =$ 12MeV	$E_d =$ 20MeV	$E_d =$ 30MeV
^{nat}Ni	^{58}Ni (68.08)	$\phi 10 \text{ mm}$ $\times 1 \text{ mm}^t$	679	691	700
	^{60}Ni (26.22)				
	^{61}Ni (1.14)				
	^{62}Ni (3.63)				
	^{64}Ni (0.93)				
^{27}Al	100	$\phi 10 \text{ mm}$ $\times 1 \text{ mm}^t$	105	105	104
^{59}Co	100	$8 \text{ mm} \times 8 \text{ mm}$ $\times 0.25 \text{ mm}^t$	159	154	155
^{93}Nb	100	$\phi 10 \text{ mm}$ $\times 0.25 \text{ mm}^t$	172	173	171
^{nat}In	^{113}In (4.29)	$8 \text{ mm} \times 8 \text{ mm}$ $\times 0.5 \text{ mm}^t$	244	249	250
	^{115}In (95.71)				

*Isotope natural abundance were taken from ref. [56].

2.1.2 γ -ray measurement of irradiated sample

A coaxial High Purity Germanium (HPGe) detector was used to detect γ -rays from the activated foils. Raw signals from the HPGe detector were processed using standard NIM electronic modules; spectroscopy amplifier (ORTEC 672) and a multichannel analyzer (ORTEC Easy-MCA-8k). The γ -rays were measured at a distance 50 mm from the HPGe detector head. The HPGe detector head was surrounded by lead blocks to suppress natural γ -rays. Besides, the environmental background γ -ray spectrum was also considered. The background spectrum was subtracted from the γ -ray spectra for activated foils, and then the γ -ray photo peaks were fitted using a Gaussian function to derive their count.

2.2 Data Analysis

2.2.1 Activity determination at the end of irradiation

After the foils were irradiated, γ -rays from the induced activities were measured with a HPGe-detector, whose detection efficiency had been calibrated with standard γ -ray sources. This is already described in section 2.1.2. Then, the activity of a nuclide at the end of irradiation (EOI) is calculated by the following relation:

$$A = \frac{Y \cdot \lambda}{I_{\gamma} \varepsilon_{\gamma} (e^{-\lambda t_c} - e^{-\lambda(t_c + t_m)})} \quad (2-1)$$

where Y , λ , I_{γ} , ε_{γ} , t_c , and t_m represent the peak area of a γ -ray photopeak, the decay constant of the isotope of interest (/sec) [56], the γ -ray emission probability [56], the detection efficiency of gamma-ray, the cooling time before measurement (sec), and the measurement time (sec), respectively. It is needed to mention that the uncertainty of the peak areas is determined by their statistics and standard deviation of fitting parameters. The uncertainties in the peak areas range from about 1% up to around 10% depending on the number of counts and the shape of the peak.

Table 2.2: A detailed list of the number of atoms produced at the EOI.

Reaction	Half-life of the produced nuclide [56]	γ -ray energy, E_γ (MeV) and intensity (%) [56]	Deuteron Energy, E_d (MeV)	No. of atoms produced in the product nuclide (-)				
				0°	10°	20°	30°	45°
$^{58}\text{Ni} (n,p)^{58}\text{Co}$ $^{27}\text{Al} (n,\alpha)^{24}\text{Na}$ $^{59}\text{Co} (n,\alpha)^{56}\text{Mn}$ $^{93}\text{Nb}(n,\alpha)^{90\text{m}}\text{Y}$	70.86 d 14.10 h 2.58 h 2.67 d	0.811 (99.45) 1.369 (99.99) 0.847 (98.85) 0.203 (97.3)	12	5.38×10^8	4.73×10^8	2.70×10^8	1.85×10^8	7.22×10^7
				9.08×10^6	6.14×10^6	4.56×10^6	2.36×10^6	6.06×10^5
				6.59×10^5	6.21×10^5	3.79×10^5	1.92×10^5	5.20×10^4
				5.82×10^4	5.58×10^4	4.94×10^4	2.18×10^4	-
			20	2.22×10^9	1.66×10^9	9.96×10^8	5.60×10^8	2.56×10^8
				1.14×10^8	8.47×10^7	4.74×10^7	2.16×10^7	7.32×10^6
				9.36×10^6	7.80×10^6	4.40×10^6	2.11×10^6	6.19×10^5
				8.61×10^6	7.93×10^5	4.54×10^5	2.51×10^5	7.22×10^4
			30	2.26×10^9	2.35×10^9	8.90×10^8	4.29×10^8	2.66×10^8
				2.11×10^8	1.58×10^8	6.65×10^7	2.62×10^7	1.38×10^7
				1.70×10^7	1.68×10^7	6.54×10^6	3.20×10^6	1.18×10^6
				2.21×10^6	2.19×10^6	9.41×10^5	4.12×10^5	1.72×10^5

2.2.2 Derivation of nuclide production

The radioactivity of the product nuclides of the reaction at the EOI can be calculated by using Eq. (2-1). Therefore, the number of nuclides produced, N_k can be derived by dividing Eq. (2-1) by decay constant of the respective nuclide, λ . Table 2.2 shows the list of the number of nuclides produced at the EOI of the multiple foils.

2.2.3 Production rate

Equation (1-5) in section 1.1.4 describes the relationship of the number of nuclides produced at the EOI when foils irradiation is treating by multiple-foil activation method. It was mentioned that the production rate function is required to unfold the neutron spectrum. For the discrete distribution, the production rate function, $R_i(E)$ can be written as shown in Eq. (2-2). [57]

$$R_{ij} = \sigma_{ij} \frac{N_T Q}{\lambda_i t} \Omega_T (1 - e^{-\lambda_i t}) \quad (2-2)$$

where R_{ij} represent a production rate corresponding to the neutron energy group j of i^{th} reaction. On the right side of the equation, σ_{ij} , N_T , λ_i , Q , t , Ω_T represent reaction the cross-section (barn), the surface density of a sample (/cm²), the decay constant of a product nuclide (/sec), the total charge of deuterons (μC), the irradiation time (sec), and the solid angle of a foil from neutron source (sr), respectively. The cross-section used in the calculation was obtained from the evaluated nuclear data library EAF-2010 [58]. Figure 2.3 shows the production rate obtained by setting the neutron energy groups to 150. In this function, the threshold energy of each reaction and the energy E_{th} exceeding 1/150 of the highest value in the range of 0 to 30 MeV maximum are shown in Table 2.3.

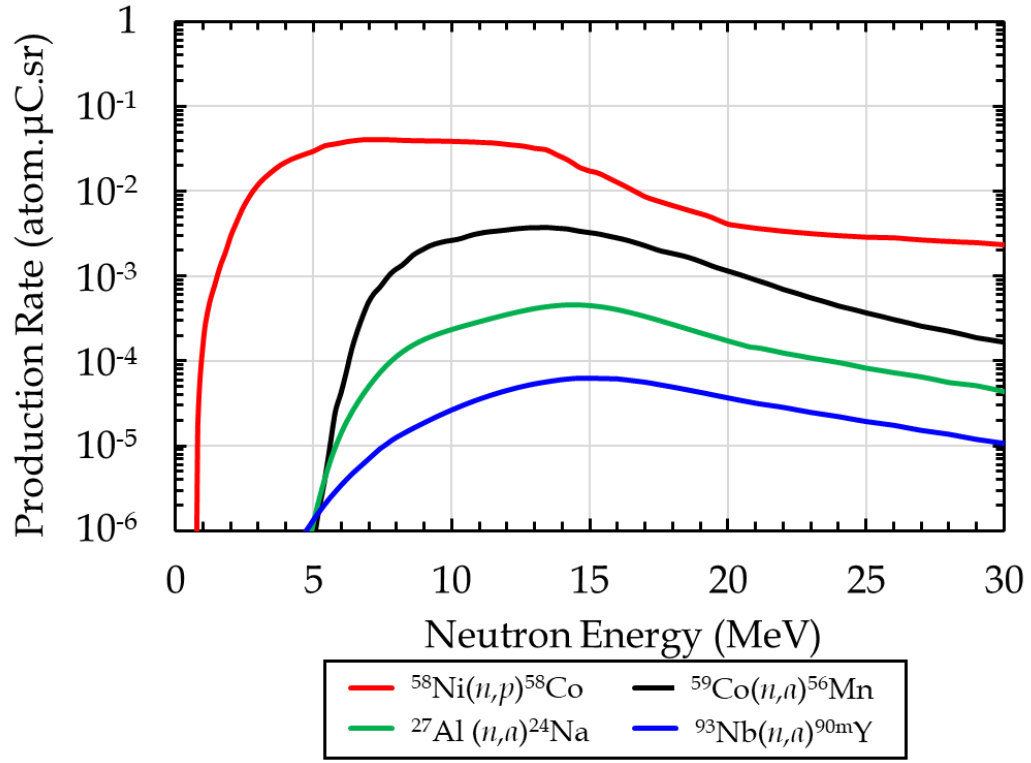


Fig. 2.3: Production rate for the interested reactions (Figure shows the production rate for the reactions produced by 30 MeV incident deuteron energy and for multiple-foils position at 0°).

Table 2.3: Reaction and energy threshold of the reaction.

Reaction	Reaction threshold energy (MeV) [59]	E_{th} (MeV)
⁵⁸ Ni(n,p) ⁵⁸ Co	0.0	0.6
²⁷ Al(n,α) ²⁴ Na	3.25	5.2
⁵⁹ Co(n,α) ⁵⁶ Mn	0.0	5.0
⁹³ Nb(n,α) ^{90m} Y	0.0	4.8

2.2.4 Unfolding process

The unfolding of neutron energy spectra is of importance in various problems of radiation protection or health physics [60]. The unfolding process is performed using the derived nuclide production amount and the production rate. The results from Eq. (2-2) can be a substitute to Eq. (1-5) for $\phi(E_i)$ calculation. Since it is already known that $\phi(E_i)$ cannot be directly determined and an unfolding method is necessary to derive it. So that, this research used a conventional unfolding code, GRAVEL [37] which is based on iterative approximation algorithm for neutron spectrum measurement by the multiple-foil activation method. Since this is spectrum adjustment code, an initial guess spectrum, which is theoretically or empirically calculated, is required. An unfolded neutron spectrum is strongly dependent on the initial guess spectrum.

2.2.4.1 Initial Guess Neutron Spectrum

The initial guess spectrum is used as a priori information for deriving resultant spectrum. In this research, theoretical calculation results calculated by DEURACS [35] were used as the initial guess spectrum. DEURACS can accurately reproduce the DDTNY in the present experiment condition. For the initial guess spectrum, TTNy derived from $^{nat}\text{C}(d,n)$ reaction where the thickness of the thick target was determined according to the experimental conditions. For deuteron energy 12, 20, and 30 MeV, DEURACS calculation of initial guess spectrum is shown in Fig. 2.4.

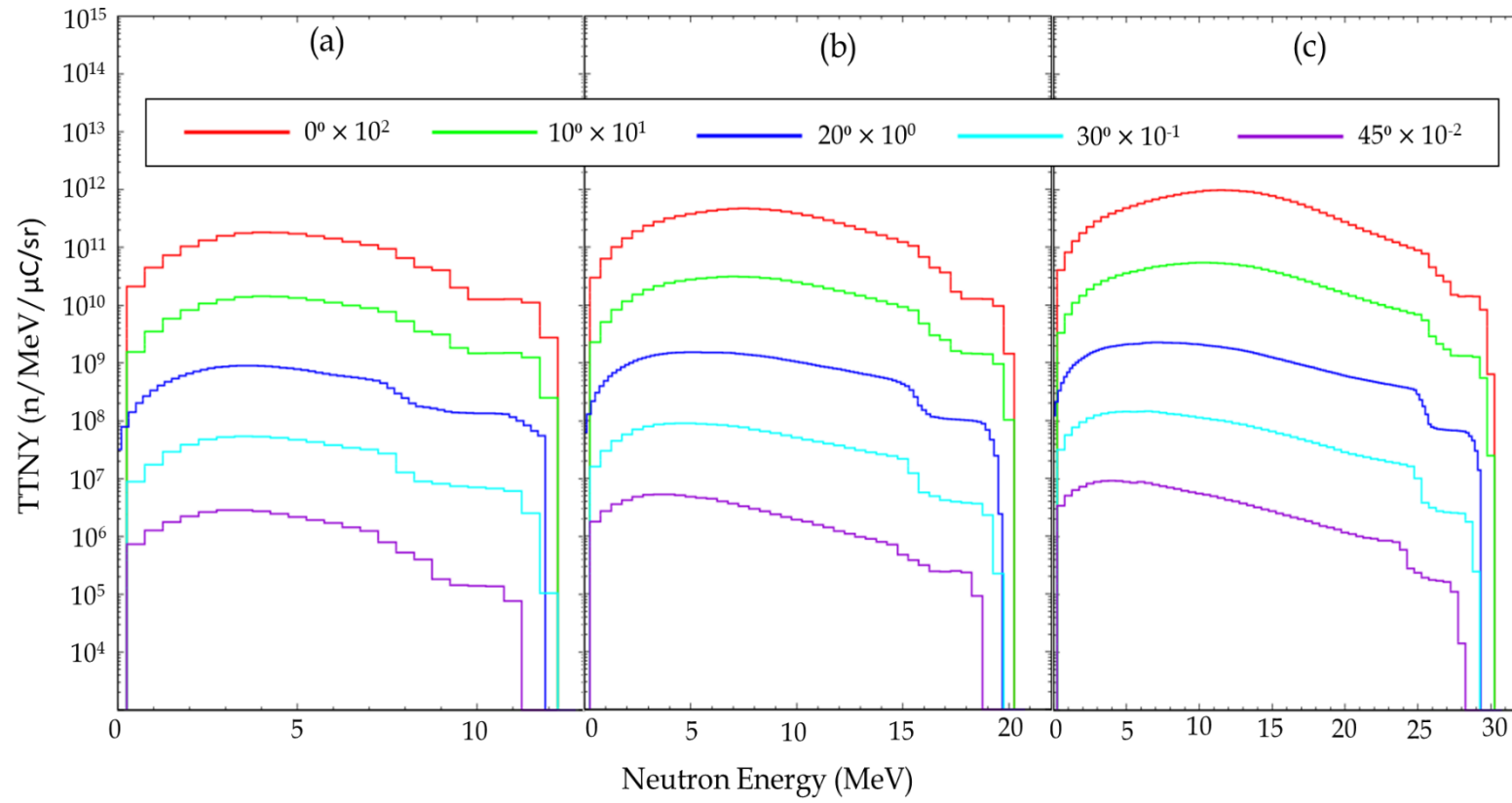


Fig. 2.4: Initial guess neutron spectrum calculated with DEURACS. For incident deuteron energy (a) 12 MeV, (b) 20 MeV, and (c) 30 MeV.

2.3 Results and Discussion

To obtain DDTTNY, the number of atoms and production rate were used as input data in the GRAVEL code. In addition to that, the initial guess neutron spectrum calculated with DEURACS also used as an input in the unfolding calculation. The convergence parameter, like the number of iterations, was adjusted in the calculation. Changing the number of iterations changes the χ^2 value and an example of it is shown in Fig.2.5. If the number of iterations is set to larger than the values for GRAVEL physically unacceptable structure is appeared in the unfolded DDTTNYs by over spectrum adjustment.

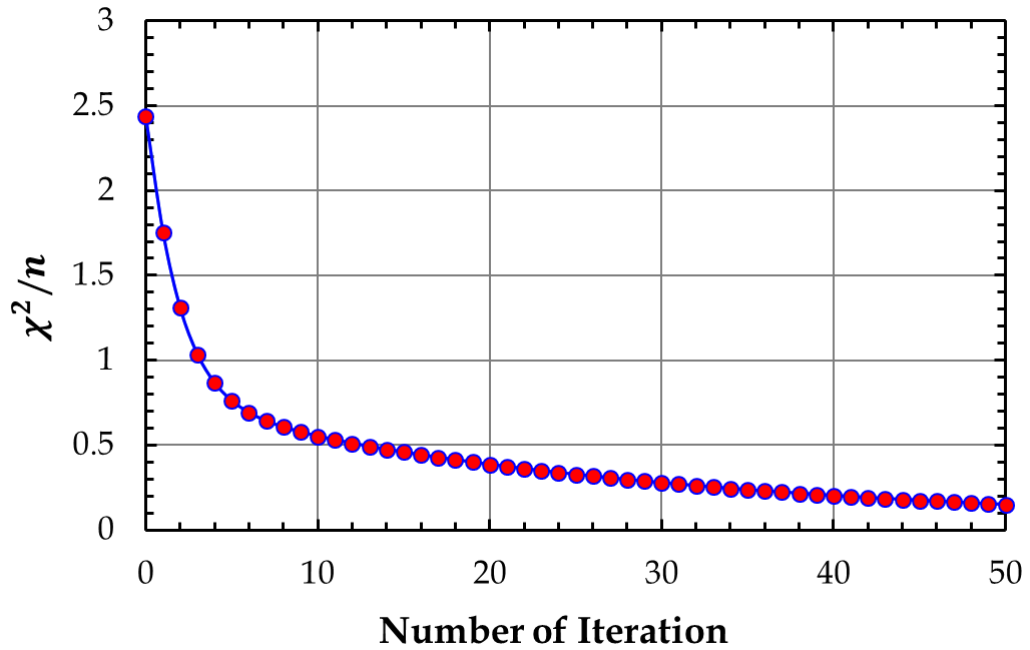


Fig. 2.5: Relationship between number of iteration and χ^2 . This example figure was determined for 30 MeV incident deuteron energy and at 10° of multiple-foil position. In this case, the number of iterations has been selected at the point where the curve tends to progress smoothly. This process of selection suggested that the number of iterations should be '10' in the case mentioned for this figure.

The unfolding DDTTNY can be derived with the input parameters for the GRAVEL code as mentioned above.

2.3.1 Double-differential thick-target neutron yield

Experimental DDTNYS on ^{nat}C unfolded using GRAVEL code are shown in Fig. 2.6. Since the experimental uncertainties tend to increase below neutron energy 2 MeV, the DDTNY was not determined in that range. At about 0° , a bump is observed about half the incident deuteron energy. The bumps devaluated with the neutron emission angles and shifted toward the lower neutron energy. The structure is caused by deuterons elastic breakup and non-elastic breakup reactions [35]. Moreover, step shapes are observed below incident deuteron energy, and they reflect discrete nuclear level structure of the residual nuclide, ^{13}N .

In Fig. 2.6(a), the DDTNYS of 12 MeV deuterons are in good agreement with Weaver *et al.* data [61] from 0° to 30° of neutron emission angle. Note that, the emission angles of the literature data are not the same as ours so that the absolute values of the spectra do not same in somewhat, and even Weaver *et al.* did not measure 45° DDTNY. The structure difference between our data and the reference data of the neutron spectrum after neutron energy 8 MeV is because of the different measurement processes made by Weaver *et al.* They measured neutron spectra by the TOF method. The foil activation method is sensitive to neutrons striking the foil materials from all directions. In contrast, the TOF method counts as neutrons arriving at the detector from a direction determined by the experimental setup. We compare our 20 MeV DDTNY data to the data measured by Weaver *et al.* at 18.09 MeV in Fig. 2.6(b). We observed it they have almost similar shapes, but different absolute values because of the incident deuteron energies variation. The spectrum shape at around 15 MeV neutrons showed dissimilarities because of different data acquisition techniques. For DDTNYS about 30 MeV deuterons, Shin's data [62] of 33 MeV deuterons at 0° is the only available data. The shape is consistent with our data as shown in Fig. 2.6(c). The mismatching of the obtained and the reference data may cause of the systematic and statistical uncertainties in the data measurement.

To validate the absolute neutron yields, Calculation/Experiment (C/E) values of the number of atoms were derived. The calculation of the number of atoms was obtained by folding the DDTNY with the production rate. Figure 2.7 shows the C/E values. The C/E values are around 1.0, and standard deviations are sufficiently small. It is found that the DDTNYS unfolded by GRAVEL have good experimental reproducibility.

Moreover, a comparison between the measured neutron spectrum and the DEURACS calculated initial guess spectrum for the neutron emission angle at 0° is shown in Fig. 2.8, as an example. Therefore, in the present work, the neutron spectrum was unfolded for the neutron energy more than 2 MeV to avoid large experimental uncertainty so that this comparison shows the values from neutron energy 2 MeV to its maximum values. Thus, for incident deuteron energy of 12 MeV, neutron yield magnitude in the measured unfolding spectrum was higher than the DEURACS spectrum, and vice-versa for 30 MeV incident deuteron energy. On

the other hand, for the incident energy of 20 MeV, the measured unfolding spectrum magnitude made a transition about 4 MeV. It is also showed that the reproducibility of the neutron yield for 30 MeV deuterons is better than for others. In contrast, in the lower deuteron energy range, the comparison does not appear flat which suggested that the DEURACS underestimates our results with increasing neutron emission energy.

2.3.2 Systematic Uncertainty Evaluation

The systematic uncertainties in the measured DDTTNYs are composed of some major components. If we sub-divide the uncertainty for each term into individual components and separate into the three stages of the measurement process, including pre-irradiation (sample preparation); irradiation; post-irradiation (γ -ray spectrometry).

- a) Pre-irradiation stage: sample masses and isotope natural abundance ratio.
- b) Irradiation stage: the ratio of neutron fluence rates (including fluence gradient & fluence variations with time, neutron self-shielding, absorption, and scattering) for a sample, effective cross-section, irradiation timing and decay corrections during irradiation (effects of half-life and timing uncertainties).
- c) Gamma-ray spectrometry stage: Measurement counting statistics (differences due to geometry and γ -ray self-shielding), effects of half-life, and timing uncertainties for each measurement i.e., from the end of irradiation to start of measurement, potential bias due to peak integration method and perturbed angular correlations (γ -ray directional effects).

However, in this research, the major sources of systematic uncertainties may come from the potential parameters defined in Eq. (2-1) and (2-2). As from the equations, the causes of systematic uncertainty are: mass and size of the foil, the half-life of the product nuclide, the γ -ray emission probability, the Ge detector photopeak detection efficiency, fitting calculation for the peak area of a γ -ray photopeak, the cooling and measurement time, the reaction cross-section data, the deuterons beam current measurement, and the solid angle of a foil from neutron source, respectively. But uncertainties of detector efficiency and activity of the standard source are estimated highest in the experiments. Other uncertainties are not as large as the uncertainties. Systematic uncertainty of detector efficiency is 3.8%, the activity of the standard source is 2.7% was estimated. Of course, systematic uncertainty comes from nuclear data also. So that, the actual value of systematic uncertainty may be increased. However, the contribution was not too much that can change the DDTTNYs results.

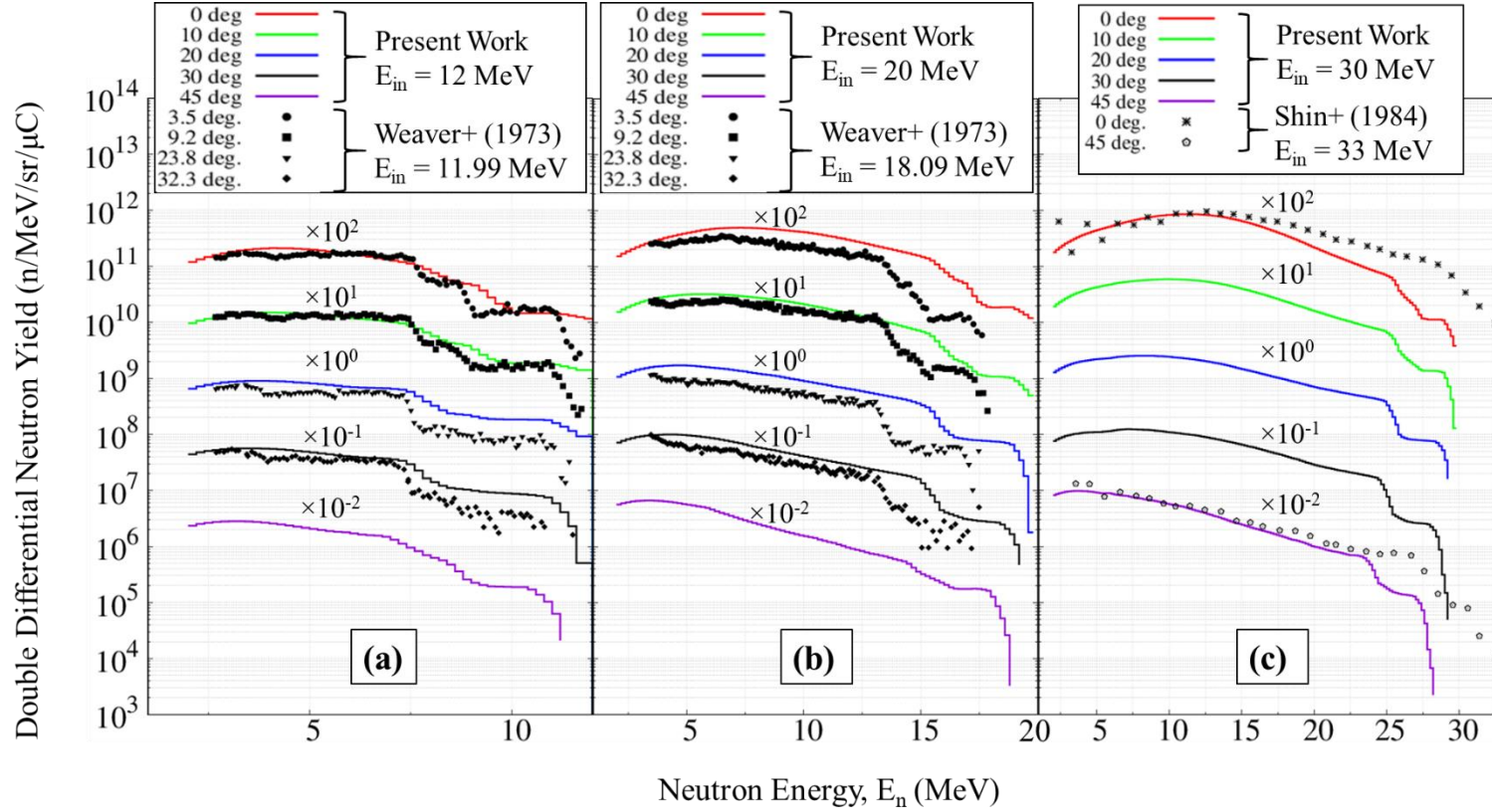


Fig. 2.6: Measured DDTTNs from thick ^{nat}C target, incident by (a) 12 MeV and compared with the published data of Weaver *et al.* at 11.99 MeV of deuteron [61], (b) 20 MeV and compared with the published data of Weaver *et al.* at 18.09 MeV of deuteron [61], (c) 30 MeV deuteron and compared with the published data of Shin *et al.* at 33 MeV of deuteron [62].

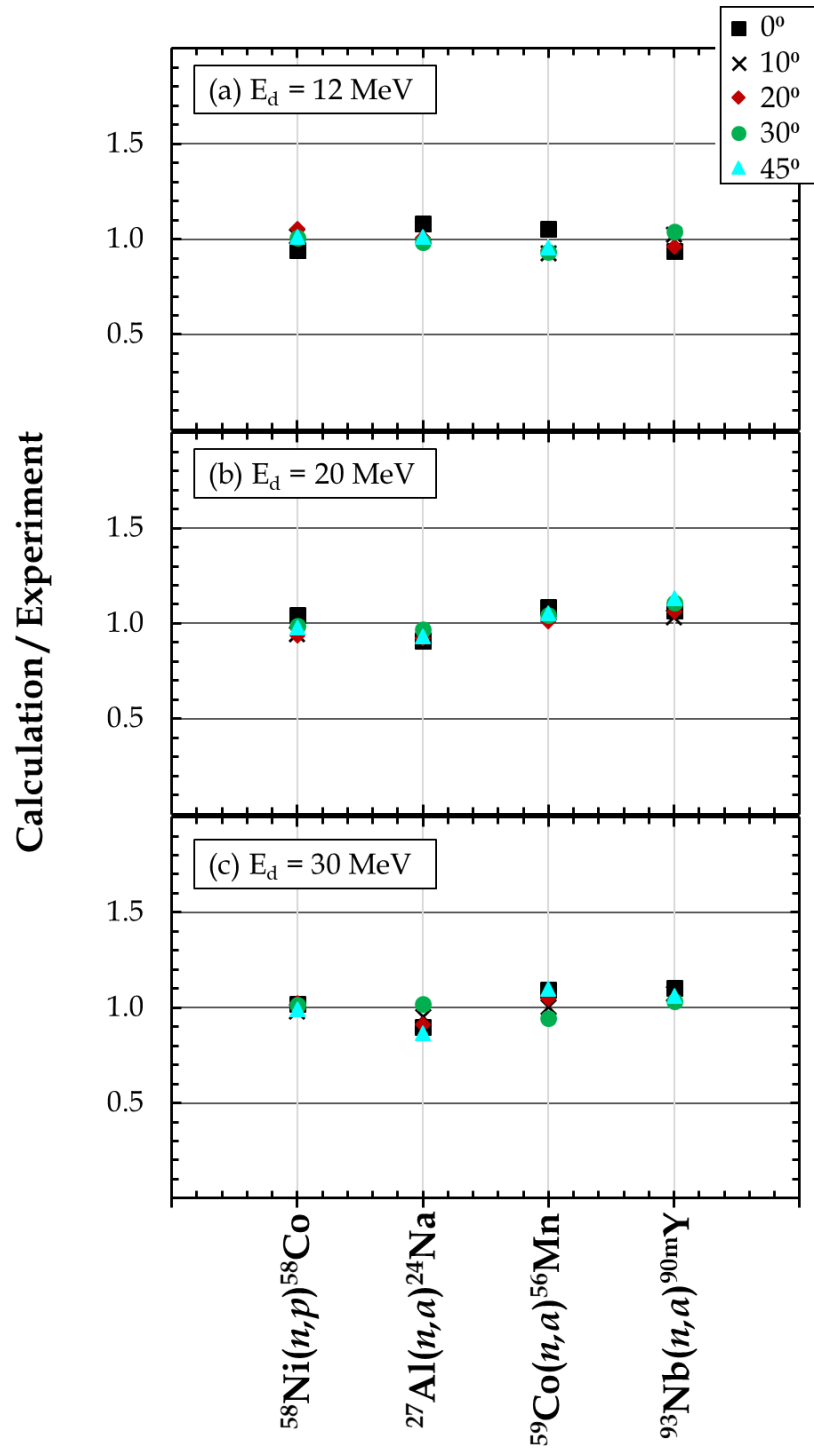


Fig. 2.7: Calculation/Experiment of number of atoms.

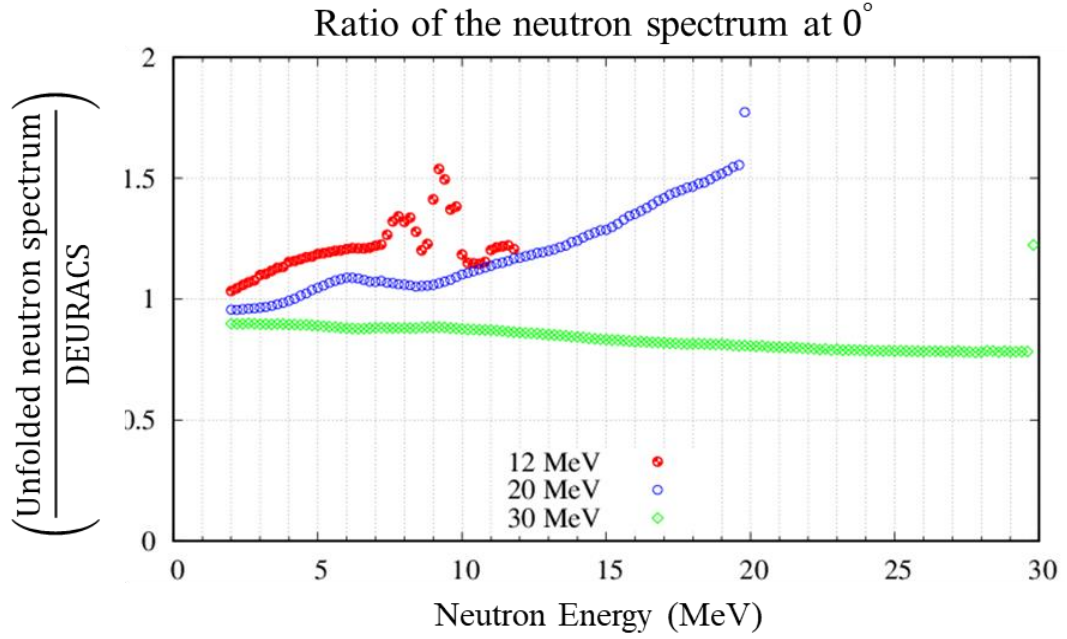


Fig. 2.8: Comparison between the unfolding neutron spectrum and the initial guess neutron spectrum calculated with DEURACS at 12, 20, and 30 MeV deuteron energies and neutron emission angle at 0° .

2.3.3 Angular differential neutron yields

To obtain angular differential neutron yields, the DDTTNYs were integrated from 2 MeV to the maximum neutron emission energy and the result is shown in Fig. 2.9 along with DEURACS calculation results. Forward-peaked distributions were observed clearly and there was no discrepancy between DEURACS and our results. For further discussion, we derived angular-differential neutron yields of multiple neutron energy groups as shown in Fig. 2.10.

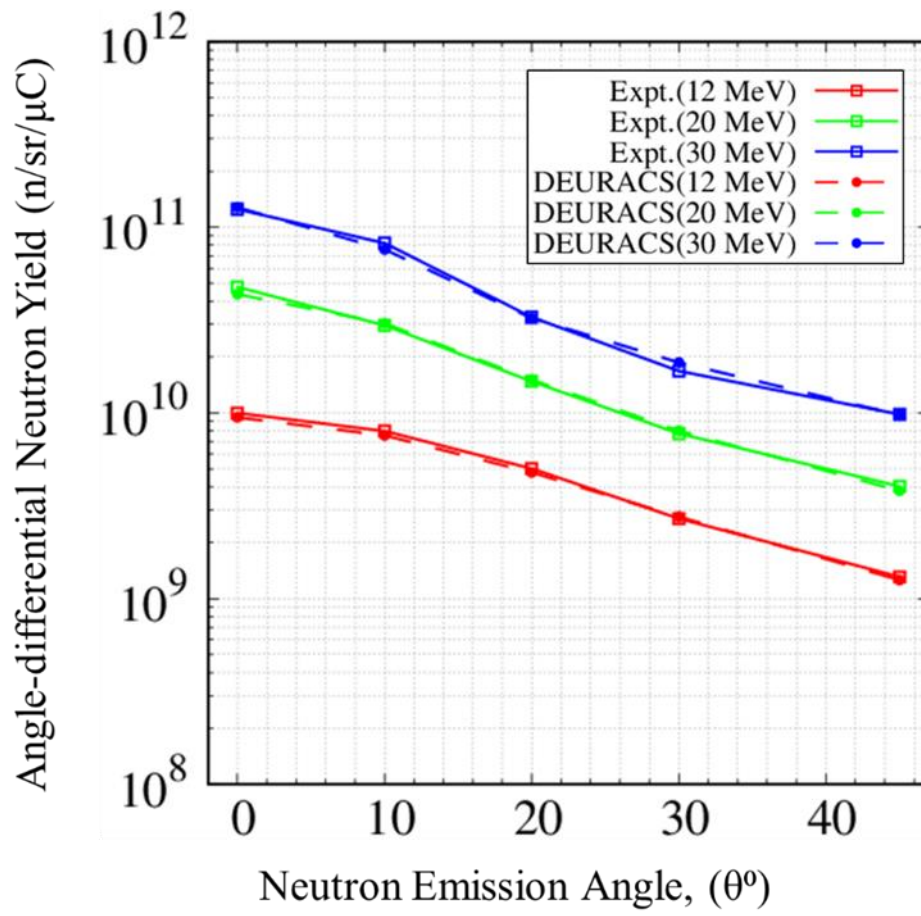


Fig. 2.9: Angular distribution of neutron yields for 12 MeV, 20 MeV, and 30 MeV deuterons.

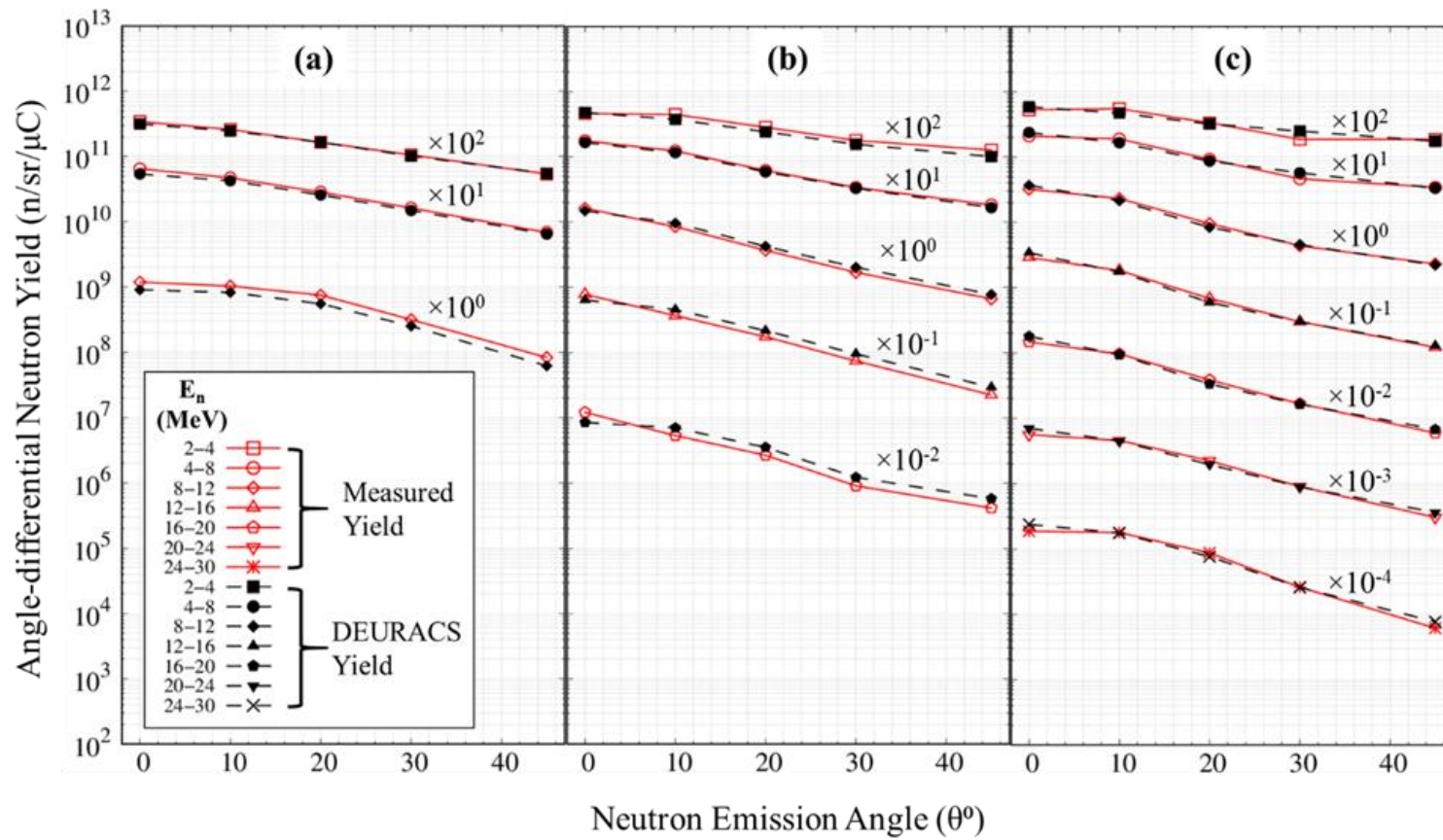


Fig. 2.10: Angle-differential neutron yield as a function of angle to beam axis for different neutron energy ranges for (a) 12 MeV, (b) 20 MeV, and (c) 30 MeV deuterons.

Neutron yields are derived by the integration of DDTTNYs over neutron energy and emission angle as shown in Fig. 2.11. Available experimental data for the total neutron yield of C(*d,n*) reaction are compared and also shown in the figure [31,51,61,63-68]. A blue line shows a fitting curve of the available data using the following formula:

$$Y(E_d) = (9.05 \times 10^5) \times (E_d)^{4.451} e^{-0.278 (\ln E_d)^2} \quad (2-3)$$

Our present data are situated on the fitting curve. Nevertheless, we did not record any experimental data between 18 MeV and 33 MeV because it is a large range, where the experiment data is unavailable. However, neutron data up to 50 MeV is crucial for most prominent medical RI production, especially, for 12 MeV, which vary slightly higher than the fitted line, but the value coincides with the data for 11.99 MeV deuteron measured by Weaver *et al.* [61]. This result is also higher than the fitted line. The other results in Ref. [61] for 14, 16, and 18.09 MeV deuteron energy show a similar tendency with our results of 12 MeV and 20 MeV deuterons. Also, the extrapolated trend agreed with our result for 30 MeV deuterons. The incident deuteron energy above 20 MeV is underestimated to the fitted curve; hence, it does not explain the drawbacks in our result at 30 MeV deuterons. However, it is notable that the points that we and other studies measured, which were less than $E_d = 20$ MeV, are indicated on the line shown in Fig. 2.11. The neutron yields given by almost all authors are in good agreement with the fitted line in the deuteron energy lower than 30 MeV.

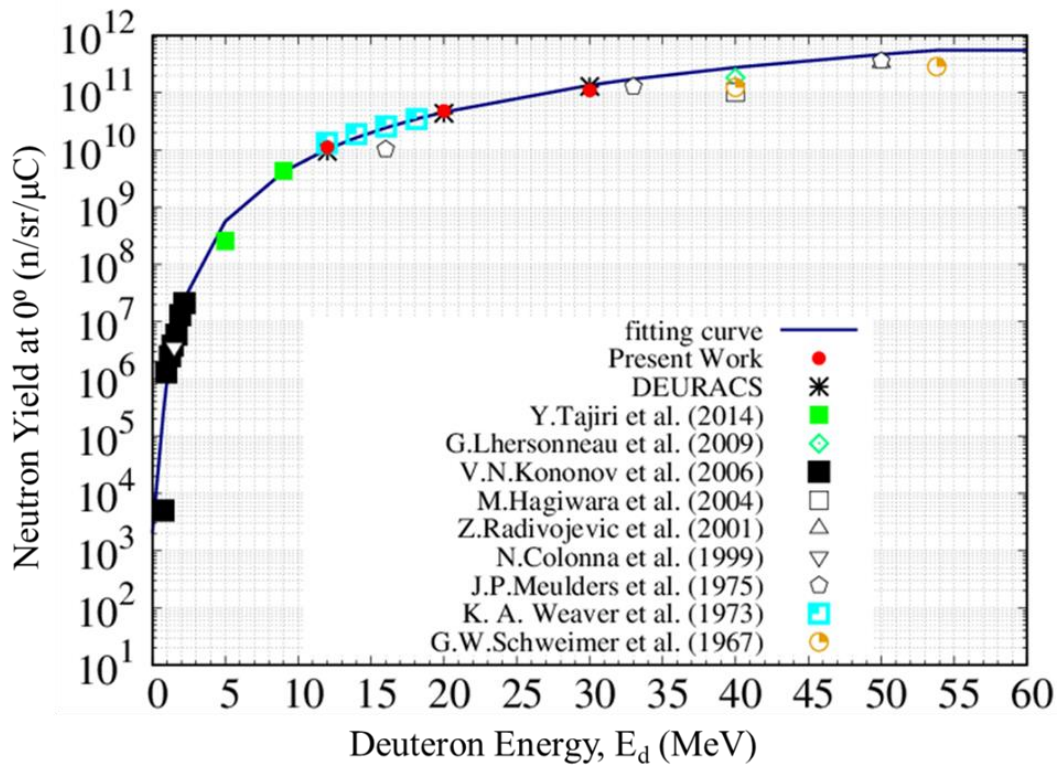


Fig. 2.11: Energy-integrated thick target neutron yield as a function of incident deuteron energy. For minimum neutron energy 2 MeV, the yield was calculated at an angle 0° to the beam axis, only.

2.3.4 Deuteron energy dependency of total neutron yield

An experimental total neutron yield per incident deuteron can be derived by integrating all the observed data over the angular and energy ranges. After proper normalization, the resultant neutron yield for the $C(d,n)$ reaction is shown in Fig. 2.12. The integrals are calculated: (a) with a neutron energy threshold of 4 MeV since several sets in the literature start at 4 MeV, and (b) for the neutron emission angles not larger than 45° from the beam direction. The curve in Fig. 2.12 is an empirical fitting function with the deuteron energy to the power of 2.16 and gives a trend established by the literature data from [62,64,66,67,69-71]. An overview of quantities useful for a quick calculation of neutron yields are listed in Table 2.4.

Since the neutron yields were measured at angles from 0° to 45° , the values corresponding to 20 MeV and 30 MeV deuterons are slightly higher than yields calculated at the same energy by other studies. Comparing with the other

experimental data by Lhersonneau *et al.* (2016) [69] shows the best similarity with our present measurement at 20 MeV and 30 MeV, which validated our measurement. However, it is noteworthy that the points we measured in the present work at $E_d = 20$, and 30 MeV are in good agreement with the interpolation from the literature data.

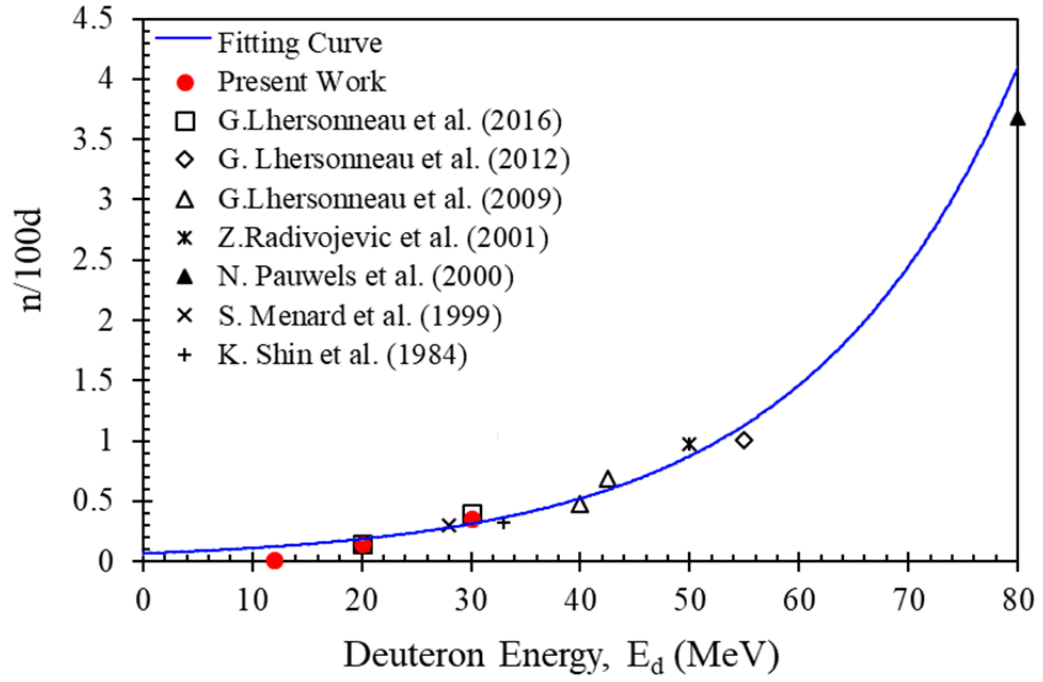


Fig. 2.12: Neutron yields for deuteron-induced reactions on ^{nat}C target up to $\theta = 45^\circ$ for various deuteron energies, representing the integrals of our work of 12, 20, and 30 MeV (red closed circle) and a few others from the literatures for carbon target. The fitting curve (blue curve) is only to guide the eye.

Table 2.4: Total neutron yields of energy ($= E_n$) higher than 4 MeV per 100 incident deuterons, ($n/100d$), and the integral of the yield per steradian per 100 incident deuterons, ($n/sr/100d$), and for maximum $\theta = 45^\circ$ in our measurements.

E_d (MeV)	($n/100 d$)	($n/sr/100 d$)	Ref.	Measurement Method
12	0.010	0.075	Present work	Activation
20	0.153	0.225	Present work	Activation
	0.192 ^a	-	[69]	
	0.146 ^b	0.064 ^c	[69]	
	0.130 ^d	-	[69]	
28	0.300 ^d	-	[71]	TOF
30	0.421	0.418	Present work	Activation
	0.490 ^a	-	[69]	
	0.403 ^b	0.165 ^c	[69]	
33	0.320 ^d	-	[62]	TOF
40	0.480 ^d	-	[64]	Activation
42.5	0.685 ^d	0.372	[64]	
50	0.970 ^d	-	[67]	TOF
55	1.010 ^d	-	[70]	Activation
80	3.680 ^d	-	[72]	TOF

^a $E_n < 1$ MeV, $\theta < 30^\circ$

^b $\theta < 30^\circ$

^c $E_n < 6$ MeV, $\theta = 30^\circ$

^d $\theta \leq 23^\circ$

2.4 Conclusion

This chapter analyzes the systematic measurement of DDTTNYs from deuteron bombardment on thick ^{nat}C target at incident energy 12, 20, and 30 MeV by multiple-foils activation method. The neutron energy spectra were unfolded by the GRAVEL code. The resultant DDTTNYs are compared with the results of the theoretical calculation code, DURACS. The measured DDTTNYs quantitatively reproduced for all incident energies at emission angles below 45° . We found that DURACS can be used for interpolation of the lacking experimental DDTTNY in the deuteron energy range from 12 MeV to 30 MeV for neutron emission angles of 0° to 45° . Further, other experimental data were included, and the empirical formulas were derived for the prediction of differential neutron yields at 0° and total neutron yield per incident deuteron over the wide range of energy. Therefore, this study provides accurate nuclear data of deuteron-induced reactions over a wide range of incident deuteron energy from 12 MeV to 30 MeV for ^{nat}C in the design of deuteron accelerator neutron sources.

3. Radioisotope Production by Accelerator-based Neutrons

This chapter will emphasize the deuteron accelerator-based neutron production method for RI production. As for the demonstration of the mentioned RI production method, an irradiation experiment and a Monte Carlo particle transport simulation will also describe for:

- A. the production and feasibility study of ^{132}Cs (which is an alternative tracer of ^{137}Cs), and
- B. the production of a medical RI, ^{47}Sc (which is applicable as a theranostic radionuclide for suitable RIT),

respectively.

A. Production of ^{132}Cs environmental tracer

A. 3.1 Background

At present, the dynamics of radioactive materials in the environment have received much attention. The behavior of radioactive cesium in the soil is especially important for avoiding public radiation exposure after a nuclear accident. On March 11, 2011, the Great East Japan Earthquake occurred, and following that the Fukushima Dai-ichi Nuclear Power Plant accident happened. After that, the Japanese government had no choice but revises the electric power generation deal, because of large amounts of ^{137}Cs and ^{134}Cs were released along with other radioactive materials during the accident [73,74]. Because the radioactive cesium isotopes ^{137}Cs and ^{134}Cs have longer half-lives (30 y and 2 y, respectively [56]) than the other RIs, they are dominant sources of public exposure at present [75-77]. From an environmental recovery perspective, the ^{137}Cs contribution is the most important. Radioactive cesium is strongly bound in soils [78] and sediment particles containing micaceous clay minerals (such as illite and vermiculite) [79]. Therefore, understanding cesium dynamics in the soil and sediment particles is important for environmental recovery. In other words, we should investigate how cesium is absorbed, the current microscopic states of cesium in the soil, and how these states can be removed by decontamination and volume reduction of contaminated soil.

Cesium dynamics can be understood by releasing a tracer that emits γ -rays, which are then intercepted by a radiation detector. In almost all researches, the tracer is ^{137}Cs itself. However, because this RI has a long half-life, radioactive waste must be measured for a long time after the research work. Thus, radioactive cesium with a shorter half-life is desired in these investigations.

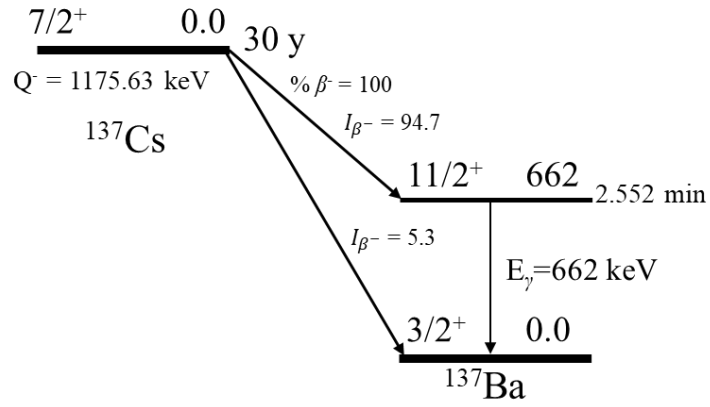
To encourage this avenue of study, Nagai et al. proposed a ^{132}Cs tracer generated by an accelerator [26]. The ^{132}Cs tracer has the following properties [80] (see also Fig. 3.1 (b)):

- 1) Cesium-132 emits 668-keV γ -rays with ~98% emission probability.
- 2) The half-life of ^{132}Cs is 6.5 d, very much shorter than that of ^{137}Cs (~30 y).
- 3) Cesium-132 can be produced via the $^{133}\text{Cs}(n,2n)$ reaction with accelerated neutrons.

The most intense gamma rays of ^{132}Cs have very similar energies to ^{137}Cs γ -rays (see Fig. 3.1), removing the need for correcting by the detection efficiency or the G(E) function. Meanwhile, the short half-life reduces the time and amount of radioactive waste management after the investigation. Moreover, the parent nuclide of the production method is ^{133}Cs , which accounts for 100% of the natural cesium. Therefore, even when using natural cesium as the target material, we can expect a high production yield with few by-product impurities. However, the production of ^{132}Cs from accelerator-based neutrons, and a feasibility study of ^{132}Cs as a replacement of ^{137}Cs tracer in different soil was not studied.

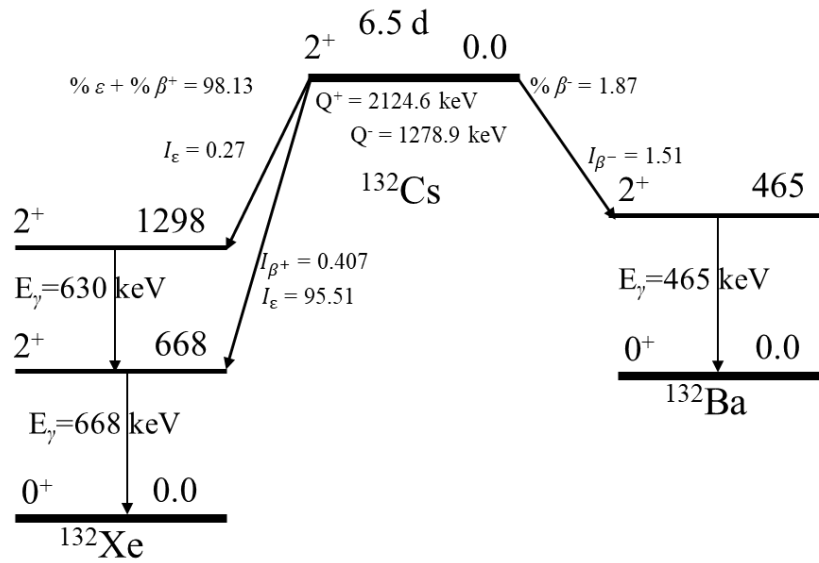
In an actual production experiment, this research investigates the quality of ^{132}Cs tracers produced via the $^{133}\text{Cs}(n,2n)$ reaction with accelerator-based neutrons. Next, a feasibility study of ^{132}Cs in andosol, haplic fluvisol, and gleyic fluvisol soil types sampled near the Fukushima Dai-ichi Nuclear Power Plant.

^{137}Cs β^- decay scheme



(a)

^{132}Cs β^- and ϵ decay scheme



(b)

Fig. 3.1: Decay schemes of (a) ^{137}Cs and (b) ^{132}Cs . Due to its short half-life, ^{132}Cs is a promising tracer of ^{137}Cs .

A. 3.2 ^{132}Cs production experiment

^{132}Cs can be produced via the $^{133}\text{Cs}(\gamma, n)$ [81] and $^{133}\text{Cs}(p, pn)$ [82] reactions by several routes. At this time, the optimal routes that maximize the ^{132}Cs yield have not been established, although the accelerator-based neutron method shows promise, so was chosen for the present study. More specifically, the ^{132}Cs was produced via the $^{133}\text{Cs}(n, 2n)$ reaction enabled by an accelerator neutron source. The neutrons were generated by bombarding deuterons onto a thick carbon target, initiating $\text{C}(d, n)$ reactions. Figure 3.2 shows the neutron-induced reaction cross sections on ^{133}Cs stored in EAF-2010 [58]. We selected the $\text{C}(d, n)$ reaction that generates the neutrons most effectively. Note also that the neutron-energy distribution of the $\text{C}(d, n)$ reaction has a broad peak around half of the incident deuteron energy [35]. Therefore, we can select the incident energy that optimizes the energy of the neutrons. To obtain the suitable neutron-energy distribution (around 17 MeV), we expected incident deuteron energies between 20 and 35 MeV.

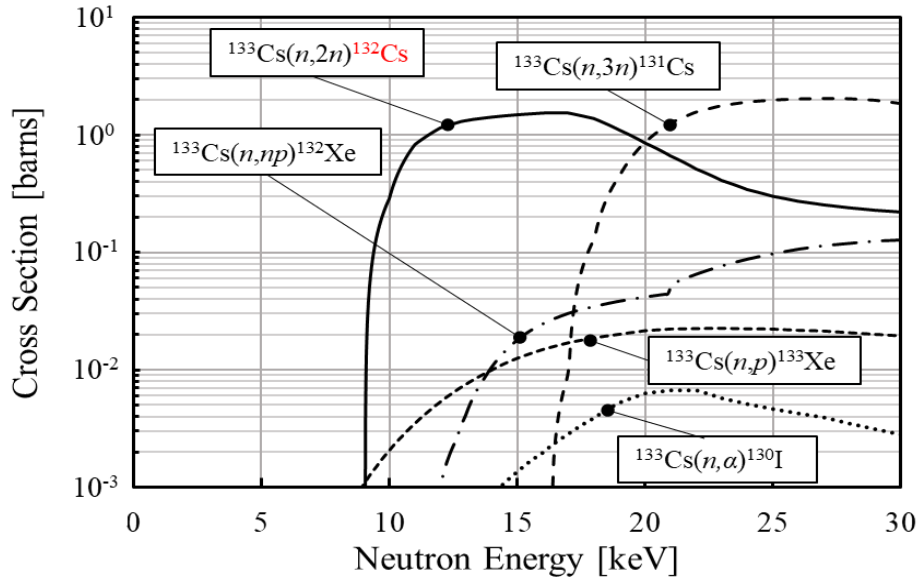


Fig. 3.2: Neutron-induced reaction cross-section of ^{133}Cs . The threshold energy of the ^{132}Cs production cross-section is approximately 9 MeV; from that point, the cross-section increases with neutron energy to its maximum at approximately 17 MeV.

A.3.2.1 Experimental facility

The ^{132}Cs production experiment was conducted at the Cyclotron and Radioisotopes Center (CYRIC) of Tohoku University, Japan [83]. Accelerator facilities at the CYRIC provide opportunities for implementing a broad research program, including medical research using positron emission tomography (PET), with accelerated ions and radioisotopes. The 930 type AVF cyclotron manufactured by Sumitomo Heavy Industries, Ltd. was used in this experiment. This accelerator can accelerate deuteron up to 10 to 50 MeV and can supply deuteron-based accelerator neutrons. The beam extension course is a course where neutrons are often used. In this experiment, we used a total of 32 beam courses. Figure 3.3 shows the positional relationship between the 930 type AVF cyclotron and its 32 courses.

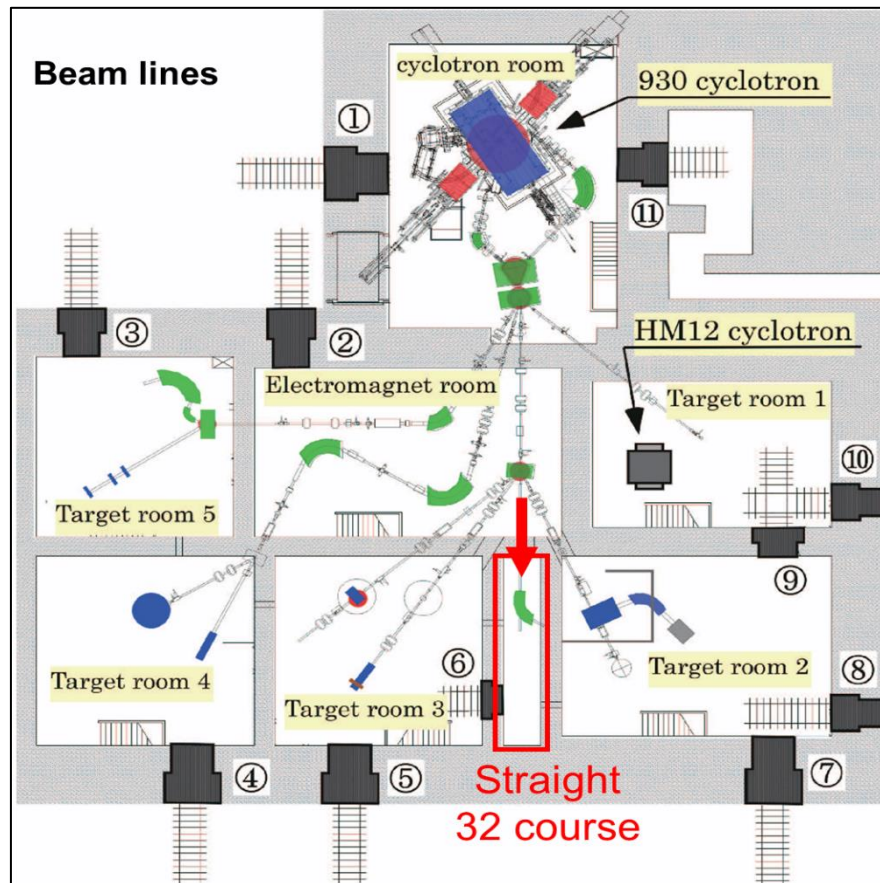
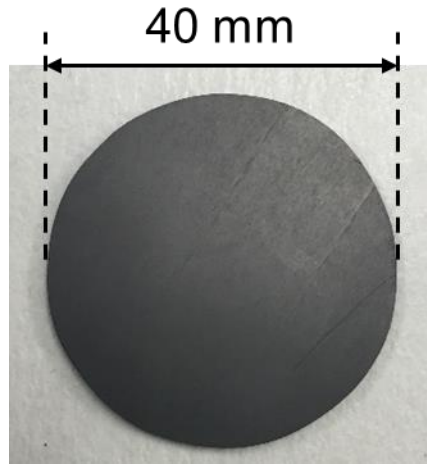


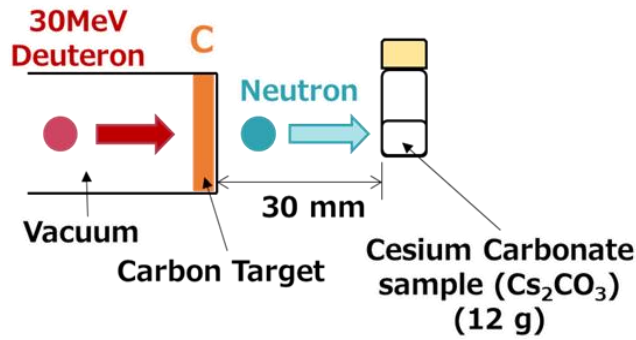
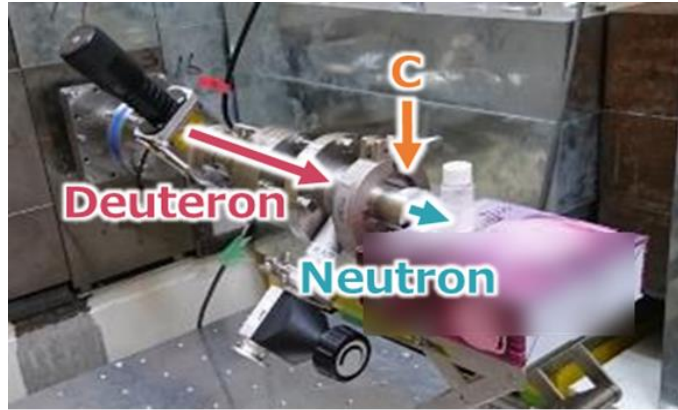
Fig. 3.3: Schematic view of 930 AVF cyclotron and its 32-course facilities in the CYRIC. (Excerpted from ref. [84].)

A.3.2.2 Experimental conditions

Deuterons were accelerated to 30 MeV by the accelerator and bombarded onto a circular-shaped thick carbon target 40 mm in diameter and 4 mm thick which is shown in Fig. 3.4(a). This carbon target has a purity of 99.99% (supplier: The Nilaco Corporation, Tokyo, Japan [54]). The thickness of the carbon target was set so that the deuterons stopped completely. As a result, accelerator neutrons are obtained by the $C(d,n)$ reaction. The generated neutrons were irradiated onto a 12-g cesium carbonate (Cs_2CO_3) sample placed 30 mm downstream of the carbon target and 0° to the beam axis. The average deuteron beam current during the irradiation was 1.2 μA . Figure 3.4(b) shows a photograph and a schematic of the irradiation setup. After irradiating for 2 hours, the γ -rays emitted from the sample were measured by a high-purity germanium (HP Ge) detector (ORTEC GMX50P4-83-RB-B-PL). The measured sample was placed 150 mm from the front head of the HP Ge detector. To derive the peak detection efficiency for this sample, a 227-kBq standard gamma-ray source of ^{137}Cs was placed and measured at the same position from the detector. The detector and the measured sample were surrounded by lead blocks to reduce the natural background radiation.



(a)



(b)

Fig. 3.4: (a) Carbon target, and (b) photograph and schematic view of the irradiation setup.

A. 3.2.3 Measurement of irradiated sample

Figure 3.5 shows the spectrum of the γ -rays emitted from the irradiated Cs_2CO_3 sample. The γ -rays from ^{132}Cs are clearly observed, and the other photo-peaks correspond to the decay of γ -rays from ^{130}I ($E_\gamma = 536.07 \text{ keV}$ and $T_{1/2} = 12.36 \text{ h}$) and $^{134\text{m}}\text{Cs}$ ($E_\gamma = 127.5 \text{ keV}$ and $T_{1/2} = 2.912 \text{ h}$). The activity of the ^{132}Cs produced in the irradiation experiment was approximately 102.2 kBq/g , with a radioactive purity of 98%. This value is comparable to the estimated activity of ^{132}Cs as we calculated before the experiment by considering the experimental conditions. The dominant by-products were ^{130}I (1.88 kBq/g) and $^{134\text{m}}\text{Cs}$ (0.311 kBq/g). The activity ratios of ^{130}I and $^{134\text{m}}\text{Cs}$ to ^{132}Cs were only 1.8% and 0.3% respectively. Besides their low activity, these by-products have shorter half-lives than ^{132}Cs , so their contributions can be reduced by cooling after the ^{132}Cs -production irradiation.

Accordingly, the influence of the by-products was negligible. Although the longer half-life of the Cs isotope $^{134\text{m}}\text{Cs}$ ($T_{1/2} = 2.07$ y), is problematic for disposal handling, its contribution to the ^{132}Cs production was also negligible. Therefore, the by-products of this production experiment are unimportant in waste management. In conclusion, neutrons generated by a state-of-the-art accelerator-based neutron enable the production of high-quality and manageable ^{132}Cs .

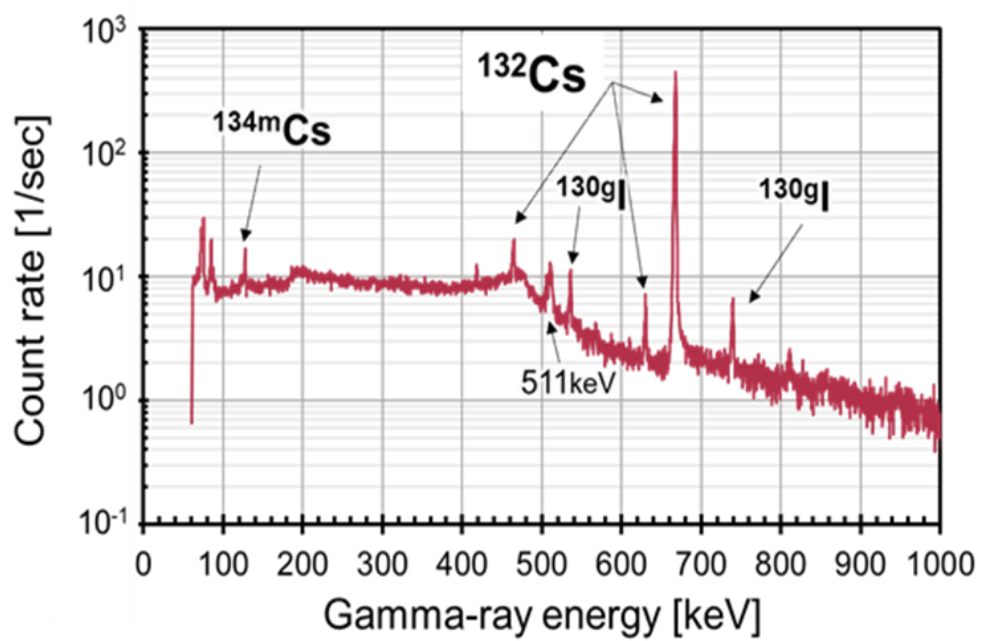


Fig. 3.5: γ -ray spectrum of the Cs_2CO_3 sample irradiated with accelerator-based neutrons.

A. 3.3 Feasibility study of ^{132}Cs tracer for environmental study

A. 3.3.1 Experiment

In the next step, the success of ^{132}Cs as an environmental tracer was investigated in a feasibility study. For this purpose, this research conducted a soil-absorption experiment using the produced ^{132}Cs tracer. The soil samples were andosol, haplic fluvisol, and gleyic fluvisol were provided by the Fukushima Agricultural Technology Centre, Japan, and sampled at their experimental sites where no contamination observed by the Fukushima Dai-ichi Nuclear Power Plant accident pollution.

Figure 3.6 is a schematic view of the measurement setup. First, the sampled soils were packed into individual acrylic cylinders ($\phi 30 \text{ mm} \times 200 \text{ mm}$) to a height of 150 mm. The density of the packed soil into the column is 1.215 g/cm^3 for haplic fluvisol, 1.076 g/cm^3 for andosol, and 1.224 g/cm^3 for gleyic fluvisol soil. Next, an aqueous solution of ^{132}Cs was made by dissolving the irradiated Cs_2CO_3 sample in 1 L of distilled water. This aqueous solution was dropped into the packed soil samples, maintaining a mass ratio of 5:1 between the soil and the solution.

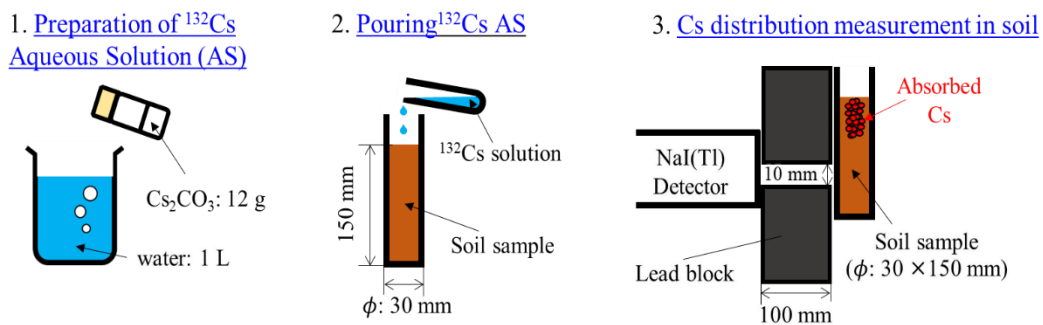


Fig. 3.6: Measuring the vertical distribution of ^{132}Cs activity in soil samples. Distributions were measured in three types of soil samples: haplic fluvisol, andosol, and gleyic fluvisol soil.

The vertical cesium distributions were derived from the γ -rays emitted by the ^{132}Cs tracer. Measurements were taken at 10-mm intervals in the depth direction (starting from the soil surface) using a NaI (Tl) detector (EMF211, EMF Japan Co., Ltd.). A lead collimator was placed in front of the NaI(Tl) detector to eliminate ^{132}Cs gamma rays outside the region of interest.

A. 3.3.2 Results and Discussion

Figure 3.7 shows the vertical distributions of the ^{132}Cs activities in the haplic fluvisol, andosol, and gleyic fluvisol soil samples in which their total activity is 30.72 kBq, 33.57 kBq, and 46.19 kBq respectively. In all samples, the ^{132}Cs was absorbed near the soil surface. Almost 100% of the ^{132}Cs was absorbed within 40 mm from the soil surface. The ^{132}Cs distribution decreased along the vertical direction. The different absorption patterns reflect the different taxonomies and compositions of the three soils. However, as is widely known, cesium is absorbed within the first 10 cm in the dominant soil types (andosol soil, forest and grassland soil, and fluvisol soil) [85-89].

Previous studies have investigated the soil absorption of ^{137}Cs γ -rays [88,90-92]. For example, Ohno *et al.* [90] analyzed the ^{137}Cs distribution in soil samples collected within a 60-km west of the Fukushima Dai-ichi Nuclear Power Plant at one month after the accident. Almost 100% of the ^{137}Cs in their experiment were detected within 40 mm from the ground surface. Similar behavior was observed in the present experiment using the ^{132}Cs tracer. Therefore, we concluded that ^{132}Cs is a plausible alternative tracer to ^{137}Cs to investigate the Cs-adsorptive nature of the soil.

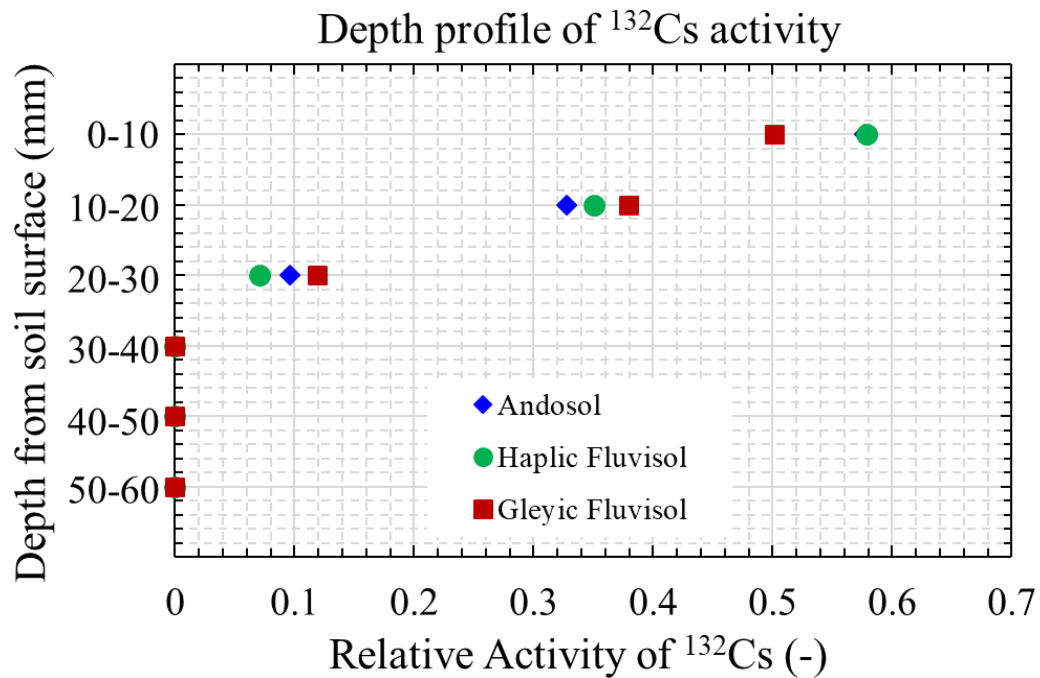


Fig. 3.7: Vertical distributions of ^{132}Cs activity in the three soil samples. The measured points are the relative activities of ^{132}Cs at the respective soil depths. The activity distribution remains steady after 40 mm.

A. 3.4 Summary

^{132}Cs was proposed as a promising alternative environmental tracer to ^{137}Cs . To study its tracing feasibility, this research first determined the production amount and radioactive purity of ^{132}Cs in a production experiment. The $^{133}\text{Cs}(n,2n)^{132}\text{Cs}$ reaction, initiated by irradiating 30 MeV deuterons on a thick carbon called neutron converter, yielded 102.2 kBq/g of ^{132}Cs with a radioactive purity of 98% after irradiation. Since the activity of ^{134g}Cs after decay of ^{134m}Cs has very small and it is negligibly small compared to the activity of ^{132}Cs , so it can be eliminated after a few days of cooling. Next, a feasibility study of the produced ^{132}Cs was conducted. The cesium absorptions to andosol, haplic fluvisol, and gleyic fluvisol soil particles were measured by an NaI(Tl) gamma-ray detector. Almost 100% of the ^{132}Cs was distributed within 40 mm from the surfaces of all soil samples. The results are consistent with previous studies on ^{137}Cs soil absorption. So that ^{132}Cs can replace ^{137}Cs as an environmental tracer. More information on this research can be found in the published article in ref. [93].

B. Application to Medical Radioisotope Production

B. 3.1 Background

The major use of RI being in nuclear medicine, in both diagnosis and internal radiotherapy. Each application, however, demands a special kind of RI. For in vivo diagnostic investigations involving organ imaging, for instance, RIs are required which will be efficiently detected from outside of the body. To this end, short-lived γ -ray emitters (like ^{99m}Tc [$T_{1/2} = 6.0$ h], ^{123}I [$T_{1/2} = 13.2$ h], and ^{201}Tl [$T_{1/2} = 3.06$ d]) and positron emitters (like ^{11}C [$T_{1/2} = 20.3$ min], ^{18}F [$T_{1/2} = 109.8$ min], ^{64}Cu [$T_{1/2} = 12.7$ h], and ^{68}Ga [$T_{1/2} = 1.03$ h]) are commonly used in SPECT and in PET, respectively. The underlying principle in diagnostic nuclear medicine is that the radiation dose to the patient is as low as possible, compatible with the desired quality of imaging, and also the diagnostic advantage compared to non-radioactive methods. Thus, an entire set of decay data of a RI is required to be able to calculate the radiation dose which plays a very important role in its choice for a diagnostic medical application. In contrast, for internal radiotherapy, RIs emitting corpuscular radiation (α or β^- particles, conversion and/or Auger electrons) are of interest, e.g., α emitters (^{211}At [$T_{1/2} = 7.2$ h] and ^{223}Ra [$T_{1/2} = 11.4$ d]), β^- emitters (^{89}Sr [$T_{1/2} = 50.5$ d], ^{90}Y [$T_{1/2} = 2.7$ d], ^{131}I [$T_{1/2} = 8.02$ d], and ^{177}Lu [$T_{1/2} = 6.7$ d]), and Auger electron emitters (^{125}I [$T_{1/2} = 60.0$ d] and ^{103}Pd [$T_{1/2} = 17.0$ d]). Since in this case, a localized, well-defined radiation dose needs to be deposited in malignant or inflammatory tissue, RIs emitting low-range highly ionizing radiation is of great interest.

The medical RI production technology is well developed and is pursued both at commercial centers and a few nuclear science research institutes. However, besides routine production and medical application of RIs, constant research work goes on around the world to boost the present production methodologies of some established RIs even on the development of novel RIs for new medical applications. Some thoughts and efforts are also constantly dedicated to the long-run development of this technology to fulfill the challenges of the latest approaches in medical investigations.

The production of RIs is carried out using nuclear reactors and accelerators/cyclotrons [94,95]. The reactor production generally results in neutron excess RIs mostly decay by β^- emission and are therefore especially suitable for RIT. Besides, the cyclotron produced RIs are mainly decay by electron capture (EC) or β^+ emission. They are therefore particularly useful for diagnostic studies. The positron emitters can be produced only at cyclotrons. For the production of some RIs, both nuclear reactors and cyclotrons are extensively used. The RI production technology today has thus become an integral part of modern nuclear medicine and its prospects also appear to be bright.

B. 3.2 Production of radioisotopes with accelerator neutrons by deuterons

This research focused on the RI production with accelerator-based neutron by deuterons. The accelerator neutron method is a method of irradiating a thick target called neutron converter with deuterons which are generated by the deuteron accelerator. By irradiating the generated neutrons to the irradiation target, a neutron-induced reaction occurs, and various RIs can be produced. Since it is a small-scale facility compared to a nuclear reactor, it can be built inside the hospital or a cancer diagnosis and treatment providing an area for a stable supply of the radiopharmaceuticals. The schematic diagram of the accelerator-based neutron method is shown in Fig. 3.8. The neutrons enter the neutron converter and produced neutrons. The neutrons are further illuminated on the target to produce medical RI. In developing a medical RI producing method using this technique, it is necessary to evaluate the effective irradiation system design and production amount. To do so, the incident particles of neutron's thick neutron yield distribution, DDTTNYs are required. Details of DDTTNYs were described in Chapter 2. Note that, in this research, unfolding DDTTNYs were measured for 12, 20, and 30 MeV incident deuteron energy, and for neutron emission angle 0° , 10° , 20° , 30° , and 45° .

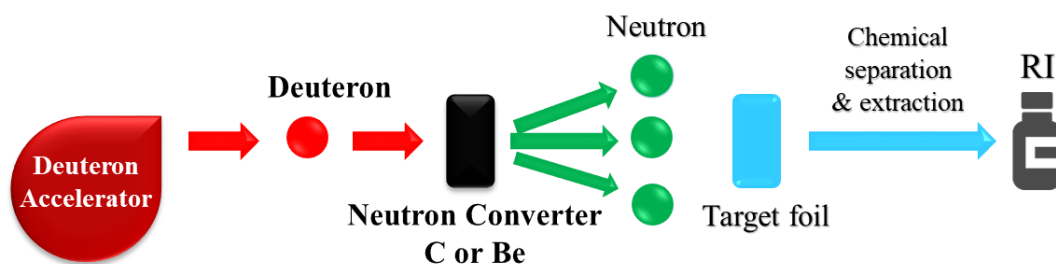


Fig. 3.8: Schematic diagram of medical RI production by accelerator-based neutrons method with deuterons.

B. 3.3 Production amount and purities of radioisotopes

One of the major aims of the development of the RIs production method by accelerator-based neutron by deuteron is to maximize the production yield of the desired product and to minimize the impurity level of by-product/s. Since the energy distribution of the accelerator-based neutrons with the $C(d,n)$ reaction can be adjusted by changing the incident deuteron energy so the appropriate deuteron energy can be determined to produce high-purity RI by investigating all the neutron excitation functions of possible reactions involving the stable isotopes of the target material. Moreover, in the production method, two types of problematic byproducts had to be considered: radioactive byproducts that could be problematic during target treatment of chemical processes, and carriers. Because the carriers cannot be chemically separated from the product, they result in a low-specific radioactivity, i.e., a low labeling index for the medicine.

The discussion in the above paragraph showed that nuclear data play an important role in the production and application of RIs in medicine. It should also be explicitly mentioned that the chemical form of the RI and its biochemical behavior are perhaps of greater significance regarding the application.

It can mention that the production amount and purities of some emergent medical RIs already estimated by some authors as for the feasibility study of the accelerator-based neutron by deuterons. For example, Kin *et al.* precisely described the estimation of production amount and the purities of promising PET tracer ^{64}Cu [18,20], novel therapeutic RI, ^{67}Cu [19], ^{92}Y [21]. Also, Nagai *et al.* propose a production method of ^{99}Mo , which is the mother nuclide of the most used medical RI, $^{99\text{m}}\text{Tc}$ [24]. His group also studied the production of a diagnostic RI, ^{90}Y with accelerator-based neutron method [25], and so on. However, the production amount and the purities of these RIs are already well established. To extend the feasibility

study of the accelerator-based neutron method, the production procedures of an emergent medical RI, ^{47}Sc ($T_{1/2} \approx 3.35$ d [56]) is described in this research.

B. 3.3.1 Production Amount and Purities of ^{47}Sc

^{47}Sc is a promising candidate for RI therapy. It has desirable nuclear properties since it is a β^- emitter with a ~ 3.35 d half-life, which may be suitable for small-molecular-weight ligands, considering their rapid pharmacokinetics. Also, ^{47}Sc has a primary γ -ray at 159 keV ($\sim 68\%$) that is suitable for SPECT imaging [96,97]. Sc also shows favorable elements for conjugation to antibody-chelate systems. Therefore, this radioisotope can be used for the treatment and diagnosis of tumors.

The availability of high ^{47}Sc activity with adequate purity becomes a crucial issue for the realization of more detailed preclinical investigations and future clinical applications. so far, the successful production of ^{47}Sc was described by two different neutron-induced reactions: $^{47}\text{Ti}(n,p)^{47}\text{Sc}$ and $^{46}\text{Ca}(n,\gamma)^{47}\text{Ca} \rightarrow ^{47}\text{Sc}$ (see Fig. 3.9) [98-100]. To produce ^{47}Sc from ^{47}Ti , fast neutrons ($E_n > 1$ MeV) are required, while the $^{46}\text{Ca}(n,\gamma)^{47}\text{Ca}$ reaction is induced by thermal neutrons ($E_n = 0.025$ eV) [98]. Proton irradiation of enriched ^{48}Ti targets made ^{47}Sc available via the $^{48}\text{Ti}(p,2p)^{47}\text{Sc}$ nuclear reaction, however, too much of the long-lived ^{46}Sc was coproduced [101]. An alternative ^{47}Sc production route considers photonuclear reactions on enriched ^{48}Ti and ^{48}Ca targets, respectively [102-106]. So far only the former route was studied in detail with enriched targets [102], while for the latter only natural target material was used for initial benchmark experiments.

This research investigates the production amount and other nuclear data of ^{47}Sc via $^{47}\text{Ti}(n,p)^{47}\text{Sc}$ reaction. This is one of the main nuclear reaction for ^{47}Sc production [107].

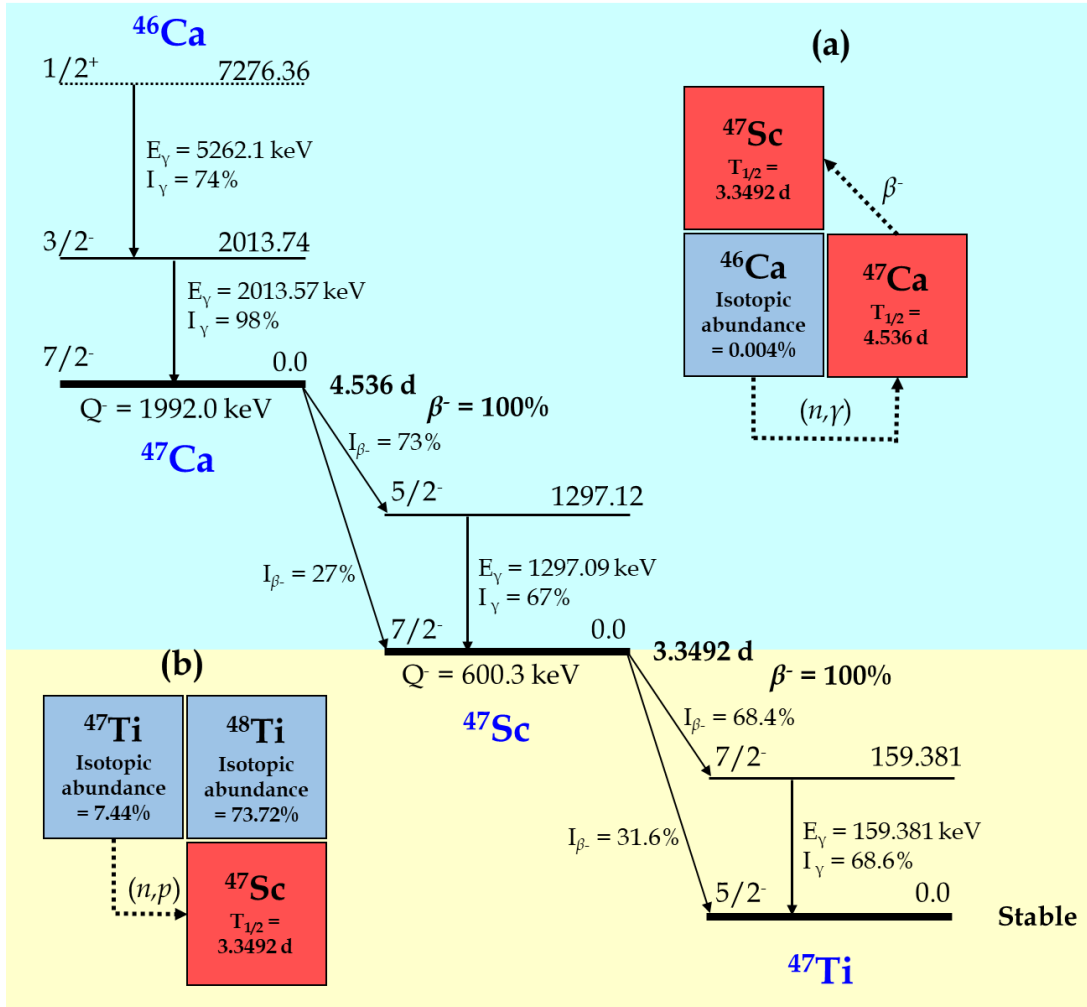


Fig. 3.9: Nuclear data for production of ^{47}Sc from (a) ^{46}Ca via $^{46}\text{Ca}(n,\gamma)^{47}\text{Ca} \rightarrow ^{47}\text{Sc}$ and (b) from ^{47}Ti via $^{47}\text{Ti}(n,p)^{47}\text{Sc}$.

B. 3.3.2 Production method

In the production method, ^{47}Sc would be produced via the $^{47}\text{Ti}(n,p)$ reaction based on an accelerator neutron source from $\text{C}(d,n)$ reaction. This research proposed a new method based on the accelerator-based neutron by deuterons method. Figure 3.10 shows the neutron excitation function of ^{47}Ti stored in the European Activation File (EAF-2010) [58].

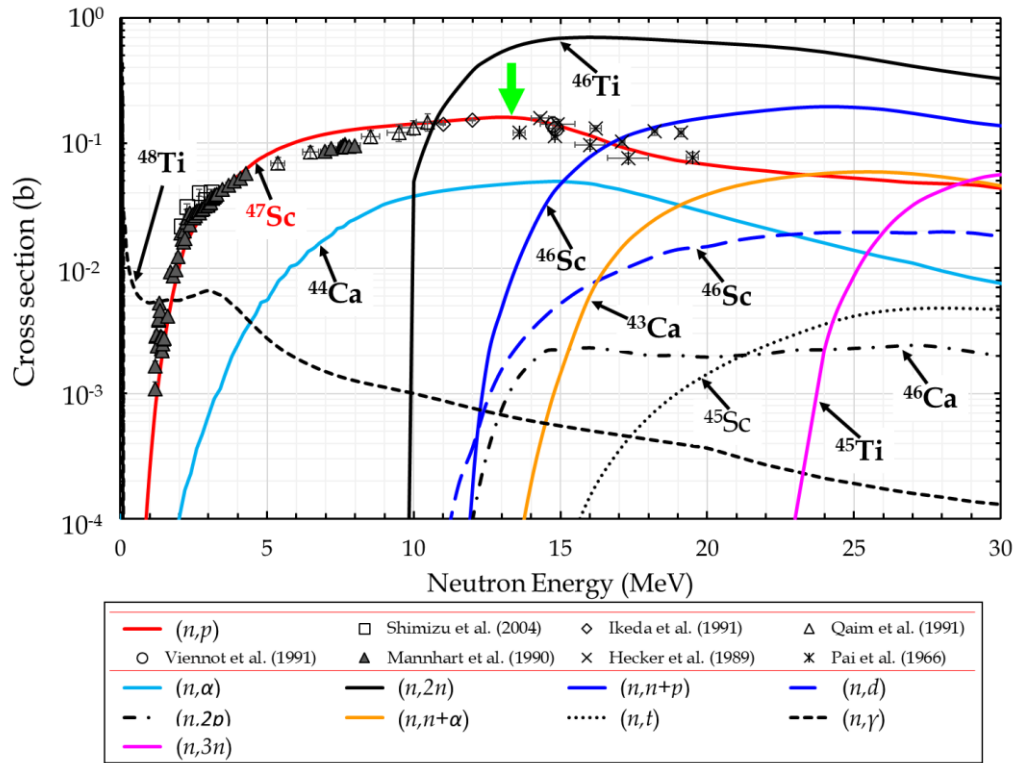


Fig. 3.10: Excitation function of neutron-induced reactions on ^{47}Ti . The red line shows the production reaction of ^{47}Sc . Green arrow indicates the maximum production cross-section point for the corresponding neutron energy approximately 14 MeV. The experimental values of $^{47}\text{Ti}(n,p)^{47}\text{Sc}$ cross-section were taken from the Experimental Nuclear Reaction Data library (EXFOR) [29].

For ^{47}Sc production reaction, the cross-sections were consistent with experimental values by Shimizu *et al.* [108], Ikeda *et al.* [109], Qaim *et al.* [110], Viennot *et al.* [111], Mannhart *et al.* [112], Hecker *et al.* [113], and Pai [114]. The threshold energy for the production cross-section is approximately 0 MeV, and from that point on the value increases with neutron energy to achieve a maximum of around 14 MeV.

Among all by-products, the nuclides that cannot be separated by chemical processes should be considered to estimate the radioactive and isotopic purities of the ^{47}Sc product. From Fig. 3.10 it is seen that isotopes of calcium and titanium may produce with scandium isotopes. In the higher energy region, $^{45,46}\text{Ti}$, ^{43}Ca , and ^{46}Sc shows higher reaction cross-section than that of ^{47}Sc . Since the radiochemical

processing of ^{47}Sc from irradiated ^{47}Ti target is well established [96,99,115]. So that almost all by-products can be treated chemically and then purified ^{47}Sc can be obtained easily. However, RI ^{46}Sc ($T_{1/2} = 83.79$ d [56]), and stable isotope, ^{45}Sc could be problematic in the production yield of ^{47}Sc . Especially, ^{46}Sc affects not only isotopic but also radioactive purities. Therefore, the amount of by-products should be kept at a low level.

To produce optimum ^{47}Sc , the requirement of the neutron energy distribution can be noted as follows;

- 1) High intensity is required near the energy that corresponds to the maximum cross-section of $^{47}\text{Ti}(n,p)$ reaction to produce a sufficient amount of ^{47}Sc .
- 2) The high-energy component of the neutron beam over 14 MeV should be avoided to suppress by-products, especially, ^{45}Sc and ^{46}Sc .

Since neutrons are produced via the $\text{C}(d,n)$ reaction and this reaction has been selected because of the energy spectrum features a broad peak around half the incident deuteron energy as a consequence of elastic and non-elastic breakup reactions [35]. In other words, the energy distribution is often adjusted by the selection of incident deuteron energy. Suitable energy ranges to produce the above-mentioned distribution is anticipated to be between incident deuteron energy 20 and 30 MeV. But this research, consider the neutron production from 12, 20, and 30 MeV deuterons on thick target as a feasibility study. So, it is aimed that estimation of the ^{47}Sc production yields, the radioactive and isotopic purities can be optimized longitudinally up to 30 MeV deuteron energy. They can estimate by the procedure of ^{47}Ti target irradiation using the measured thick target neutron yield (TTNY) of the $\text{C}(d,n)$ reaction. This procedure can be done by using a general-purpose Monte Carlo particle transport simulation code, PHITS [32].

B. 3.3.3 PHITS simulation for production yield and purity estimations

PHITS simulations were performed using a similar experimental system illustrated by Fig. 3.8 to determine the production amount, radioactivity purity, and isotope purity of ^{47}Sc from ^{47}Ti target. Fig. 3.11 shows a schematic diagram of the target irradiation with incident neutron yields–DDTTNYs applied in the simulation. The experimental data of the DDTTNYs of the $\text{C}(d,n)$ reaction at incident energies of 12, 20, and 30 MeV deuterons and for neutron emission angle up to 45° are precisely explained in Chapter 2.

Neutrons are irradiated the target, ^{47}Ti (2.54 cm in diameter and 1.8 mm thick) placed 5 mm away from the neutron source. Target dimension was chosen according to the irradiation setup used by Mannhart *et al.* [112]. PHITS simulation was performed at each incident deuteron energy keeping the same target geometry.

For 1 μA of beam current and 5 hours of irradiation, a yield of ^{47}Sc is shown in Table 3.1.

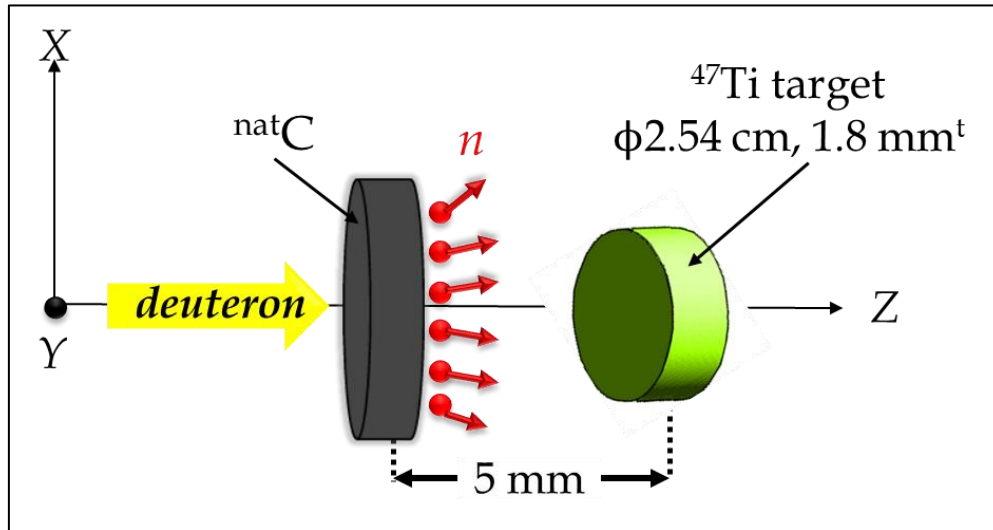


Fig. 3.11: Schematic diagram of the ^{47}Ti target irradiation system used in the simulation.

Table 3.1: Simulation results of ^{47}Sc production yield from 5 g of ^{47}Ti target.

Neutron Source	Yield (1/source)	Yield (MBq/g/ μC)
Experimental DDTNYS at E_d = 12 MeV	7.55×10^{-3}	2.80×10^{-6}
Experimental DDTNYS at E_d = 20 MeV	1.22×10^{-2}	1.36×10^{-5}
Experimental DDTNYS at E_d = 30 MeV	1.65×10^{-2}	4.59×10^{-5}

Table 3.1 shows that as the incident deuteron energy increases, the production of ^{47}Sc increases. Also, to put this method into clinical use, it is necessary to evaluate the production amounts of radioactive and stable isotopes of scandium. A study by Kolsky *et al.* [115] showed that up to 97% of ^{47}Sc could be recovered by using Dowex AG 50W0-X4 cation-exchange method within 10-12 hours of processing and almost 100% of nuclides other than Sc could be separated in the purification and separation. But by-products (whatever in a small amount of percentage) could cause to reduce the labeling rate of the radiopharmaceuticals. If a radioactive impurity of ^{46}Sc contained in a large amount in the labeled radiopharmaceuticals, the radioactive purity of ^{47}Sc will be low, and the patient will be exposed to the extra radiation. On the other hand, if stable isotope ^{45}Sc contained in large amounts, it is not only decreasing the labeling rate of ^{47}Sc but also difficult to know the drug accumulation rate or metabolism of the target cells/tumors.

Therefore, in this simulation, the radioactive and isotopic purity occupied by ^{47}Sc were obtained for each incident deuteron energy. The results are shown in Tables 3.2 and 3.3.

Table 3.2: Production amount of $^{46,47}\text{Sc}$ and ^{47}Sc radioactive purity at each incident deuteron energy.

Neutron Source	Yield (MBq/g)		Radioactive Purity of ^{47}Sc (%)
	^{46}Sc	^{47}Sc	
Experimental DDTTNYs at $E_d = 12 \text{ MeV}$	2.12×10^{-7}	5.03×10^{-2}	99.99
Experimental DDTTNYs at $E_d = 20 \text{ MeV}$	8.63×10^{-4}	2.46×10^{-1}	99.65
Experimental DDTTNYs at $E_d = 30 \text{ MeV}$	1.96×10^{-2}	8.26×10^{-1}	97.69

Table 3.3: Production amount of $^{45,46,47}\text{Sc}$ isotopes and isotopic purity of ^{47}Sc at each incident deuteron energy. ‘-’ means ^{45}Sc cannot produce at 12 MeV incident deuteron energy.

Neutron Source	No. of atom (-)			Isotopic Purity of ^{47}Sc (%)
	^{45}Sc	^{46}Sc	^{47}Sc	
Experimental DDTTNYs at $E_d = 12 \text{ MeV}$	—	1.11×10^7	1.42×10^{11}	99.99
Experimental DDTTNYs at $E_d = 20 \text{ MeV}$	2.58×10^7	4.51×10^{10}	6.94×10^{11}	93.90
Experimental DDTTNYs at $E_d = 30 \text{ MeV}$	3.30×10^{10}	1.02×10^{12}	2.34×10^{12}	68.88

From Table 3.2, it was found that the radioactivity purity of ^{47}Sc showed a high value at any incident deuteron energy. However, as the incident deuteron energy increases, ^{47}Sc production increases and its radioactive purity decreases. Since the half-life of ^{46}Sc is about 83.79 d, which is almost 25 times longer than ^{47}Sc , attention must be paid to the radioactive purity over time. On the other hand, Table 3.3 shows that the isotope purity of ^{47}Sc decreases as the incident deuteron energy increases. This is because ^{45}Sc and ^{46}Sc were produced in large quantities as the energy of the neutrons emitted by the $\text{C}(d,n)$ reaction increased. However, the values are enough for SPECT studies. For example, $^{99\text{m}}\text{Tc}$ ($T_{1/2} = 6 \text{ h}$) currently uses for SPECT applications requires an isotopic purity of about 50% at the time of administration to patients and from that point of view, the produced ^{47}Sc by this research is suitable for actual SPECT application.

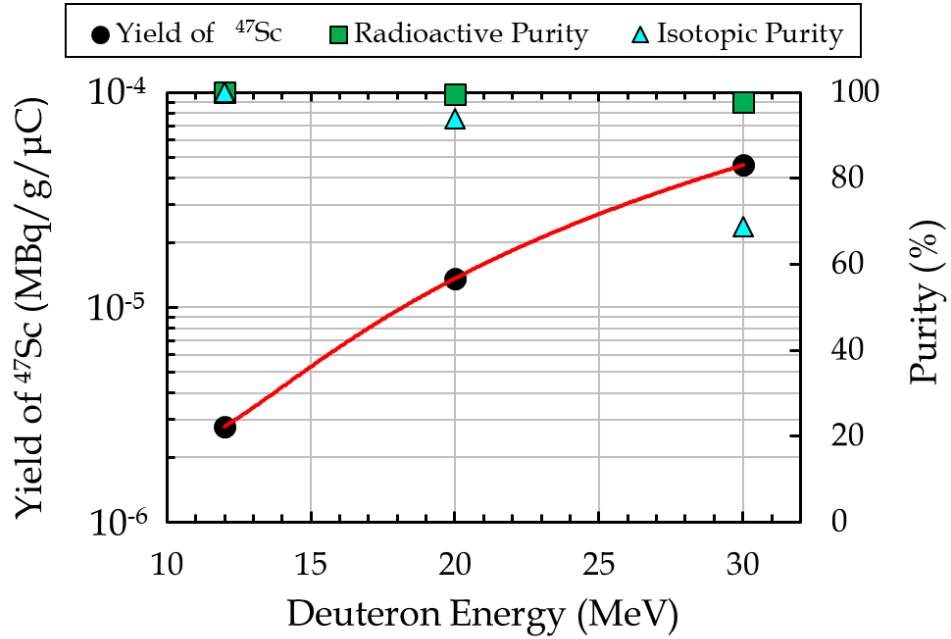


Fig. 3.12: Dependence of ^{47}Sc production, radioactive purity, and isotope purity on incident deuteron energy.

B. 3.4 Summary

Figure 3.12 summarizes the dependence of ^{47}Sc production amount, radioactivity purity, and isotope purity shown in Tables 3.1 to 3.3 on incident deuteron energy. Radioactivity purity and isotope purity are determined assuming that 100% of nuclides other than Sc can be purified and separated. The radioactive and isotopic purity is decreasing while incident deuteron energy is increasing. It is because of more impurity was added in ^{47}Sc production. However, enough production amount can have achieved via the accelerator-based neutron method.

Recently, the use of ^{47}Sc has attracted considerable attention for therapeutic purposes, as part of the $^{43}\text{Sc}/^{47}\text{Sc}$ or $^{44}\text{Sc}/^{47}\text{Sc}$ theranostic radionuclide pair. This research estimated the production amount and purities of ^{47}Sc via $^{47}\text{Ti}(n,p)$ route. Feasibility studies have been performed to determine the suitability of the $\text{C}(d,n)$ accelerator-based neutrons at 12, 20, and 30 MeV of incident deuteron energy. It is found that ^{47}Sc of sufficient purity can be produced in the mentioned procedure. Based on the results obtained from this proof-of-concept study, ^{47}Sc has the potential to be produced in an exceedingly suitable quality for clinical applications,

however, the quality of radioactivity still has to be expanded to fulfill the requirements for radionuclide therapy.

Finally, it must be critically acknowledged, however, that the production of ^{47}Sc is expensive and, hence, the RI is not currently available in large quantities that would enable clinical translation. This research is going to be feasible as soon because the production of the Sc RI family has been fully established to make them readily available in large quantities, at high quality, and a reasonable cost.

3.2 Conclusion

The accelerator-based neutron method is promising for RI production. ^{132}Cs -an alternative tracer of ^{137}Cs , and theranostic nuclide ^{47}Sc can be produced by using accelerator neutrons by deuterons. The production amount and purities are optimum for their appropriate application. Note that, Patwary *et al.* studied the feasibility of ^{132}Cs production using accelerator-based neutrons method and duly described that it can be used as an alternative tracer of ^{137}Cs for environmental radioactivity monitoring [93], as became an important issue after the accident at the nuclear power plant (NPP) in Fukushima Prefecture, Japan in March 2011. However, the RI production method of accelerator-based neutron by deuteron can be extended to propose new production routes or new RIs which can fulfill the demand for respective purposes.

4. Radiation Dose to Patient

In nuclear medicine, radioimmunotherapy (RIT) involves the administration of a RI-labeled monoclonal antibody (mAb), using intravenous or intratumoral injection [116], to treat cancer [117,118]. With RIT, radionuclides are carried directly toward the tumor and emit radiation-induced double-strand DNA breaks, finally inducing cell death [119,120]. Various RIs are used for RIT. For instance, bulky tumors may be treated with radionuclides that emit long-ranged β -rays, like ^{131}I or ^{90}Y , whereas small clusters of cells or tumors can be effectively targeted by α -particles [121] or short-range β -rays [118]. A schematic of the RIT is shown in Fig. 4.1.

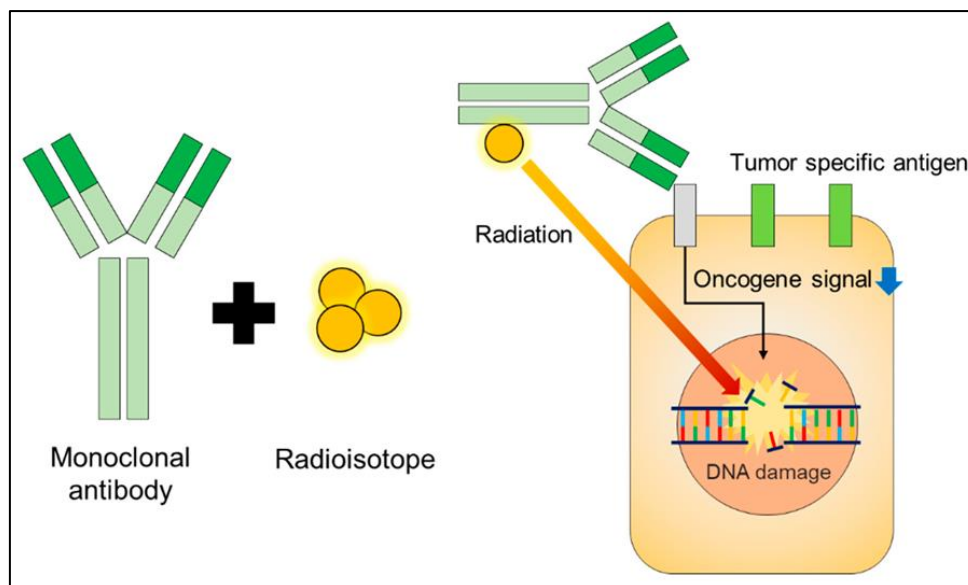


Fig. 4.1: Schematic of RIT. RIT delivers radiation directly to the tumor-specific antigen of a specific cancer type. (Excerpted from ref. [122].)

In RIT, radionuclides are administered to patients in nuclear medicine procedures in an exceedingly kind of diagnostic and therapeutic applications. A key consideration in such studies is the absorbed dose of various organs and tissues of the patient. This concern is of course heightened in therapy applications, where a significant absorbed dose also be received by other organs and by radiosensitive organs. RIT supported patient-specific dosimetry offers the potential for optimizing the dose delivered to the target tumor through utilizing measured radiopharmaceuticals kinetics specific to the individual. The administered activity can adapt for the patient for the best possible radiation dose can deliver to the tumor

while limiting the dose to critical organs/tissues below any permitted threshold for negative biological effects.

In radiological protection, it's important to be able to perform calculations of the absorbed dose in organs and tissues of the body for persons exposed to external radiation sources and radiation from internally distributed radionuclides. Nowadays, nuclear medicine is an integral part of modern healthcare. A theranostic approach is an established tool for specific molecular targeting, both for diagnostics and therapy in nuclear medicine. With the rapid development of radiopharmaceuticals and diagnostic techniques, the utilization of theranostic agents has been continually increasing [123,124]. Internal radiation dosimetry of patients undergoing theranostic is prime for the protection of patients and as in radiological protection. It is important to be able to perform valid calculations of the absorbed dose in organs and tissues of the body for patients exposed to radiation from internally distributed radionuclides. Calculation of the radiation amount absorbed by body tissue is critical for the success of the treatments [125]. It prefers to estimate the dose to be administered to the patient to provide maximum therapeutic effect but at the identical cut-off data excessive irradiation of healthy tissues [126]. Estimating doses to individual organs and tissues in an exceedingly real clinical setting is extremely difficult. So computational frameworks are needed.

Computational simulation with a Monte Carlo method is helpful to clarify the contributions of the particle types and their energy distributions to organ doses inside a human body, which is impossible to work out by experimental investigations. For reliable simulation, it is essential to use a humanlike phantom reflecting precise information about both the form of the body and anatomical structure including the interior organs, and a particle transport code which will treat interaction, transport, and energy deposition of not only primary but also secondary particles in wide energy ranges. It is sure, the procedures of the newest calculations, using references of the new biokinetic data from ICRP Publication 107 [127], Human Alimentary Tract (HAT) model from ICRP Publication 100 [128], organ Specific Absorbed Fraction (SAF) values from ICRP Publication 133 [129]. So that absorbed dose calculations are often done to all or any region defined in ICRP Publication 133. Therefore, the effective dose with new tissue weighting factors published within the ICRP Publication 103 [46]. Now a day, the ICRP recommended standardized anthropomorphic computational phantoms [44] are usually used in various computational frameworks [130-135] for internal dose assessment. The phantoms are predicting the organ masses consistent with the ICRP Publication 89 [43]. Since an updated set of reference values for basic anatomical and physiological data was given in ICRP Publication 89 for both male and female subjects of six different ages (newborn, 1, 5, 10, and 15 years, and adult) supported statistics for Western Europeans and North Americans and are different from Asian reference personals. In some cases of internal dosimetry, more realistic phantoms are required to calculate absorbed dose coefficients to patients within the region-specific. Therefore, the introduction of more realistic anatomical models creates the

likelihood of more accurate and representative absorbed dose estimations, especially, for the Asian people.

JAEA has developed the high-resolution voxel phantoms, named the Japanese Male (JM-103) and Japanese female (JF-103), supported CT imaging of actual person to clarify the results of anatomical characteristics of Japanese on dose assessments. These were constructed with body sizes and organ masses that are near the Japanese averages [47], and also the tissue segmentation of the phantoms was based on the ICRP 2007 recommendations [46]. The phantoms are executable to the PHITS [32], which is a general-purpose Monte Carlo code, also developed by the JAEA and collaborating institutes. The code was benchmarked against various experiments including calculations for the radiation dose from internal exposures. As the first Asian voxel phantoms and also the PHITS-based calculation of the organ doses should provide a sensible demonstration of dose calculations for Asian people. However, no attempt has been made to-date to estimate the internal radiation dosimetry in nuclear medicine using the JM-103 and JF-103 voxel phantoms for the medical dosimetry guideline for Asian people.

Therefore, during this chapter, the estimation of the absorbed doses to organs/tissues and also the effective dose to estimate the radiation risk from theranostic application in nuclear medicine is presented to justify the utilization of specific investigation. The PHITS-based estimation uses the JM-103 and JF-103 voxel phantoms to demonstrate the dose calculations in accordance with the ICRP Publication 103 for the Asiatic reference patients.

4.1 Dose quantities in radiological protection

The protection of human health from exposure due to the utilization of ionizing radiation is that the purpose of radiation protection, which relies on some principles derived from the knowledge of risk [46]. The system of radiation protection is developed by the ICRP as recommendations that are adapted in national regulations. The definition of dose quantities to be used in radiation protection was defined by the ICRP and therefore the ICRU. Three quantities are of relevance for radiation protection purposes: basic physical quantities, protection quantities, and operational quantities. The physical quantities are universally accepted for the characterization of radiation fields. These are defined at any point within the field, and therefore the units are directly obtained by primary standards. The protection quantities configure the idea for dose limitation. These quantities are not directly measurable but can be estimated with a group of measurable operational quantities that are recommended in routine monitoring of occupational exposure. The relation between these different kinds of quantities is shown in Fig. 4.2. In both the retrospective assessment of risk from exposure to radiation, supported on the scientific knowledge base, and within the prospective management of such risk by the system of radiation protection, the (absorbed, equivalent or effective) dose appears as a central quantity to be evaluated. While a dose from external irradiation

could also be measured with properly calibrated dosimeters, the absorbed dose due to incorporated radionuclides during the commitment of the period following the intake is not measurable in the least. Instead, in internal dosimetry, the activity of the incorporated radionuclides is measured and interpreted into dose using models.

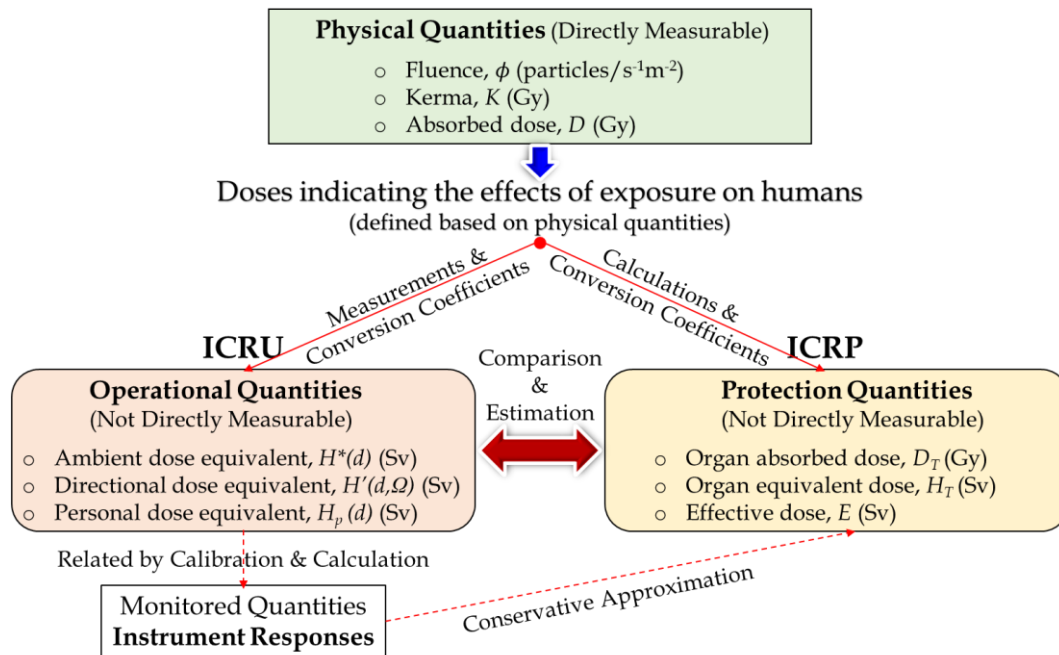


Fig. 4.2: Radiation dose quantities define by the ICRP and the ICRU.

To control radiation effects on the human body, it is necessary to contemplate the consequences of exposure on multiple parts of the body. Thus, protection quantities are calculated based on doses for organs/tissues within the human body. Also, operational dose quantities are defined to be used in measurements of external radiation exposure and practical applications.

4.2 Internal dose calculations

Internal dosimetry is motivated by the idea that the absorbed dose in an organ/tissue could be a good predictor for biological effect on them with a minimum dose level and dose rate. As an example, sound data are indicating that DNA damage responses and mutational processes operate at low doses (down to 20 mGy) and dose rates (down to 1 mGy day⁻¹, equivalent to approximately 0.04 mGy h⁻¹) as they are doing at higher doses and dose rates [136,137].

The absorbed dose, D to an organ from an internally administered radiopharmaceutical depends on the characteristics of both the radionuclide and therefore the pharmaceutical in terms of the sort of radiation emitted and the spatial and temporal distribution of the radionuclide within the body. ICRU defined D in a point as [138]:

$$D = \frac{d\bar{\epsilon}}{dm} \quad (4-1)$$

where $d\bar{\epsilon}$ is the mean energy imparted to the matter of mass dm by ionizing radiation. The SI unit is J kg^{-1} and is most often referred to as gray (Gy). In theory, the mean energy imparted is deposited over an infinitesimal volume, but in practice, the mean energy imparted is calculated over a finite volume. This volume is named the target region (or tissue), r_T , [139] leading to a calculation of the mean absorbed dose, \bar{D} . The foremost common method to calculate absorbed dose from an internally deposited radionuclide is to use the framework provided by the MIRD Committee of the Society of Nuclear Medicine in the USA. The latest revision of the MIRD formalism given in MIRD pamphlet 21 [139] states that the mean absorbed dose for a time-independent system is calculated as:

$$D(r_T, T_D) = \sum_{r_S} \tilde{A}(r_S, T_D) S(r_T \leftarrow r_S) \quad (4-2)$$

where $D(r_T, T_D)$ is the mean absorbed dose in the target region r_T over the dose-integration period T_D , $\tilde{A}(r_S, T_D)$ is the time-integrated activity (or, cumulated activity) in the source region r_S over the dose-integration period T_D . $S(r_T \leftarrow r_S)$ is the absorbed dose in r_T per disintegration in r_S and defined as:

$$S(r_T \leftarrow r_S) = \sum_i \Delta_i \phi(r_T \leftarrow r_S, E_i) \quad (4-3)$$

where $\phi(r_T \leftarrow r_S, E_i)$ is the SAF value [129] (i.e., the fraction of the E_i emitted in source region r_S to the target region r_T divided by the mass of the target tissue in kilograms) of the i^{th} emitted radiation of the radionuclide and $\Delta_i = E_i Y_i$ (the product of the yield Y_i , and the mean energy or part of the energy distribution for β decay E_i [127]) of the i^{th} nuclear transition of the radionuclide in joules. For beta spectra we can calculate radionuclide-specific $S_{\text{beta}}(r_T \leftarrow r_S)$ values. The $S_{\text{beta}}(r_T \leftarrow r_S)$ values are generated by integration over the beta particle energy distribution. Thus, the S value considers all physical factors when calculating the energy absorbed by the target organ, from radiation emitted from the source organ.

The MIRD formalism is often used for both diagnostic and therapeutic nuclear medicine and be applied to whole organs, tissue subregions, voxelized structures, and individual cellular compartments. For radiation protection purposes, human models are relevant in absorbed dose calculations because the aim is to estimate the risk of late stochastic effects on an outside population of patients. The utilization of dosimetry factors based on a standardized phantom and average-based biokinetics. The discrepancy between the body geometry of the patient which of the dosimetry model introduces inaccuracies into the absorbed dose calculation [140].

When administering high activities for therapeutic purposes the aim is to provide enough deterministic effects on tumor cells but to avoid such effects on normal tissues. Therefore, the planning of radionuclide therapy is extremely important to make sure that the right activity is administered to achieve the specified effect. The calculation of organ absorbed doses in patient-specific radionuclide therapy dose planning [141-144] must be as accurate as possible. In patient-specific dosimetry, both a patient-specific physical model furthermore as patient-specific biokinetic data should be included. If the inhomogeneous activity distribution within an organ or tissue even is accounted for, the accuracy within the absorbed dose calculation would increase.

4.2.1 Anatomical models

Many different phantoms are accustomed to simulating absorbed fractions between source and target regions [145]. These mathematical models are divided into three different generations phantoms:

1. Stylized: The first-generation phantoms are stylized mathematical models described by linear and quadratic equations. The foremost commonly used phantom for the estimation of absorbed doses to numerous organs and tissues is the adult phantom by Snyder *et al.* (1975) [146]. This was later improved and completed with a phantom for other ages by Cristy and Eckerman (1987) [147]. These phantoms are utilized in the ICRP publications and biokinetic dosimetry programs [134]. The mathematical models are very schematic. For the family phantoms by Cristy and Eckerman, the source regions are defined based on the Reference Man defined in ICRP Publication 23 [148], which is described as a Caucasian Western European or North American person. The ICRP stresses that the Reference Man does not represent a random sample of any specified population [148].
2. Voxel: The second-generation phantoms are the voxel-based mathematical models derived from high-resolution CT images or MR imaging of real humans. The human images are voxelized and every voxel is segmented and given an object identifier number (OID), where every OID represents a

source region. There are many voxelized phantoms created for various purposes, but they are all derived from the images of one person [145].

3. Non-uniform rational B-spline: The third-generation phantoms are the non-uniform rational B-spline phantoms which are supported mathematical models that use a group of control points to define surfaces. This provides the chance to change or introduce anatomical differences in size or describe other characteristics as, as an example, a mathematical model generated to simulate respiratory motion [149].

In each new generation, structures and features are increasingly realistic and detailed to be used in Monte Carlo simulations to come up with more accurate absorbed fractions. Monte Carlo simulations are performed on the mathematical models and therefore the absorbed doses are hence calculated for target regions defined by the phantoms.

4.2.1.1 Monte Carlo simulation on anatomical model

The Monte Carlo method is that the main tool went to calculate dose conversion factors. Based on a consistent geometry, the transport of energy by photons and electrons is simulated and source-to-target dose factors are calculated by an accurate coupled electron/photon program.

When using Monte Carlo programs in medical applications the accuracy within the simulated phantom can be critical. The interior shapes of organs in an exceedingly human are very complicated, and therefore the assumption of equivalent cylinders is not always justified. The realistic anthropomorphic phantoms recently developed are therefore of great importance. These phantoms are often represented as voxel matrices where the worth of every voxel represents an activity (or density) and its position in the 3D matrix represents its location (x,y,z) in the coordinate system. By linking a voxel value to a particular material one can simulate non-homogeneous attenuation. The phantom matrix also can be obtained from a CT study of a particular patient, resulting in very accurate simulation for a particular case.

Several voxel-based phantoms are developed for general purposes [150-153]. One amongst the most recent voxel phantoms introduced by the ICRP/ICRU was reported in many cases. The adult male and adult female ICRP/ICRU computational voxel phantoms were approved by ICRP in 2007 and adopted by ICRU in 2008 as reference phantoms for dosimetric calculations [44]. These mathematical models were constructed by adjusting the voxel phantoms of Golem [45] and Laura [154] to the organ masses given within the ICRP Publication 89 [43]. The phantoms are published in ICRP Publication 110 [44]. However, for accurate dosimetry more specific reference phantom is required.

4.2.1.2 Dosimetry models related to the anatomical model

Dosimetry models represent the transport of radiations recorded within the nuclear database [127] from their point of emission, following the nuclear transformation of a radionuclide, to the radiosensitive regions of the body combined with biokinetic models they can predict the doses absorbed by the tissues and therefore the committed effective dose following the intake of a radionuclide. The geometry of irradiation is provided by computational anthropomorphic phantoms according to the volumes and densities of organs in an exceedingly reference person [43]. Where the precise nature and site of the cells in danger are identified (skeleton, gut, lung), specific models are available to assess doses at the cellular scale. The laws of physics are applied through Monte Carlo codes. A recent improvement was the endorsement by the ICRP of voxel phantoms [44] rather than the formerly stylized phantoms where organs were represented by simple geometric shapes like ellipsoids and cylinder [147]. The male and female voxel phantoms are based on medical images from real persons and include two matrices of volume elements (voxels). They provide a more precise and realistic representation of human anatomy.

The ICRP dose calculation task group, DOCAI, took advantage of those phantoms to recalculate the specific absorbed fractions (SAF) of energy deposited in target regions following the emission of radiation in source regions and published in [129].

4.2.2 Japanese reference adult phantoms

To calculate organ doses of the survivors of the atomic bomb in Hiroshima and Nagasaki, the Dosimetric System 1986 (DS86) was used. In DS86, mathematical-type phantoms, with the body sizes and organ masses adjusted to Japanese averages, were used for organ dose calculations [155]. These mathematical phantoms were constructed by modifying the Medical Internal Radiation Dose (MIRD) Committee phantoms [147].

In the late 1990s, the Japan Atomic Energy Agency (JAEA) had started the development of Japanese voxel phantoms to clarify the results of anatomical characteristics of Japanese on dose assessments. Saito *et al.* had developed the Otoko and Onago phantoms as the first Japanese voxel phantoms [156,157]. The voxel size of those phantoms is $0.98 \times 0.98 \times 10 \text{ mm}^3$. In some cases of internal dosimetry, more realistic phantoms were required to calculate the SAFs. Therefore, the authors developed the Japanese male (JM) and Japanese female (JF) phantoms whose voxel size is $0.98 \times 0.98 \times 1.0 \text{ mm}^3$ [158,159]. Since the JM and JF phantoms were constructed by using the CT images of a particular subject, masses of organs and tissues in JM and JF failed to represent the Japanese averages [48].

The above Japanese voxel phantoms have supported the recommendations [160] issued in 1991 as Publication 60 by the ICRP. In March 2007, ICRP approved

the new recommendations (ICRP Publication 103) [46]. Recently, the reference adult male and female voxel phantoms were constructed into consideration of the tissue-weighting factors given in ICRP Publication 103 [46].

From these backgrounds, the authors modified the JM and JF phantoms to construct the adult JM and JF voxel phantoms with body sizes and organ masses that are near the Japanese averages. Also, the tissue segmentations of the new Japanese adult male and female phantoms were based on ICRP Publication 103. Then, these phantoms are called as JM-103 and JF-103 phantoms, respectively. These phantoms are useful to general-purpose radiation transport code-PHITS. Table 4.1 shows the physical characteristics of JM-103 and JF-103 voxel phantoms.

Table 4.1: A comparative scenario between the main physical characteristics of JM-103 & JF-103 developed at JAEA [47] and the adult male (AM) & adult female (AF) reference computational phantoms developed by the ICRP/ICRU [44].

Property	JM-103	JF-103	ICRP-AM	ICRP-AF
Height (cm)	171	155	176	163
Weight (kg)	65	52	73	60
Voxel size (mm ³)	0.98 × 0.98 × 1.0		36.54	15.25
Slice thickness (mm)	1.0		8.0	4.84
Tissue segmentation	ICRP Publication 103 [46]			
Number of horizontal pixels	512	526	127	137
Number of vertical pixels	1835	1666	254	299
Japanese average [48]	Male: 170 cm, 64 kg Female: 155 cm, 52 kg			

CT phantoms of JM-103 and JF-103 with an average body size were developed as the first Asian voxel phantoms. Voxel size is an important component of a specific organ or region image quality in CT imaging. It is related to both the pixel size and slice thickness. Where pixel size is dependent on both the field of view and the image matrix. [161] From Table 4.1, Japanese voxel phantoms have very specific voxel size and slice thickness than the ICRP adult phantoms. Besides, the matrix size in the horizontal alignment (512 × 526) and the vertical alignment (1835 × 1666) is more detailed so that smaller pixel size is expected (e.g., typically, when the field of view is 320 mm, the theoretical size of 1 pixel in an image matrix is 0.625 mm for 512 × 512; 0.313 mm for 1024 × 1024; and 0.156 mm for 2048 × 2048 [162]). It is well-known that the smaller the pixel size, the greater the image spatial resolution which is meaning that an accurate shape and size can be obtained from the CT imaging. Therefore, due to the smaller pixel size and thinner slice

thickness of the JM-103 and JF-103 voxel phantom than the ICRP adult voxel phantoms, the internal body parts (organs, tissues, and bones) of the Japanese volunteers are defining specific geometrics. As much as the anatomical properties are specific, as much as possible to calculate the absorbed dose precisely. This research is demonstrating the necessity of sophisticated phantoms for accurate dose calculations.

4.2.3 PHITS simulation for dose estimation

4.2.3.1 *The Basics of the Monte Carlo Method-PHITS*

The Monte Carlo method is employed to numerically solve problems that involve stochastic processes. The strategy has been continuously developed and has become increasingly important and useful as computing power has improved. Monte Carlo simulations make it possible to calculate parameters that cannot be measured in an experimental or a clinical situation. The PHITS-method has been used extensively throughout this research and more detailed information about the method will be found in ref. [32].

4.2.3.2 *Incorporation of JM-103 and JF-103 voxel phantoms to PHITS*

The voxel phantoms designated as JM-103 and JF-103 simulating a male and female, respectively, were developed from CT images of healthy adult Japanese volunteers. Also, the skeleton system was segmented into 7 subgroups keep with the density of the bones determined by the CT values, and also the elementary compositions of every subgroup were assigned based on the weight percentage of bone marrow. The computational geometry formats which could be read in PHITS are both general and combinational geometry. To require advantage of the repeating structure of a lattice function in general geometry, we converted the phantoms into the format of general geometry. The voxel data were saved as external ASCII files, whose sizes were 710 and 620 MB for the JM-103 and JF-103 respectively, and which were loaded within the execution of the PHITS simulation. Figure 4.3 shows 3D anterior views of the JM-103 and JF-103 phantoms depicted using the PHITS. The skin, muscle, and adipose tissues were made transparent to exhibit the interior structure.

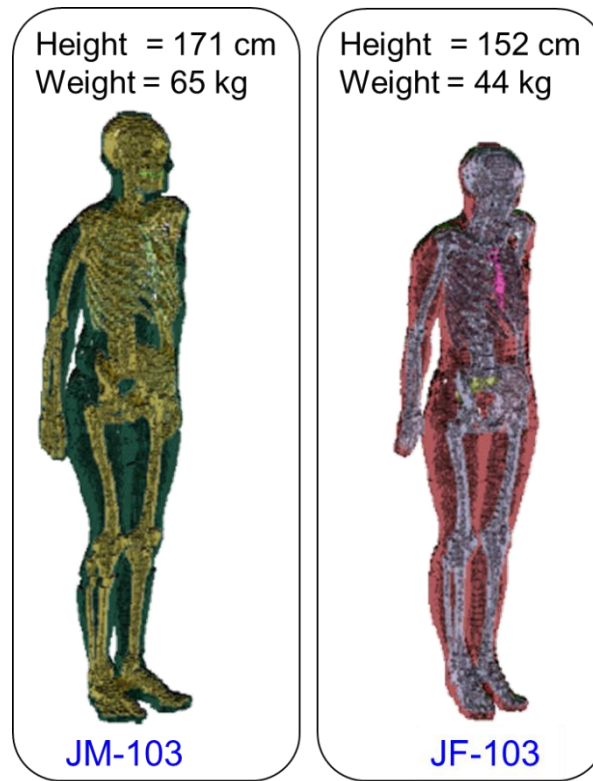


Fig. 4.3: 3D anterior view of the whole body of the JM-103 and JF-103.

4.2.3.3 PHITS conditions in dose calculation

In PHITS simulation, the distributions of beta particles and also the secondary particles produced within the human body are tracked until their kinetic energies fall below the cutoff energies, or the particles escape outside the computational geometry. The cutoff energy was set at 1.0×10^{-3} MeV for photons, electrons, and other charged particles. For the nuclear decay data “RIsource.dat” file was active by parameterized the decay file directory. Which has the nuclear decay database of radionuclides and is employed to get the energy distribution of radionuclides sources in accordance with the ICRP Publication 107 [127]. Since the β^+ and/or β^- decays are generated by simply specifying the activity (in Bq) within the simulation. The energy spectrum is set supported the decays of the radionuclide including the contributions from their daughter nuclides at the time to attend radioactive equilibrium. However, there is no information on the time necessary to achieve radioactive equilibrium is present, a command was set as for that. The use

of nuclear decay database and energy distribution of radionuclide sources makes the transport calculation more accurate. The absorbed doses in organs and tissues were calculated with the JM-103 and JF-103 phantoms for conditions defined by the nuclear medicine administrations. The estimated relative error within the PHITS dose calculations, defined as an estimated standard deviation of the mean divided by the estimated mean, was reduced to below 0.05.

4.2.4 Absorbed doses to organs and tissues

The mean absorbed dose as defined in Eq. (4-2) is calculated by summing the dose contribution from all source regions to a particular target region. The calculation is usually straightforward but maybe extensive in cases of the many separate nuclear transitions with disintegrations in several source regions connected to several target regions. Therefore, the absorbed dose calculations are facilitated if they are automated in a computer program.

An organ dose calculation system, PHITS simulation, is employed for calculation of the organ doses due to internal exposures from the theranostics application in nuclear medicine. The JM-103 and JF-103 phantoms were incorporated into PHITS to estimate the absorbed doses to organs and tissues. Taking an example for organ absorbed doses estimations, we used radionuclide properties of theranostic radionuclide ^{47}Sc . Since this theranostic pharmaceutical has suitable characteristics for diagnostics radiology and yet as therapeutic purposes in targeted RIT. Figure 4.4 shows schematically the procedure for determining the absorbed doses and effective dose i.e., protection quantities as defined in ICRP Publication 103 [46].

Absorbed doses in organs and tissues are assessed separately for males and females using the JM-103 and JF-103 phantoms consisting absorbed doses to all or any 213 regions including 47 target regions defined in ICRP Publication 133 [129], and also the estimated results are presented in terms of absorbed dose per administered activity (mGy/MBq). The calculated absorbed doses per intravenously administered activity are presented in Table 4.2 for ^{47}Sc and with the results calculated with ICRP/ICRU reference computational phantoms ICRP-AM and ICRP-AF.

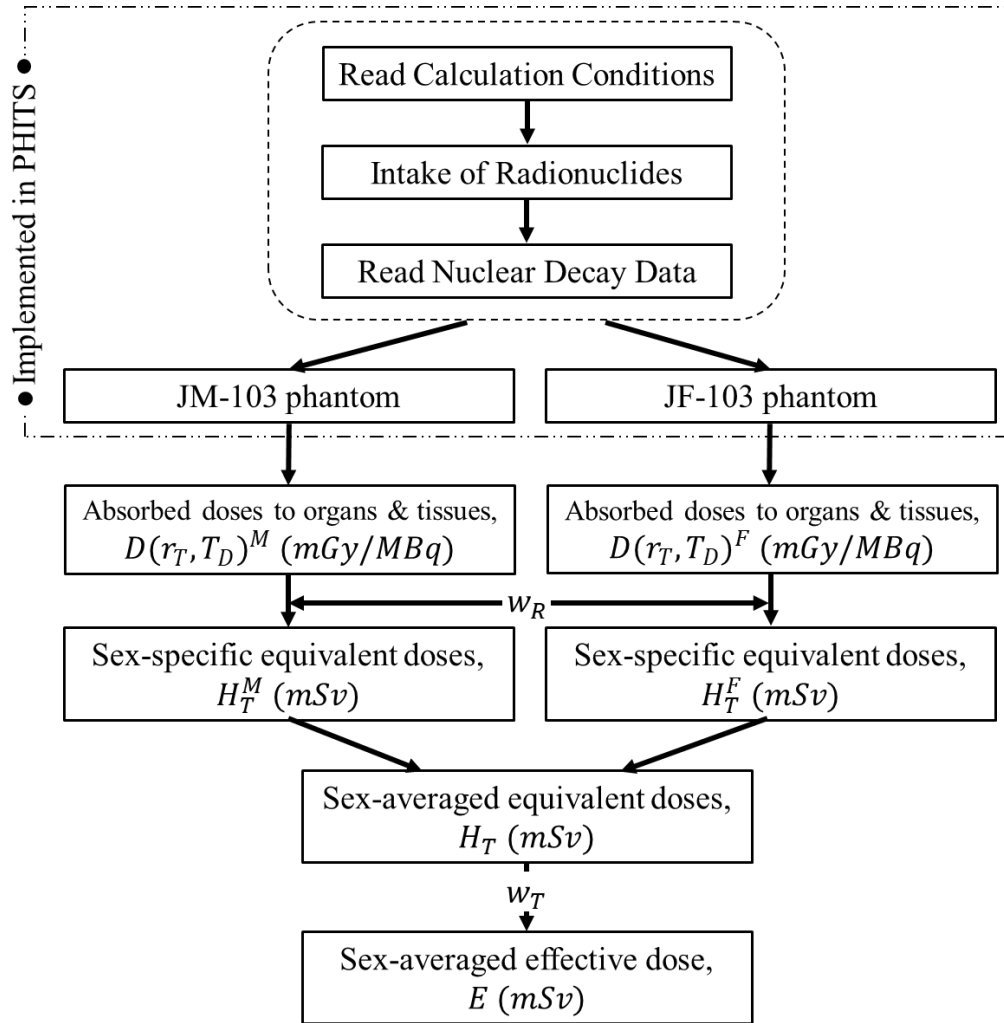


Fig. 4.4: A schematic diagram for the internal radiation dose calculation with PHITS simulation.

Table 4.2: Absorbed doses (mGy/MBq) and the effective dose (mSv/MBq) per administered activity of theranostic radionuclide ^{47}Sc (physical half-life, $T_{1/2} = 3.3492$ d) for the proposed internal dosimetry calculation method with the Japanese phantoms JM-103 and JF-103. Results obtained with ICRP/ICRU computational reference phantoms are also given. ‘–’ and ‘×’ indicating the value of absorbed dose cannot calculate due to sex dependency and in the estimation method, respectively.

Organ	Japanese Phantoms		ICRP/ICRU Phantoms	
	JM-103	JF-103	AM	AF
Adipose tissues	1.13E-01	1.33E-01	8.93E-02	1.05E-01
Adrenals	1.17E-01	1.60E-01	9.18E-02	1.23E-01
Brain	1.40E-01	1.90E-01	1.09E-01	1.45E-01
Breast	9.50E-02	1.18E-01	7.63E-02	9.41E-02
Bronchi	9.95E-02	1.09E-01	7.67E-02	8.41E-02
Cervix	–	×	–	1.25E-01
Esophagus*	1.24E-01	1.53E-01	9.58E-02	1.18E-01
ET region	9.80E-02	1.40E-01	7.38E-02	1.05E-01
Eye	3.98E-03	7.12E-03	×	×
Eye lenses	1.09E-01	1.39E-01	8.52E-02	1.08E-01
Gallbladder Content	8.07E-01	1.74E-01	×	×
Gallbladder wall	1.12E-01	1.54E-01	8.90E-02	1.20E-01
Heart Content	2.23E-01	1.32E-01	×	×
Heart wall	1.12E-01	1.32E-01	8.87E-02	1.04E-01
Left colon wall	9.03E-02	1.23E-01	7.18E-02	9.68E-02
Right colon wall	9.43E-02	1.23E-01	7.48E-02	9.64E-02
Kidneys	1.04E-01	1.32E-01	8.24E-02	1.03E-01
Lung	1.03E-01	1.21E-01	8.04E-02	9.35E-02
Liver	1.02E-01	1.21E-01	8.07E-02	9.51E-02
Lymphatic nodes	1.16E-01	1.39E-01	9.05E-02	1.08E-01
Meninges	1.01E-03	2.28E-03	×	×

(continued on next page)

(continued)

Muscle	1.23E-01	1.52E-01	9.70E-02	1.18E-01
Oral mucosa	1.47E-01	2.13E-01	1.14E-01	1.61E-01
Ovaries	—	×	—	1.28E-01
Pancreas	1.09E-01	1.36E-01	8.61E-02	1.07E-01
Prostate	1.40E-01	—	1.09E-01	—
Salivary glands	1.25E-01	1.76E-01	9.74E-02	1.35E-01
Skin	9.63E-02	1.14E-01	7.67E-02	9.05E-02
Small intestine Content	6.30E-03	3.73E-03	×	×
Small intestine wall	9.63E-02	1.23E-01	7.58E-02	9.58E-02
Spleen	9.58E-02	1.12E-01	7.72E-02	8.78E-02
Stomach Content	1.98E-01	1.17E-01	×	×
Stomach wall	8.44E-02	1.02E-01	6.68E-02	8.06E-02
Testes	2.90E-02	—	8.14E-02	—
Thymus	1.30E-01	1.59E-01	1.01E-01	1.24E-01
Thyroid	1.18E-01	1.45E-01	9.18E-02	1.13E-01
Tongue	1.00E-01	1.20E-01	7.58E-02	8.97E-02
Trachea	1.45E-03	6.17E-03	×	×
Ureters	×	×	1.05E-01	1.40E-01
Urinary Bladder Content	2.44E-03	1.68E-03	×	×
Urinary Bladder Wall	1.45E-01	1.64E-01	1.13E-01	1.27E-01
Effective dose (mSv/MBq)	2.53E-01		1.66E-01	

* a Latin word; Esophagus (American English), Oesophagus (British English) [163]

Table 4.2 shows a higher absorbed dose estimation for an individual organ/tissue of the Japanese references than the ICRP adult references. We got this situation for the same administered dose activity of ^{47}Sc and the consideration of the nuclear data for dosimetry calculation remains the same for all estimations. For both JM-103 and JF-103, the absorbed dose coefficients are higher because of smaller physical geometrics of the Japanese references than the ICRP adults (as shown in Table 4.1). From Eq. (4-1), for the same mean energy deposition, the absorbed dose will be higher in the smaller organ/tissue of target regions because of the less weight than the larger organ/tissue. So that for smaller organ/tissue size, a high amount of radiation energy deposited to the respective target organ/tissue. This obeys the basic radiation dosimetry formalism. Female voxel phantom, JF-103 showed its organs/tissues are more radiation-sensitive compared to the male voxel phantom, JM-103. It is obvious, the female's overall body size and organ sizes are smaller than those of her male counterpart (thus her radiation doses will be higher, given the same amounts of administered activity and similar biokinetics). This result acknowledges the finding of the ICRP Publication 103 that the risk of incidence of cancers of all types and serious health impacts are somewhat higher for the women than for the men, with the overall lethality risk for women being approximately 35% greater than that for men. Therefore, our study for the organs/tissue absorbed dose estimations are recommending the use of specific reference anatomical model in the internal dose calculations in the nuclear medicine department.

In addition, we can term the absorbed dose estimations from voxel pixel quality of the tomographic image based anatomical phantom. Because of the enormous matrix size (horizontal and vertical) and smaller pixel size of JM-103 and JF-103 phantoms, localizations of their organ/tissue/bone is more specific in geometrically than the ICRP reference adults (see Table 4.1). It means the image data acquisition shows better image spatial resolution for the real Japanese volunteer's body parts reconstructions. So that the absorbed dose estimations for the Japanese averages (showed in Table 4.2) are precisely gives the detail dose resolution for the specific organ/tissue. This research is not focusing on the voxel S-value (SVS) study for the absorbed dose evaluation and their impacts. However, the analogy of the pixel size and voxel resolution suggested that the organ/tissue absorbed doses would be more reliable for the JM-103 and JF-103 instead of the ICRP-AM and ICRP-AF for the Japanese and the Asian.

4.3 Biological effects and effective dose calculations

It is well-known that ionizing radiation incorporates a biological effect on the human body. There are two forms of harmful effects: deterministic (tissue) effects and stochastic effects [46]. These effects are caused by both high and low doses. Former one should consider when organ dose exceeds the threshold dose for the respective organ. But the stochastic effect is observed as a statistically detectable

increase of cancer after a certain period after the exposure. This study focuses on the stochastic effect of the ionizing radiation. The results can not apply to estimate any deterministic effects.

To estimate the biological effect from a disintegration there are two correction factors, the radiation weighting factor, w_R , and therefore the tissue weighting factor, w_T , applied on the mean absorbed dose. The radiation weighting factors are defined largely to reflect the relative biological effectiveness of the stochastic effects of various forms of radiation. According to the ICRP Publication 103 [46], $w_R = 1$ is employed for all radiation types in nuclear medicine. The entire detriment for stochastic effects, which is that the overall harm to health experienced by an exposed group and its descendants is defined by the tissue weighting factor. The tissue weighting factors published in ICRP Publication 103 given in Table 4.3 are sex- and age-averaged values and it is stressed that the appliance of those factors is restricted to the effective dose definition and not used for the assessment of individual risk.

Table 4.3: Tissue weighting factors w_T for different organs [46].

Organ	w_T	$\sum w_T$
Bone-marrow (red)	0.12	0.72
Breast		
Colon		
Lung		
Stomach		
Remainder tissues*		
Gonads	0.08	0.08
Bladder	0.04	0.16
Oesophagus		
Liver		
Thyroid		
Bone surface	0.01	0.04
Brain		
Salivary glands		
Skin		
Total		1.00

* Remainder tissues: Adrenals, Extrathoracic (ET) region, Gall bladder, Heart, Kidneys, Lymphatic nodes, Muscle, Oral mucosa, Pancreas, Prostate (♂), Small intestine, Spleen, Thymus, Uterus/cervix (♀).

The effective dose is a radiation protection quantity defined by the ICRP to estimate the overall effect on the human body and its descendants caused by stochastic effects. The quantity was first introduced within the ICRP Publication 26 and up to now ICRP has revised the weighting factors twice and also changed the name of the quantity to effective dose (E) [46,160,164]. The unit is Sievert (Sv).

An effective dose is calculated from the equivalent dose. Absorbed doses in organs and tissues are assessed separately for males and females using the JM-103 and JF-103 phantoms and so equivalent doses for the organs and tissues are calculated by multiplying the radiation weighting factors, w_R . For β and γ radiation the w_R is adequate to 1. The sex-averaged equivalent doses are obtained by averaging male and female values, then weighted by the tissue weighting factors, w_T given in Table 4.3 and summed over all organs and tissues to get the effective dose, E .

To estimate the radiation-induced stochastic effects for a population the sex-average effective dose E is calculated:

$$E = \sum_T w_T \sum_R w_R \left[\frac{D_R(r_T, T_D)^M + D_R(r_T, T_D)^F}{2} \right] \quad (4-4)$$

where w_T is the tissue weighting factor for tissue T and $\sum_R w_R D_R(r_T, T_D)^{sex}$ is the sex-specific equivalent dose for target region r_T .

In this research, the effective dose was estimated for ^{47}Sc , and also the result is presented in terms of effective dose per administered activity (mSv/MBq). Table 4.2 showed the effective dose for ^{47}Sc estimated within the method presented in this research. The sex-averaged whole-body effective dose was calculated as 2.53×10^{-1} mSv/MBq with 0.10% of statistical uncertainty. Besides, the effective dose coefficient for the ICRP adults was calculated 1.66×10^{-1} mSv/MBq. It is found that our result is an increase of about 52.41% than the effective dose calculation result with the ICRP adult phantoms, ICRP-AM, and ICRP-AF. This variation was due to the different anatomical and physiological characteristics of the Japanese and the ICRP references. For smaller body properties of the Japanese references, the higher radiation risk is predicted than the ICRP references. Moreover, both of the calculations are in the range of the dose limit recommended by the ICRP 2007 recommendations of the public dose limit for the world and the Japanese populations. It is also noted that the dissimilarities of the effective dose estimations for different anatomical models have an importance for using the specific anatomical model for radiation risk of cancer prediction. In particular, an appropriate calculation of the risk prediction is required to set a national radiation protection guideline.

Also, the effective dose is calculated for some other radionuclides that are emergent in both diagnostic and therapeutic nuclear medicine, and therefore the results are presented in Table 4.4. Dose calculations were performed using the tactic described in this research, which bases its calculations on the JM-103 and JF-103 voxel phantoms and so tissue weighting factors from ICRP Publication 103. The value of E (mSv/MBq) shown in Table 4.4 includes statistical uncertainty within 0.10%. For organ/tissue doses, there are substantial changes between the current method and also the ICRP calculations with their recommended reference phantoms. Therefore, the sole significant change in effective dose differed to previous estimations of the ICRP published data was a 40% reduction for ^{124}I .

Table 4.4: The effective dose from emergent medical radionuclide used in imaging and/or therapeutic nuclear medicine and the difference in % concerning the effective dose presented in the ICRP publications. ‘×’ indicates that the calculated effective dose cannot compare to ICRP reference value because there is no published data.

Radionuclide	Physical Half-life, $T_{1/2}$ [56]	Effective Dose, E (mSv/MBq)	Difference to ICRP published value (%) [reference]
^{64}Cu	12.701 <i>h</i>	3.88E-02	−1.42 [167]
^{67}Cu	61.83 <i>h</i>	1.48E-01	−7.20 [167]
^{67}Ga	3.2617 <i>d</i>	7.92E-02	−2.08 ^a [168]
^{68}Ga	1.129 <i>h</i>	1.67E-02	−2.33 ^b [168]
^{89}Sr	50.563 <i>d</i>	2.92E+00	2.00 [167]
^{90}Y	2.67 <i>d</i>	1.34E-02	×
$^{123}\text{I}^*$	13.2235 <i>h</i>	2.44E-01	−6.60 [168]
$^{124}\text{I}^*$	4.176 <i>d</i>	1.76E+01	−40.00 [168]
$^{131}\text{I}^{**}$	8.0252 <i>d</i>	2.42E+01	20.00 [167]
^{152}Tb	17.5 <i>h</i>	1.26E-01	×
^{161}Tb	6.89 <i>d</i>	2.71E-01	×
^{166}Ho	1.12 <i>d</i>	2.94E-01	×
^{111}In	2.8047 <i>d</i>	1.23E-01	−4.70 ^c [168]

*Thyroid, high uptake; **Thyroid, uptake 55%; ^acompared with ^{67}Ga -citrate; ^bcompared with ^{68}Ga -labelled ethylenediaminetetraacetic acid (EDTA); ^ccompared with ^{111}In -labelled human immunoglobulin (HIG)

Many radiopharmaceuticals labeled with ^{18}F and $^{99\text{m}}\text{Tc}$ are developed for PET imaging and SPECT studies. 2- ^{18}F -fluoro-2-deoxy-D-glucose (^{18}F -FDG) is one among them, but other radiopharmaceuticals are commercially available or under development. Estimation of the effective doses for frequently used radiopharmaceuticals labeled with ^{18}F and $^{99\text{m}}\text{Tc}$ were calculated using the procedure developed during this research and noted with the values for adult reference published within the ICRP Publication 128 [165]. The results of the calculations are shown in Fig. 4.5 (a) and (b).

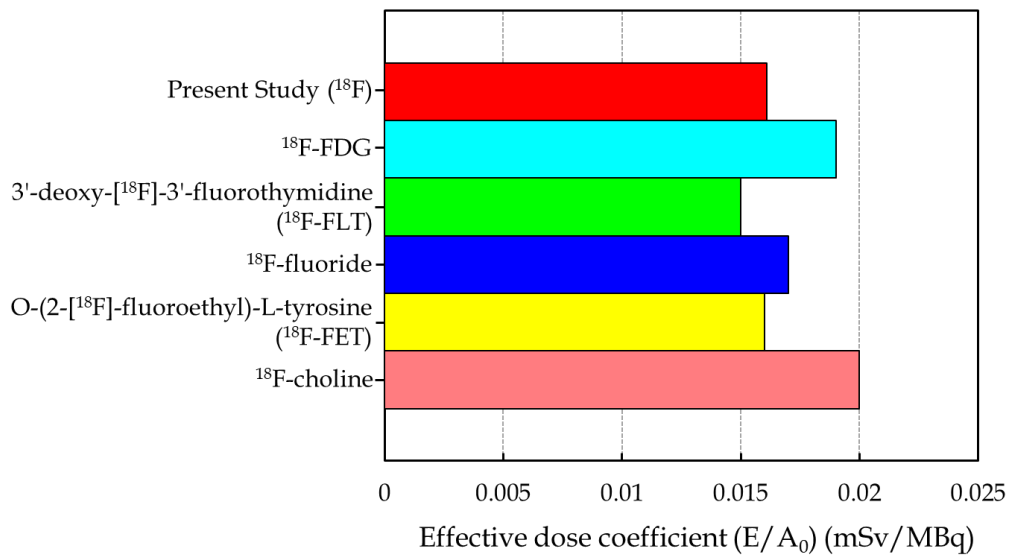
The effective dose coefficient (mSv/MBq) for ^{18}F and $^{99\text{m}}\text{Tc}$ shows the diversified result in this research than the ICRP calculated values for various radiopharmaceuticals. The difference between the corresponding values of E/A_0 , $D(\%)$, is defined as follows:

$$D (\%) = \left(\frac{(\frac{E}{A_0})_{\text{present study}}}{(\frac{E}{A_0})_{\text{ICRP 128}}} - 1 \right) \times 100 \quad (4-5)$$

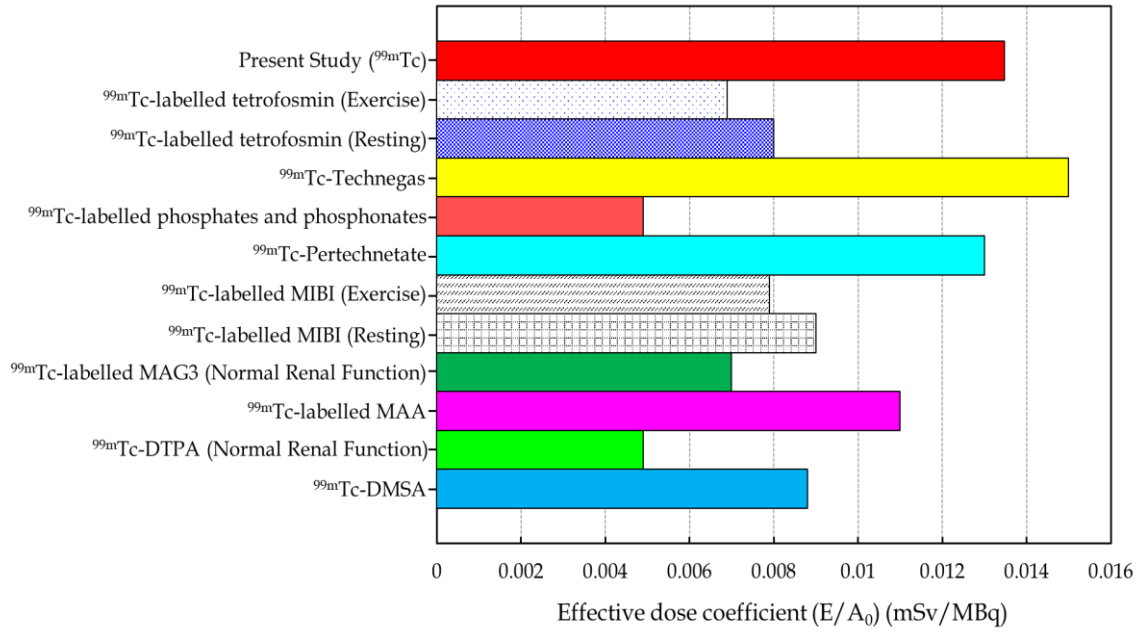
where $(\frac{E}{A_0})_{\text{present study}}$ (mSv/MBq) is the effective dose coefficient calculated using the developed method in the present study, and $(\frac{E}{A_0})_{\text{ICRP 128}}$ (mSv/MBq) is the reference value from the ICRP Publication 128. Fig. 4.5 (a) shows the values of D ranges from -19.5% to 7.33% for ^{18}F -choline (1.70×10^{-2} mSv/MBq) and ^{18}F -FLT (1.50×10^{-2} mSv/MBq), respectively with respect to our value of ^{18}F -PET RI (1.61×10^{-2} mSv/MBq). Whereas, our calculation shows close to the value of E/A_0 for ^{18}F -FET (1.60×10^{-2} mSv/MBq) where our estimation is only 0.62% higher than that of it. On the other hand, almost all forms of radiopharmaceuticals labeled with $^{99\text{m}}\text{Tc}$ showed a lower effective dose coefficient than our calculation for $^{99\text{m}}\text{Tc}$ except $^{99\text{m}}\text{Tc}$ -Technegas (see Fig. 4.5 (b)). But the ICRP 128 value of $^{99\text{m}}\text{Tc}$ -Technegas does not exceed our calculation by more than 10.15%. $^{99\text{m}}\text{Tc}$ -Pertechnetate ($\text{Na}^+ ^{99\text{m}}\text{Tc O}_4^-$) is one of the technetium radiopharmaceuticals used in imaging of thyroid, colon, bladder, and stomach [166]. This radiopharmaceutical shows the nearest whole-body effective dose per administered activity (1.30×10^{-2} mSv/MBq) of our calculation and only 3.67% lower than the value of us (1.35×10^{-2} mSv/MBq). By the way, for both of the RIs, ^{18}F , and $^{99\text{m}}\text{Tc}$, the most common scenario is the disagreement of the calculation done by us and the ICRP reference data published in the ICRP Publication 128. Of course, each calculation system employs different anthropomorphic phantoms, and it is known that the results of dose calculation mainly rely upon the phantom model that defines the shapes, volumes, locations, and orientations of the organs. However, a slight discrepancy is unavoidable because of rounding errors over multiple calculation steps. As a result, the developed computational framework of E/A_0 was considered to be verified. To

validate our results, our estimated result of E/A_0 for ^{18}F and $^{99\text{m}}\text{Tc}$ were compared with the ICRP developed program, Dose and risk CALculation software (DCAL) [167], calculations for intravenous administration of RI by injection with the same criteria of our calculations. The ratio of the quotient of E/A_0 generated using the developed method divided by that obtained using DCAL. The E/A_0 values generated using the developed method were smaller than those obtained using DCAL for both RIs (see Table 4.5). The possible cause of the higher effective dose coefficients generated by the ICRP recommended program, DCAL is the photon specific absorbed fraction library which is based on the data of Cristy and Eckerman (1987, 1993) [147,168] as used by the ICRP. Organ masses for adults are taken from ICRP Publication 23 [42]. This incomparable aspect suggested that appropriate anatomical and physiological references are necessarily important for the internal dosimetry of patients in nuclear medicine applications. Moreover, the validation study also made the importance of the new PHITS based dose estimations using JM-103 and JF-103.

To look more, Fig. 4.5 indicates the dose management in nuclear medicine imaging requires more attention and there is a requirement for the better contribution of new technology for individual patient dose management moreover as for education and training of the multidisciplinary teams of nuclear medicine physicians, technologists, and medical physicists, responsible for the investigations.



(a)



(b)

Fig. 4.5: Effective dose coefficients (mSv/MBq) for clinically relevant and frequently used radiopharmaceuticals with radiolabeled (a) ¹⁸F and (b) ^{99m}Tc.

Table 4.5: Values of E/A₀ generated using developed calculation in the present study and those generated using DCAL [167], and ratios of E/A₀ for intravenous administration of ¹⁸F and ^{99m}Tc RI.

RI	E/A ₀ (mSv/MBq)		
	This study	DCAL	Ratio
¹⁸ F	1.61×10^{-2}	1.70×10^{-2}	0.95
^{99m} Tc	1.35×10^{-2}	1.93×10^{-2}	0.70

4.4 Dose coefficients for intravenous administration of radiopharmaceuticals

The administration of radiopharmaceuticals to humans are increasingly used for diagnosis, therapy, or research purposes. New administration techniques and new radiopharmaceuticals are being introduced continually. Reasonably accurate dosimetry for representative groups of patients for every specific investigation is required to optimize the utilization of the assorted alternative diagnosis and radiopharmaceutical therapy techniques. It is also important to estimate the collective radiation exposure and risk from nuclear medicine investigations. Radiopharmaceuticals for therapy requires even more detailed and patient-specific dosimetry and dose planning for both tumor and normal organs and tissues.

Several reports are published by the ICRP for internal dose coefficient calculations for diagnostic radiopharmaceuticals [165,169,172]. In contrast, only ICRP Publication 140 reported the radiation dosimetry for therapeutic radiopharmaceuticals [173]. Moreover, information regarding dose calculations from radiopharmaceuticals has also been published in reports from the ICRU, notably ICRU Report 67 [174]. Also, many countries set their own absorbed dose catalogs for radiopharmaceuticals [175-178].

An ICRP recommended computer software code-named ‘MIRDose’ and its updated version ‘OLINDA/EXM 2.0’ was developed to facilitate automated and standardized internal dose calculations for nuclear medicine applications [134]. Also, the IDAC-Dose program [135] has been utilized by ICRP to tabulate dose coefficients for patients undergoing examination with radiopharmaceuticals in nuclear medicine mainly intravenous administration. These dosimetry programs were remarked within the dose coefficient calculations published by the ICRP Publication 53, 80, 106, 128, and 140. Since the OLINDA/EXM 2.0 code uses an identical technical basis (phantoms, organ masses, equations, relationship assumed, and other details) as the RADAR system [179]. On the other hand, in an updated version of IDAC-Dose, IDAC-Dose 2.1 uses the most recent ICRP/ICRU reference voxel phantoms, SAF values, and nuclear decay data published by the ICRP.

Since internal dosimetry and calculation of organs/tissues dose coefficients are strongly dependent on the anatomical and physiological data of reference phantoms as it is already described in the past sections of this chapter. In order that this section is presenting the dose coefficients for a few medical RIs that are frequently using as radiopharmaceuticals to humans for diagnosis, therapy, or moreover as theranostic, and research purposes in nuclear medicine applications. The results of dose coefficient calculations done by the method described in this research are compared to the available results published in ICRP publication. The results are given within the following tables.

Table 4.6: Absorbed dose coefficients (mGy/MBq) in different organs/tissues for positron emitter ^{18}F (physical half-life = 1.83 h, [56]). ICRP published values of absorbed dose coefficients (mGy/MBq) for 2- ^{18}F -fluoro-2-deoxy-D-glucose (^{18}F -FDG) from the ICRP Publication 128 [165] have been noted for comparing to the values obtained in this research. ‘—’ means absorbed dose in the respective organs cannot be obtained due to the physiological characteristic of the reference phantom.

Organ	Present Research		ICRP Value
	JM-103	JF-103	Adult
Adrenals	3.97E-02	3.40E-02	1.20E-02
Bone surfaces	3.72E+01	6.53E+00	1.10E-02
Brain	1.87E-01	1.00E-01	3.80E-02
Breast	5.45E-01	5.25E+00	8.80E-03
Esophagus	2.03E-02	1.85E-02	1.20E-02
Gallbladder wall	9.30E-02	3.38E-03	1.30E-02
Heart wall	1.67E-02	5.64E-01	6.70E-02
Colon wall	1.41E-02	7.01E-01	1.30E-02
Kidneys	2.67E-02	7.19E-01	1.70E-02
Lungs	1.58E-01	4.23E-01	2.00E-02
Liver	1.10E+01	4.11E+01	2.10E-02
Muscles	2.57E-01	4.09E-01	1.00E-02
Pancreas	3.33E-02	6.60E-01	1.30E-02
Skin	2.15E-01	2.18E-01	7.80E-03
Small intestine wall	8.46E-01	1.26E-01	1.20E-02
Spleen	7.53E-01	9.25E-01	1.10E-02
Stomach wall	2.36E-02	1.09E-02	1.10E-02
Testes	3.76E-02	—	1.10E-02
Thymus	4.70E-01	5.28E-01	1.20E-02
Thyroid	1.95E-01	1.98E-02	1.00E-02
Urinary Bladder Wall	1.45E-01	1.31E+00	1.30E-01

Table 4.7: Absorbed dose coefficients (mGy/MBq) in different organs/tissues for positron emitter ^{68}Ga (physical half-life = 1.129 h [56]). ^{68}Ga is used mostly for ^{68}Ga -PSMA-PET/CT imaging. ICRP published values of absorbed dose coefficients (mGy/MBq) for ^{68}Ga -labelled ethylenediaminetetraacetic acid (^{68}Ga -EDTA) from the ICRP Publication 128 [165] have been noted for comparing to the values obtained in this research. ‘–’ means absorbed dose in the respective organs cannot be obtained due to the physiological characteristic of the reference phantom.

Organ	Present Research		ICRP Value
	JM-103	JF-103	Adult
Adrenals	9.44E-02	9.51E-02	9.40E-03
Bone surfaces	4.69E-01	4.72E-01	9.20E-03
Brain	1.29E-02	1.30E-02	7.70E-03
Breast	4.78E-01	4.81E-01	7.50E-03
Esophagus	1.67E-02	1.68E-02	8.30E-03
Gallbladder wall	6.89E-02	6.93E-02	9.80E-03
Heart wall	1.21E-02	1.22E-02	8.70E-03
Colon wall	3.66E-01	3.68E-01	1.30E-02
Kidneys	6.43E-01	9.54E-01	5.40E-02
Lungs	4.49E-02	1.17E-02	8.20E-03
Liver	2.57E-01	4.52E-01	8.90E-03
Muscles	3.08E-01	3.11E-01	9.70E-03
Pancreas	6.10E-01	6.15E-01	9.60E-03
Skin	2.25E-01	2.27E-01	7.80E-03
Small intestine wall	4.30E-01	4.33E-01	1.20E-02
Spleen	6.02E-02	6.06E-02	9.20E-03
Stomach wall	1.23E-01	1.24E-01	9.20E-03
Testes	8.23E-02	–	1.20E-02
Thymus	3.33E-01	3.35E-01	8.30E-03
Thyroid	1.30E-01	1.31E-01	8.20E-03
Urinary Bladder Wall	3.35E-01	3.38E-01	5.90E-01

Table 4.8: Absorbed dose coefficients (mGy/MBq) for ^{99m}Tc (physical half-life = 6.0072 h [56]). ICRP published values of absorbed dose coefficients (mGy/MBq) for ^{99m}Tc -labelled methoxy-isobutyl-isonitrile (^{99m}Tc -MIBI- Resting subject and ^{99m}Tc -MIBI- Exercise) from the ICRP Publication 128 [165] have been noted for comparing to the values obtained in this research. ‘–’ means absorbed dose in the respective organs cannot be obtained due to the physiological characteristic of the reference phantom.

Organ			ICRP Value	
			^{99m}Tc -MIBI- Resting subject	^{99m}Tc -MIBI- Exercise
	Present Research		Adult	Adult
	JM-103	JF-103		
Adrenals	6.40E-01	6.33E-01	7.50E-03	6.60E-03
Bone surfaces	1.31E-03	1.29E-03	8.20E-03	7.80E-03
Brain	7.50E-06	7.43E-06	5.20E-03	4.40E-03
Breast	4.73E-04	4.69E-04	3.80E-03	3.40E-03
Esophagus	3.55E-01	3.51E-01	4.10E-03	4.00E-03
Gallbladder wall	7.54E+00	7.46E+00	3.90E-02	3.30E-02
Heart wall	7.89E-02	7.81E-02	6.30E-03	7.20E-03
Colon wall	1.20E-01	2.37E-01	2.40E-02	1.90E-02
Kidneys	8.92E-02	8.83E-02	3.60E-02	2.60E-02
Lungs	6.09E-02	6.02E-02	4.60E-03	4.40E-03
Liver	1.97E-01	1.95E-01	1.10E-02	9.20E-02
Muscles	3.35E-03	3.32E-03	2.90E-03	3.20E-03
Pancreas	5.88E-02	5.82E-02	7.70E-03	6.90E-03
Skin	2.21E-04	2.19E-04	3.10E-03	2.90E-03
Small intestine wall	6.85E-03	6.78E-03	1.50E-02	1.20E-02
Spleen	9.13E-04	9.04E-04	6.50E-03	5.80E-03
Stomach wall	1.88E-01	1.86E-01	6.50E-03	5.90E-03
Testes	2.90E-03	–	3.80E-03	3.70E-03
Thymus	7.35E-04	7.28E-04	4.10E-03	4.00E-03
Thyroid	2.28E-04	2.26E-04	5.30E-03	4.40E-03
Urinary Bladder Wall	3.07E-05	3.04E-05	1.10E-02	9.80E-02

Table 4.9: Absorbed dose coefficients (mGy/MBq) for theranostic ^{64}Cu (physical half-life = 12.701 h [56]). ICRP published values of absorbed dose coefficients (mGy/MBq) for ^{64}Cu -Ion from the ICRP Publication 53 [169] have been noted for comparing to the values obtained in this research. ‘–’ means absorbed dose in the respective organs cannot be obtained due to the physiological characteristic of the reference phantom. ‘×’ means absorbed dose in the respective organs is not available in the ICRP publication.

Organ	Present Research		ICRP Value
	JM-103	JF-103	Adult
Adrenals	2.95E-03	2.99E-03	3.00E-02
Bone surfaces	1.11E-01	1.12E-01	1.30E-02
Brain	3.06E+00	1.02E+01	1.10E-01
Breast	1.44E-02	1.42E-02	1.60E-02
Esophagus	2.47E-02	2.49E-02	×
Gallbladder wall	3.48E-03	3.42E-03	×
Heart wall	1.34E-02	1.34E-02	×
Colon wall	1.63E-03	1.62E-03	×
Kidneys	2.31E-03	2.29E-03	6.10E-02
Lungs	1.77E-02	1.78E-02	1.80E-02
Liver	5.03E-03	5.02E-03	4.80E-01
Muscles	8.79E-02	8.80E-02	×
Pancreas	2.34E-03	2.33E-03	4.80E-02
Skin	9.34E-02	9.33E-02	×
Small intestine wall	9.75E-04	9.70E-04	1.70E-02
Spleen	4.58E-03	4.49E-03	1.50E-02
Stomach wall	3.16E-03	3.13E-03	1.90E-02
Testes	6.06E-05	–	1.10E-02
Thymus	2.16E-02	2.17E-02	×
Thyroid	7.50E-02	7.55E-02	1.20E-02
Urinary Bladder Wall	2.21E-04	2.08E-04	1.20E-02

Table 4.10: Absorbed dose coefficients (mGy/MBq) for therapeutic RI ^{67}Cu (physical half-life = 2.58 d, β^- decay [56]). ICRP published values of absorbed dose coefficients (mGy/MBq) for ^{67}Cu -Ion from the ICRP Publication 53 [169] have been noted for comparing to the values obtained in this research. ‘–’ means absorbed dose in the respective organs cannot be obtained due to the physiological characteristic of the reference phantom. ‘×’ means absorbed dose in the respective organs is not available in the ICRP publication.

Organ	Present Research		ICRP Value
	JM-103	JF-103	Adult
Adrenals	1.10E+00	5.92E-01	9.40E-02
Bone surfaces	1.89E-03	1.02E-03	6.80E-02
Brain	6.74E-06	3.29E-06	5.00E-01
Breast	5.54E-04	3.42E-04	7.00E-02
Esophagus	6.11E-01	3.26E-01	×
Gallbladder wall	1.24E+01	6.71E+00	×
Heart wall	1.39E-01	7.45E-02	×
Colon wall	2.03E-01	1.09E-01	×
Kidneys	1.50E-01	8.05E-02	2.60E-02
Lungs	1.00E-01	5.40E-02	7.20E-02
Liver	1.86E+01	1.01E+01	1.80E-00
Muscles	5.45E-03	2.95E-03	×
Pancreas	9.59E-02	5.24E-02	1.80E-01
Skin	3.26E-04	1.80E-04	×
Small intestine wall	1.07E-02	5.72E-03	7.00E-02
Spleen	1.30E-03	6.64E-04	6.40E-02
Stomach wall	3.06E-01	1.67E-01	7.30E-02
Testes	1.00E-05	–	5.10E-02
Thymus	7.35E-04	3.98E-04	×
Thyroid	2.75E-04	1.29E-04	5.40E-02
Urinary Bladder Wall	1.02E-04	6.09E-05	5.60E-02

Table 4.11: Absorbed dose coefficients (mGy/MBq) for ^{123}I (physical half-life = 13.2235 h [56]). ICRP published values of absorbed dose coefficients (mGy/MBq) for ^{123}I -Iodide (Thyroid, high uptake) from the ICRP Publication 128 [165] have been noted for comparing to the values obtained in this research. ‘-’ means absorbed dose in the respective organs cannot be obtained due to the physiological characteristic of the reference phantom.

Organ	Present Research		ICRP Value
	JM-103	JF-103	Adult
Adrenals	1.40E-02	1.74E-02	6.40E-03
Bone surfaces	1.12E-02	1.42E-02	1.20E-02
Brain	3.28E-03	4.40E-03	6.30E-03
Breast	4.68E-03	6.54E-03	3.30E-03
Esophagus	9.71E-02	1.15E-01	7.70E-03
Gallbladder wall	7.74E-03	1.21E-02	5.70E-03
Heart wall	1.86E-02	1.78E-02	8.90E-03
Colon wall	9.39E-03	7.21E-03	6.90E-03
Kidneys	2.33E-02	2.98E-02	2.80E-02
Lungs	1.52E-02	1.72E-02	8.60E-03
Liver	1.07E-02	1.36E-02	7.20E-03
Muscles	5.57E-03	7.44E-03	7.60E-03
Pancreas	1.59E-02	2.18E-02	9.20E-03
Skin	3.52E-03	4.53E-03	3.50E-03
Small intestine wall	9.46E-03	1.22E-02	4.50E-03
Spleen	1.50E-02	2.64E-02	8.80E-03
Stomach wall	6.79E-02	7.28E-02	5.10E-02
Testes	2.89E-03	—	3.90E-03
Thymus	9.89E-02	9.31E-02	7.70E-03
Thyroid	5.02E+00	6.02E+00	6.00E+00
Urinary Bladder Wall	2.92E-02	2.93E-02	6.30E-02

Table 4.12: Absorbed dose coefficients (mGy/MBq) for theranostic RI ^{131}I (physical half-life = 8.0252 d [56]). ICRP published values of absorbed dose coefficients (mGy/MBq) for ^{131}I -Iodide (Thyroid uptake 55%) from the ICRP Publication 53 [169] have been noted for comparing to the values obtained in this research. ‘-’ means absorbed dose in the respective organs cannot be obtained due to the physiological characteristic of the reference phantom. ‘×’ means absorbed dose in the respective organs is not available in the ICRP publication.

Organ	Present Research		ICRP Value
	JM-103	JF-103	Adult
Adrenals	8.59E-02	9.41E-02	4.90E-02
Bone surfaces	2.81E+00	1.68E+00	1.10E-01
Brain	9.21E-02	1.43E-01	×
Breast	9.20E-02	2.26E-01	9.10E-02
Esophagus	3.80E+00	4.35E+00	×
Gallbladder wall	7.62E-02	8.99E-02	×
Heart wall	3.47E-01	3.62E-01	×
Colon wall	5.33E-02	4.43E-02	×
Kidneys	7.50E-02	8.29E-02	5.10E-02
Lung	4.65E-01	5.19E-01	1.30E-01
Liver	9.99E-02	1.07E-01	4.30E-02
Muscle	1.42E-01	2.07E-01	×
Pancreas	9.53E-02	9.82E-02	5.80E-02
Skin	8.78E-02	1.11E-01	×
Small intestine wall	1.02E-01	1.16E-01	2.80E-01
Spleen	1.13E-01	1.15E-01	5.10E-02
Stomach wall	4.15E-01	4.08E-01	4.60E-01
Testes	2.18E-02	—	2.60E-02
Thymus	4.17E+00	3.72E+00	×
Thyroid	6.44E+02	7.73E+02	7.90E-02
Urinary Bladder Wall	8.57E-02	1.00E-01	2.90E-01

Table 4.13: Absorbed dose coefficients (mGy/MBq) for ^{90}Y (physical half-life = 2.67 d [56]). ^{90}Y is using in radioembolization (or selective internal radiation therapy) for primary or metastatic liver cancer treatment [180]. ‘-’ means absorbed dose in the respective organs cannot be obtained due to the physiological characteristic of the reference phantom.

Organ	^{90}Y	
	JM-103	JF-103
Adrenals	3.82E+02	3.81E+02
Bone surfaces	8.71E-01	8.66E-01
Brain	4.67E-03	5.91E-03
Breast	1.62E-01	1.70E-01
Esophagus	2.10E+01	2.13E+01
Gallbladder wall	2.67E+01	2.68E+01
Heart wall	5.27E+01	5.26E+01
Colon wall	7.35E+01	7.33E+01
Kidneys	5.98E+01	6.06E+01
Lungs	4.46E+01	4.47E+01
Liver	7.64E+03	7.64E+03
Muscle	1.84E+00	1.85E+00
Pancreas	4.24E+01	4.29E+01
Skin	8.57E-02	8.57E-02
Small intestine wall	4.77E+00	4.69E+00
Spleen	3.06E-01	3.33E-01
Stomach wall	1.15E+02	1.13E+02
Testes	3.91E-03	—
Thymus	1.88E-01	1.98E-01
Thyroid	6.30E-02	8.98E-02
Urinary Bladder Wall	4.88E-02	4.02E-02

Table 4.14: Absorbed dose coefficients (mGy/MBq) for ^{152}Tb (physical half-life = 17.5 h [56]). ^{152}Tb is identified for PET or SPECT imaging and even it can combine to other terbium RIs (e.g., ^{161}Tb ; β^- decay) for the potential theranostic application in nuclear medicine. Müller et al. showed the first-in-human application of ^{152}Tb -PSMA-617 for PET/CT imaging of prostate cancer [181]. ‘-’ means absorbed dose in the respective organs cannot be obtained due to the physiological characteristic of the reference phantom.

Organ	^{152}Tb	
	JM-103	JF-103
Adrenals	9.46E+01	1.48E+01
Bone surfaces	4.18E+00	3.02E+00
Brain	2.14E-01	1.73E-01
Breast	6.14E+00	1.09E+00
Esophagus	5.13E+01	8.20E+01
Gallbladder wall	4.46E+02	1.74E+02
Heart wall	2.57E+01	1.82E+01
Colon wall	2.55E+01	2.77E+01
Kidneys	3.78E+01	2.06E+01
Lungs	2.11E+01	1.41E+01
Liver	1.03E+01	4.56E+01
Muscles	3.08E+00	7.75E+00
Pancreas	4.28E+01	1.36E+01
Prostate	1.24E+00	—
Skin	2.36E+00	5.12E+00
Small intestine wall	9.95E+00	1.58E+00
Spleen	8.36E+00	2.11E+00
Stomach wall	4.16E+01	4.35E+01
Testes	4.22E-01	—
Thymus	5.10E+00	1.70E+00
Thyroid	2.12E+00	5.27E+00
Urinary Bladder Wall	1.56E+00	7.10E+00

Table 4.15: Absorbed dose coefficients (mGy/MBq) for ^{161}Tb (physical half-life = 6.89 d [56]). ^{161}Tb is an interesting RI for cancer treatment, showing an alternative to the clinically-applied conventional RI ^{177}Lu (physical half-life = 6.647 d, β^- or Auger electron decay [56]) for PSMA-targeted radionuclide therapy of prostate cancer [182,183]. ‘-’ means absorbed dose in the respective organs cannot be obtained due to the physiological characteristic of the reference phantom.

Organ	^{161}Tb	
	JM-103	JF-103
Adrenals	7.97E+02	7.56E+02
Bone surfaces	1.36E+00	1.20E+00
Brain	1.91E-03	7.27E-03
Breast	3.19E-01	4.65E-01
Esophagus	4.34E+02	4.14E+02
Gallbladder wall	8.76E+03	8.50E+03
Heart wall	1.02E+02	9.58E+01
Colon wall	1.47E+02	2.75E+02
Kidneys	1.08E+02	1.03E+02
Lungs	7.22E+01	6.89E+01
Liver	1.14E+02	1.10E+02
Muscles	3.90E+00	3.75E+00
Pancreas	6.70E+01	6.47E+01
Prostate	1.29E-02	—
Skin	2.22E-01	2.31E-01
Small intestine wall	7.92E+00	7.34E+00
Spleen	7.68E-01	7.23E-01
Stomach wall	2.18E+02	2.12E+02
Testes	8.82E-03	—
Thymus	8.35E-01	4.53E-01
Thyroid	1.83E-01	5.31E-01
Urinary Bladder Wall	4.40E-02	7.09E-02

Table 4.16: Absorbed dose coefficients (mGy/MBq) for ^{166}Ho (physical half-life = 1.12 d, β^- decay [56]). The various therapeutic applications of ^{166}Ho is reviewed by Klaassen *et al.* [184]. Among them, ^{166}Ho -microspheres ($^{166}\text{HoMS}$) shows prominent to treat for patients with locoregional recurrences of head and neck squamous cell carcinoma (HNSCC) [185]. ‘-’ means absorbed dose in the respective organs cannot be obtained due to the physiological characteristic of the reference phantom.

Organ	^{166}Ho	
	JM-103	JF-103
Adrenals	1.14E+01	1.05E+01
Bone surfaces	2.18E-02	2.01E-02
Brain	1.35E-04	1.24E-04
Breast	5.82E-03	5.38E-03
Esophagus	6.15E+00	5.68E+00
Gallbladder wall	9.27E+01	8.56E+01
Heart wall	1.53E+00	1.42E+00
Colon wall	2.20E+00	2.03E+00
Kidneys	1.41E-02	1.30E-02
Lungs	1.81E-01	1.67E-01
Liver	3.06E+02	2.83E+02
Muscles	5.45E-02	5.03E-02
Pancreas	1.18E+00	1.09E+00
Skin	2.57E-03	2.38E-03
Small intestine wall	1.32E-01	1.22E-01
Spleen	1.03E-02	9.53E-03
Stomach wall	3.34E+00	3.09E+00
Testes	1.98E-04	—
Thymus	5.35E-03	4.94E-03
Thyroid	2.21E-03	2.04E-03
Urinary Bladder Wall	9.60E-04	8.87E-04

From Table 4.6 to Table 4.16, the absorbed dose coefficients (in mSv/MBq) have meaning for patient's dosimetry in nuclear medicine applications due to the diversified estimated results than the reported reference values of the ICRP publications. Since the patient-specific dosimetry requires more specific anatomical and physiological models therefore, these results have potential importance in the diagnostic and therapeutic planning at the clinical nuclear medicine. In addition, external radiation doses like X-ray, CT, or IMRT therapy can be precisely predicted by using conventional models or the latest Monte Carlo based method, and also the internal dose of inhalation and ingestion can be determined by using dose coefficients listed in ICRP Publication 119 [186]. In contrast to that, however, the precise dose calculation method of "administrated medical RIs" has not been established yet. From this point of view, the dose coefficient list for different emergent medical RIs given in these tables (Table 4.6 – Table 4.16) may contribute as a quick data table in the clinical nuclear medicine department especially to preclinical investigations. Even organ/tissue absorbed dose results generated by the developed PHITS-based method can be the guideline for national/regional radiation protection guidelines since for the use of Japanese averages data of the JM-103 and JF-103 voxel phantoms.

4.5 Uncertainty in internal dosimetry

The relevance of the uncertainty in internal dosimetry depends on the applying of the dosimetric data. For instance, when using ^{177}Lu for therapy, the kidneys are the limiting organs in danger and dose estimates in keeping with patient-specific calculations have an uncertainty of 6% (1 standard deviation) [187]. Roedler [188] showed that using reference phantoms the real patient dose within lower for radionuclides with short half-life e.g. $^{99\text{m}}\text{Tc}$ [140,189,190]. The tissue weighting factors given in ICRP Publication 103 for radiation-induced biological effects are defined for all populations, ages, and sexes. Thus, applying these factors on individuals or subgroups is wrong and so this uncertainty is irrelevant. The uncertainties within the tissue weighting factors do not seem to be within the scope of this work.

Also, the uncertainties of biokinetic modeling of long-lived isotopes for an age and sex independent population are unknown. For long-lived isotopes, there are still not enough data available to construct a biokinetic model. For example, for long-lived indium isotopes, there are still not enough data available to construct a biokinetic model. So that, after about 100 days the erythrocytes dies, and indium is recycled. Therefore, the uncertainties in the long-term fitting to the model are difficult to estimate [191].

This research calculates JM-103 and JF-103 voxel's organs/tissues absorbed doses by PHITS simulation and then the effective dose for risk assessment, as it is already described in Fig. 4.4. Note that, Monte Carlo particle transport simulation-PHITS uncertainty estimated method explained in detail by Hashimoto *et al.* [192].

In this research, PHITS simulated values of absorbed doses include relative uncertainty less than 5% which only may do reflect the overall uncertainty of the dose estimations. For example, for ^{47}Sc , Table 4.2 shows the internal radiation doses where the whole-body effective dose per administered activity of ^{47}Sc included uncertainty 2.58×10^{-4} mSv/MBq (i.e., less than 0.10% of measured whole-body effective dose coefficient).

4.6 Conclusion

For the radiopharmaceuticals utilized in nuclear medicine absorbed doses are estimated for radiation protection purposes with a way using a “standard” patient geometry. The absorbed dose calculations are based on models of the human body and also the radiopharmaceutical’s behavior within the body. This chapter focused on revising absorbed dose calculations by using PHITS simulation by implementing mathematical models described by CT images generated on real Japanese volunteers called the Japanese voxel phantoms JM-103 and JF-103. Together with the adaptation of the voxel phantoms (i.e., JM-103 and JF-103), the updated definition of effective dose published in the ICRP Publication 103 has been implemented. This research has been applied to the absorbed doses to organs/tissues in mGy/MBq and also the effective dose coefficient calculation for a few emergent medical RIs like ^{47}Sc , $^{64,67}\text{Cu}$, ^{90}Y , $^{152,161}\text{Tb}$, ^{166}Ho , etc. with other frequently used RIs (e.g., ^{18}F , $^{99\text{m}}\text{Tc}$, $^{123,131}\text{I}$, etc.). Estimated results showed considerable dissimilarities to the ICRP recommended values in some cases. This made the importance of the new PHITS based dose estimations using JM-103 and JF-103.

Since dosimetry in nuclear medicine is completely patient-specific. In order that dosimetry calculations involving patient-specific geometries are generally not performed. However, in this chapter, the absorbed dose coefficients in mGy/MBq in different organs/tissues are listed for some future prospective medical RIs which are showing in prominent nuclear medicine applications concerning their suitability of the uses as radiopharmaceutical. The present results are a good reflection of the organ doses of the Japanese references and as well as the Asian personal. Therefore, these dose coefficients would be a guideline for the medical physics researchers rather than clinical reference, especially for the Asian people’s body geometry.

In the end, the ICRP/ICRU reference adults, AM and AF, has completely different anatomical and physiological characteristics than JM-103 and JF-103, so the results obtained in this research would be the reference for internal dosimetry in nuclear medicine for the Japanese and as well as the Asian peoples.

5. Radiation Dose from Patient

When the patient is kept in hospital following radionuclide therapy, the people at risk of exposure include clinical staff who may or may not be radiation workers or carers¹. This is a significant problem. On the other hand, once the patient has been released, the groups at risk include members of the patient's family, including children, and carers; they may also include neighbors, visitors to the household, co-workers, those encountered in public places, on public transport or at public events such as entertainments, and finally the general public. Safety issues for the patient, their family, associated carers, staff, and the general public arise with either approach.

The exposure of other persons by patients who have received radionuclide therapy can occur in the following ways [193]:

1. External irradiation of persons close to the patient.
2. Internal contamination of persons as a result of excreted or exhaled radionuclides.

In addition to both above, exposure of those immediately involved with the patient and the general public can occur through environmental pathways including sewerage, discharges to water, incinerated sludge, or cremation of bodies. From the individual doses involved, this is of relatively minor significance.

External irradiation of the persons close to the patient is related to the radionuclide used, its decay characteristics, half-life, and biokinetics, which can be important with some radionuclides. However, the dose limits recommended by the ICRP and the IAEA for members of the general public, patients, and carers are set out in Table 5.1. Furthermore, there are dose constraints for carers, and some countries also provide dose constraints for staff [46,160,194,195]. This may, in special circumstances, be subject to averaging over five years, and weighting for the age of the exposed persons.

¹Individuals who knowingly and voluntarily accept exposure while helping others undergoing medical diagnosis or treatment (other than in their occupation) are referred to as comforters and/or carers.

Table 5.1: ICRP Publication 60 & 103 and IAEA recommended annual dose limits.

Application	Public dose limit	Patient, comforter and carer dose limit
Effective dose	1 mSv/year*	No dose limit
Annual equivalent dose in:		
Lens of the eye	15 mSv	No dose limit
Skin	50 mSv	No dose limit

* In special circumstances, a higher value of effective dose could be allowed in a single year, provided that the average over five years does not exceed 1 mSv/year. From ref. [46,160,194].

Good estimates of the external dose from patients to whom radionuclide has been administered are available and have recently been summarized by the ICRP [196-201]. These documents reinforce the conclusion that doses to other persons from treated patients are predominantly the result of external exposures. Without precautions, it is possible to envisage doses up to several orders of magnitude higher than the dose limits or dose constraints [202]. The ICRP and others are careful to draw attention to the many methodological issues that can compromise external dose calculations including, e.g., the assumption that the activity in patients behaves as a point source.

This chapter concerns the development of PHITS based estimation of external dose coming from the patient as point source who followed by radionuclide therapy. For area or workplace monitoring, the operational quantity, namely, the ambient dose equivalent, $H^*(d)$, estimated according to the definition given by the ICRU. This operational quantity is important for safety issues for the patient, their family, associated carers, staff, and the general public.

5.1 Operational quantities for area monitoring

Section 4.1 of Chapter 4 explained the operational quantities defined by the ICRU (see Fig. 4.2). For area or workplace monitoring, two quantities, namely, the ambient dose equivalent, $H^*(d)$, and the directional dose equivalent, $H'(d, \Omega)$, are used to link external radiations to the effective dose and the equivalent dose to the lens of the eye and local skin. Where, $H^*(d)$ at a point in a radiation field, is the dose equivalent that would be produced by the corresponding aligned and expanded field in the ICRU sphere, at a depth d on the radius opposing the direction of the aligned field [46]. For strongly penetrating radiation, the recommended depth is 10 mm so the ambient dose equivalent for strongly penetrating radiation is $H^*(10)$. When the specified radius is parallel to the radiation field (i.e. when $\Omega = 0^\circ$), the

quantity $H'(d, \boldsymbol{\Omega})$ may be written simply as $H'(d)$. Furthermore, in a unidirectional field, $H'(d) = H^*(d)$.

5.2 $H^*(10)$ for safety issues: a PHITS study

To calculate $H^*(10)$, a Monte Carlo based PHITS [32] simulation was studied. Here, the simulated estimation is based on:

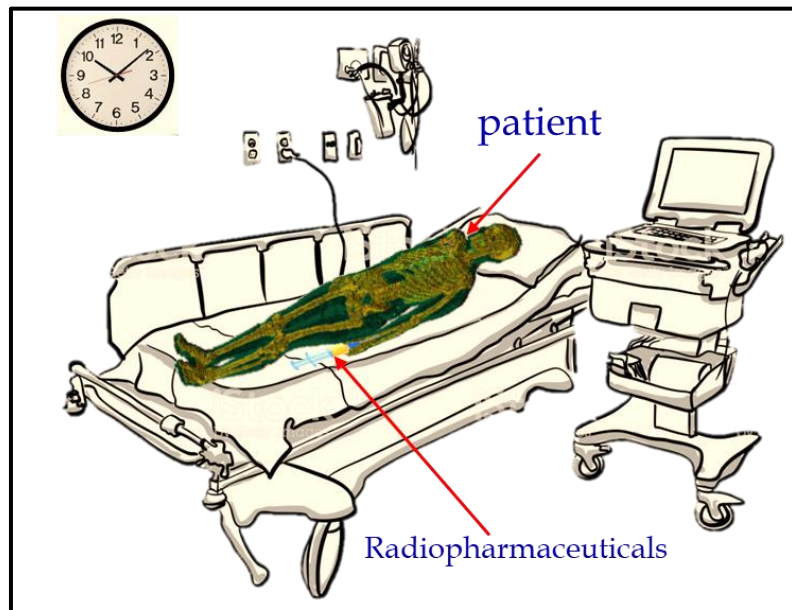
- 1) the dose equivalent occurring at a depth of 1cm (= 10 mm) from the surface of an ICRU 4-element tissue, called an ICRU sphere, the ICRU sphere is a 30 cm in diameter, made of tissue-equivalent material with a density of 1 g/cm³ and an elemental composition (by mass) of 76.2% oxygen, 11.1% carbon, 10.1% hydrogen and 2.6% nitrogen [203];
- 2) the definition of dose equivalent according to the ICRP Publication 103 [46],

$$H = D \cdot Q(L) \quad (\text{Sv}) \quad (5-1)$$

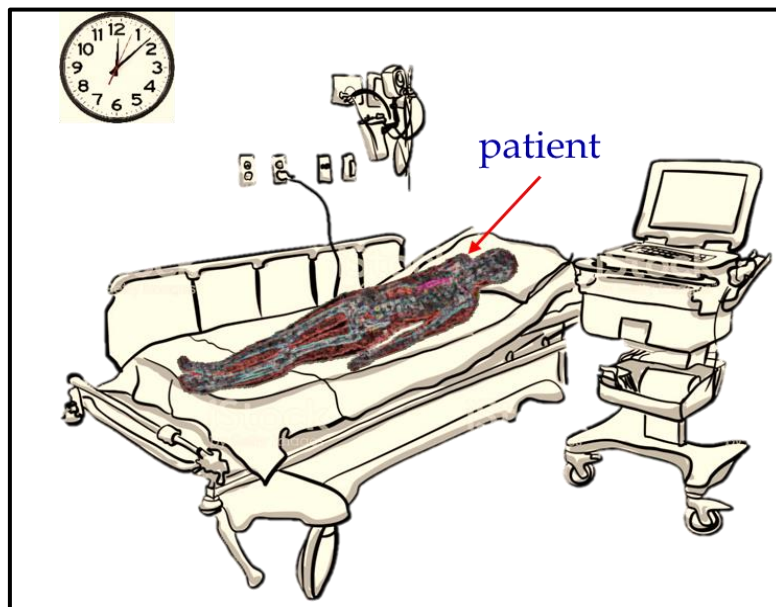
where D is the absorbed dose in a 1 mm³ cube situated at a depth of 10 mm from the surface of an ICRU sphere and $Q(L)$ is the quality factor for the specific radiation at a point in tissue and is characterizing the biological effects of radiation, based on the ionization density along the tracks of charged particles in tissue.

In PHITS simulation, for the calculation of deposition energies at a depth of 10 mm from the surface of an ICRP sphere, quality factor $Q(L)$ can be multiplied by setting the parameter, “dedxfnc = usrdfn 1.f”, in [t-deposit] tally. This program returns the dose equivalent from the product of the deposited energy with the $Q(L)$ relationship defined in the ICRP Publication 60 [160]. However, ICRP keeps the same definition of $Q(L)$ in their latest recommendations [46] so that the $H^*(10)$ calculation result ultimately appears based on the ICRP Publication 103.

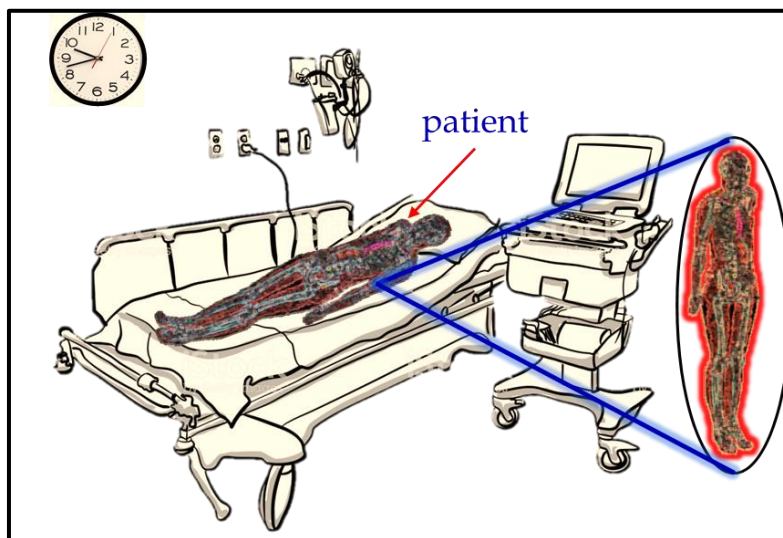
By following the above bases, $H^*(10)$ was calculated by PHITS simulation. Procedures of the calculation of $H^*(10)$ by PHITS simulation are illustrated in Fig. 5.1. In the figure, it is demonstrating how a patient becomes a source of external exposure to surrounding people after nuclear medicine applications.



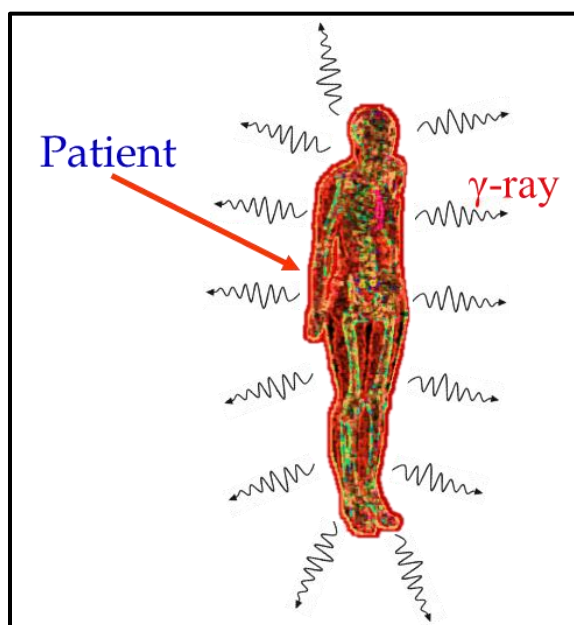
(a)



(b)



(c)



(d)

Fig. 5.1: An illustration of how a patient can be a source of external exposure to clinical staff or take carers after nuclear medicine treatment. (a) administration of radiopharmaceuticals to the patient for the treatment of any specific disease, (b) biodistribution of radiopharmaceuticals in the whole body of the patient after a certain period, (c) as time goes, patient acts as a source of external radiation exposure, and (d) emission of γ -rays from the patient body parts.

From Fig. 5.1, in the end, emitted γ -rays from the patient's body is the source of radiation that can expose the surrounding peoples. Therefore, proper dosimetry is required to estimate safety issues according to the ICRP and IAEA guidelines. To do so, this research-based on PHITS simulation stored the source information by creating the universal source calculation of 'dump' files. PHITS developed some special features to calculate 'dump' files. The following section will provide more information in detail.

5.3 Universal radiation source calculation of RI administrated patient: "dump" file

Figure 5.2 shows a patient spreading out γ -radiation in all directions from its body surface. These γ -photons can transmit to other's bodies depending on the kinetic energy and the directions of the emitted particles. Moreover, the information can be stored as a 'dump' file by PHITS execution for universal radiation source calibration. The importance of the 'dump' information is - it can use to calculate $H^*(10)$ for safety issues for clinical staff and carers. Apart from this advantage, these files can also be used for further research purposes of external dosimetry without having a real patient as a source of radiation. This research is completely a new development of particle information 'dump' for external radiation dosimetry.

In PHITS simulation, the Japanese voxel phantoms, JM-103, and JF-103 were supposed as therapeutic patients. The body height of the patient was considered as vertical distribution (see Fig. 5.2, vertical direction mentioned along the z -direction). The consideration of the patient body geometry has been taken from the real situation of patient movements that is happened after the treatment. Of course, patients must follow clinical guidelines when they stay in the hospital or after release from the hospital regarding their movements.

To dump transmitted particle information an arbitrary cylindrical surface was constructed surrounding the patient body along the same direction of patient height i.e., z -direction. This arbitrary cylindrical surface cannot modify the particle energy or direction or nature of the particle to other types by any nuclear reaction or in any other way. Dimensions of this arbitrary cylindrical surface have been chosen randomly but keep in mind the phantoms, JM-103, and JF-103 physical properties. Table 4.1 in Chapter 4 shows the physical properties of the Japanese voxel phantoms. So that, in the present situation an arbitrary cylindrical surface having 195 cm of height and 30 cm of the radius was constructed in the PHITS simulation input. The reason for the selection of higher cylindrical dimensions than patient body geometries is to allow the particles to transmit through the surface from the patient body. That means particle direction is always along the outward direction from the surface of the cylindrical periphery (see Fig. 5.2).

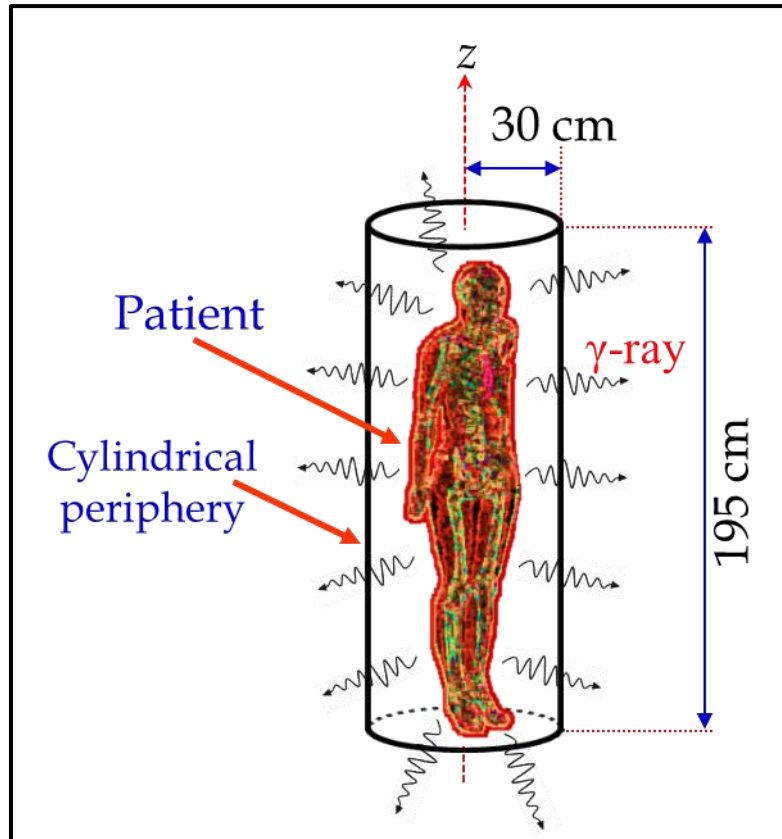


Fig. 5.2: Information on the particles can be dumped when crossing a cylindrical peripheral enclosing surface from the patient after nuclear medicine applications.

At this instant, to create a ‘dump’ file by the [t-cross] tally of PHITS input, information on the particles can be dumped in the file by the PHITS parameter of “dump =”. Where the number of dumped data in one record is specified. This research uses the ‘dump’ option for [t-cross] tally in MPI parallel computing and the data were read as ASCII data. In the ASCII file, information of the particle type, position coordinates (cm), the unit vectors of the direction of the particle, and the energy (MeV) created for writing and reading dumped data.

In this research, PHITS simulation input has been prepared to create ‘dump’ files by setting 16 cores of parallel computing option. When these options are used in parallel computing, PHITS makes 15 ASCII files for writing the dump information from each node. For a patient (for JM-103) after ^{47}Sc therapy and 11250000 (= maxcas*maxbch) histories, 15 ASCII files were created within a CPU time of approximately 20 min and requires 26.3 MB storage. Under these conditions, calculations were completed with the statistical uncertainties of less than 5%. An example of the universal radiation source file is shown in Fig. 5.3.

5.3.1 Reading ‘dump files’ for $H^*(10)$ calculation

PHITS can also read the ‘dump’ files under parallel computing. By setting “s-type=17” (reading dump file) in the source section, information on particles recorded in a file can be used as sources. The ‘dump’ files obtained by using the dump option in the [t-cross] tally. The total number of histories of the previous step is adopted from the values of maxcas and maxbch written in this PHITS input file.

Moreover, created ‘dump’ files were applied to calculate the ambient dose equivalent, $H^*(10)$. As it was written, for all types of external radiation, the operational quantities for the area or workplace monitoring are defined based on a dose equivalent value at a point in a phantom, the ICRU sphere, which is already mentioned in section 5.2 of this chapter. So, this research used ‘dump’ files as a source of external radiation and calculate $H^*(10)$ according to guidelines provided by the ICRU and the latest recommendations published in the ICRP Publication 103. Figure 5.4 is showing a schematic view of the PHITS simulation geometry for $H^*(10)$ calculation.

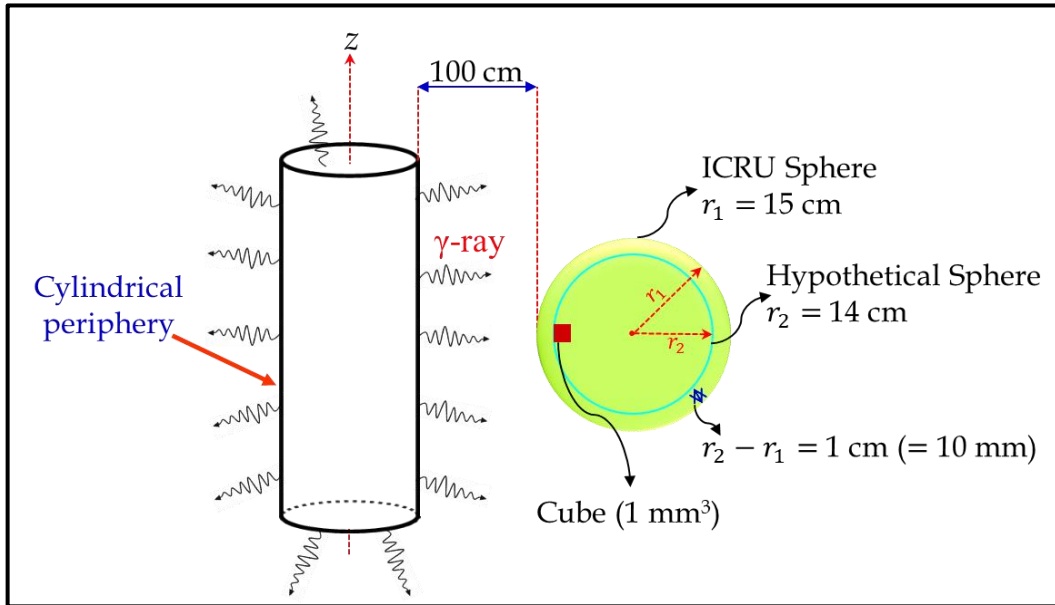


Fig. 5.4: Schematic view of the geometry of PHITS simulation for $H^*(10)$ calculation inside an ICRU sphere.

It is clear from Fig. 5.4, an ICRU sphere was implemented at 100 cm (= 1 m) from source geometry (because γ radiation levels at a distance of one meter have been measured in case of a source of external exposure). Where sources are used as the particle information recorded in the ‘dump’ files. The energy deposition from γ photons occurring at a depth of 1 cm (= 10 mm) from the surface of an ICRU sphere placed in a field where radiation is coming from one direction. At the depth of 10 mm, a cube having a 1 mm³ dimension was selected for absorbed dose estimation. Since radiation quality factor $Q(L)$ has been confirmed in PHITS simulation input so that the ambient dose equivalent, $H^*(10)$, can be calculated by using Eq. (5-1).

To validate the universal radiation source calculation for $H^*(10)$ calculation, this research applied PHITS simulation. Table 5.2 shows the result of the PHITS simulation for some emergent therapeutic radionuclides which are showing promising not only in nuclear medicine therapy but also in theranostics applications.

Table 5.2: PHITS simulated ambient dose equivalent, $H^*(10)$, for the area or workplace monitoring for safety issues from further radiation exposure.

Theranostic Radionuclide(s) ^a	$H^*(10)$ in mSv for a person ^b when ‘dump’ files calculated with patient as:	
	JM-103 (\pm error)	JF-103 (\pm error)
⁴⁷ Sc	1.412 (\pm 6)	1.457 (\pm 7)
⁶⁴ Cu	1.286 (\pm 6)	1.248 (\pm 5)
⁶⁴ Cu/ ⁶⁷ Cu	1.447 (\pm 7)	1.453 (\pm 6)

^aphysical half-life of ⁴⁷Sc, ⁶⁴Cu, and ⁶⁷Cu is 3.3492 d, 12.7 h, and 2.58 d, respectively [56]; ^bperson means anybody of clinical staff or associated carers.

Results showed in Table 5.2 is only the demonstration of PHITS calculation for $H^*(10)$. It is of course the procedures described in this calculation can be extended for any other radionuclide which is using in therapeutic or theranostic purposes in clinical nuclear medicine. Furthermore, if the situation of radiation exposure on the ICRU sphere is assumed for a unidirectional field then these results can be equated to the other operational quantity called the directional dose equivalent, $H'(10)$. Moreover, according to the ICRP Publication 103, the $H^*(10)$ is commonly used as a surrogate for the quantity effective dose equivalent because of dose estimation to 10 mm depth in soft tissue equivalent material of the ICRU sphere. So that, $H^*(10)$ is the effective dose equivalent that we evaluate for purposes of radiation protection. Since the determination of the effective dose

requires knowing the doses delivered to all the major organs in the body, it is not a practical dose quantity to attempt an evaluation of the routine operations involving external source, personal dose equivalent.

In practical situations, radiation fields are often not aligned and expanded, although most photon fields we measure are sufficiently extensive to at least cover the dimensions of the detector being used. $H^*(10)$ was devised as a satisfaction more than as a representation of reality. Such “satisfactions” are often necessary compromises to have a system that can be implemented practically, uniformly, and reasonably easily. Consider how impractical, indeed impossible, it would be to attempt to calibrate instruments to account for all possible variations in the radiation field that might be experienced in the field. So, $H^*(10)$ is an operational quantity intended for field use. What is important is that it provides an acceptable approximation to the actual dosimetric quantity of interest e.g., effective dose equivalent, preferably with errors being in the conservative direction. This is true for the quantity $H^*(10)$.

For more discussion, since there is no recommended dose limit of $H^*(10)$ for clinical staff and carers (see Table 5.1) so this calculation can extend in the area or workplace monitoring dosimetry. It is noted that the result showing in Table 5.2 cannot use for any recommendation. However, these could a guideline for the ICRP, ICRU, IAEA, or other international bodies who would like to set-up recommendations for safety issues. Also, the values of $H^*(10)$ listed in Table 5.2 is not comparable between radionuclides and/or patient types in anyways. Because patient-specific radionuclide therapy or theranostic applications is disease dependent clinical application.

5.4 Conclusion

For the area or workplace monitoring of external radiation, new techniques are emerging. PHITS based technique for the ambient dose equivalent, $H^*(10)$ calculation is a different method of the area or workplace monitoring than the conventional method by using conversion coefficients for the photon. Moreover, the techniques of the universal radiation source calculation by ‘dump’ file creation can play an important role in medical dosimetry research of clinical nuclear medicine applications. Also, demonstration of the described method of $H^*(10)$ calculation for some theranostic radionuclides (e.g., ^{47}Sc , ^{64}Cu , and $^{64}\text{Cu}/^{67}\text{Cu}$) replies to the successful reading of the created ‘dump’ files. This method would be useful for safety issues for the patient, their family, associated carers, staff, and the general public.

6. Dosimetry of Occupational Exposure from ^{132}Cs

Radiation exposure may be internal or external and can expose to humans through various exposure pathways. One of the areas of exposure of humans to ionizing radiation at the workplace is occupational radiation exposure of workers.

For occupational exposure to internal radiation, the main route of radionuclides intake is by inhalation, some by ingestion and absorbed by the skin through cuts or wounds. Because the radionuclides are potential sources of radiation exposure to workers, it is important to assess exposure doses prospectively for radiation protection. For internal dose estimation, ICRP has developed dose coefficients for radionuclide intake by workers [186] based on the ICRP Publication 60 [160]. Now a day, ICRP has been developing revised dose coefficients for internal exposure in accordance with the latest ICRP Publication 103 [46] as a series of publications called “Occupational Intakes of Radionuclides (OIR) series” [204-207]. Also, various computational codes have been developed to calculate dose coefficients based on a dosimetric methodology following the ICRP Publication 60, such as Dose and risk CALculation software (DCAL) [167], Integrated Modules for Bioassay Analysis (IMBA) [208] and MONitoring to Dose cALculation (MONDAL) [209]. Besides these codes, Manabe *et al.* [210] constructed a computation algorithm to derive dose coefficients by using the current methodology of ICRP Publication 103.

On the other hand, ICRP Publication 119 [186] has provided dose conversion coefficients for use in occupational radiological protection against external exposure radiation based on the ICRP Publication 60 by compiling coefficients provided previously in the ICRP Publication 74 [41]. Where dose conversion coefficients were derived assuming whole-body irradiation by mono-energetic photons, electrons, and neutrons in several idealized standard exposure geometries on an adult anthropomorphic computational model described by Cristy and Eckerman [147]. For external radiation to the body, it is possible to define a set of operational quantities for specific external exposure geometries which are measurable in terms of the basic physical quantities. Individual monitoring of external exposure by active or passive means can be measured by an expensive dosimeter calibrated in terms of the operational quantities. Then dose conversion coefficients can be used to allow users to calculate protection quantities from operational quantities.

Therefore, ICRP provided information on the occupational exposures to external sources of radiation via the current updated publication, ICRP Publication 119, demands a change in dose conversion coefficient calculations using:

1. the more updated Japanese computational voxel phantoms, JM-103 and JF-103, or the latest ICRP/ICRU adult reference phantoms published in the

ICRP Publication 110 [44] instead of an adult anthropomorphic computational model described by Cristy and Eckerman [147], and

2. the latest ICRP recommendations published in the ICRP Publication 103 [46] by replacing the ICRP old recommendations published in the ICRP Publication 60 [160].

So that, this research motivated to calculate the model-based protection quantities for occupational exposure to external sources of radiation to a reference person under the Antero-posterior (AP) geometry². In this regard, absorbed dose coefficients (mGy/MBq) in organs/tissues have been calculated for JM-103 and JF-103 as a reference person by using a Monte-Carlo code PHITS. Where the external radiation irradiates to a reference person are emitting from ¹³²Cs (physical half-life = 6.48 d, maximum $I_\gamma = 97.59\%$ at $E_\gamma = 668$ keV [56]) contaminated soil samples. After that, the equivalent dose and the effective dose were calculated in accordance with the latest recommendations of ICRP published in the ICRP Publication 103.

6.1 Materials and methods

6.1.1 Source of external exposure

A significant amount of radioactive material was discharged into the environment by the accident at the Fukushima Dai-ichi nuclear power plant in Japan on 11 March 2011. The radioactive materials were widely deposited on the ground around the accident area, where they elevated the radiation dose [211]. Due to the relatively long half-lives of cesium and higher energy radiated photons, radioactive cesium deposited on the ground after the accident. This is one of the most important nuclides for estimating medium-term to long-term doses resulting from external exposure.

Chapter 3 of this thesis described the production of a RI, ¹³²Cs. The environmental tracer, ¹³²Cs, can be used as an alternative of ¹³⁷Cs. The feasibility study of ¹³²Cs tracer has been conducted with three different types of soil samples and the experimental procedures were demonstrated in Fig. 3.6 under section A.3.3.1 of Chapter 3. At the time of experimental procedures, γ -rays emitted from radioactive ¹³²Cs enter the occupational radiation worker's (ORW) body as an external exposure. Since the distance between the ¹³²Cs contaminated soil cylinder and the ORW was less than a meter so there is a possibility that the ORW may be

² Antero-posterior (AP) geometry - the irradiation geometry in which a monoenergetic parallel beam of ionizing radiation is incident on the front of the body in a direction orthogonal to the long axis of the body [212]

exposed to the emitted radiation externally. Figure 5.1 shows the situation in a schematic view.

Of course, the operational quantities for exposure to external γ -rays are directly monitored by a personal dosimeter. So, the protection quantities can be calculated by using the conversion coefficients published in ICRP Publication 119 (based on ICRP Publication 60). But it is not too advantageous as the related causes were already discussed in the previous section.

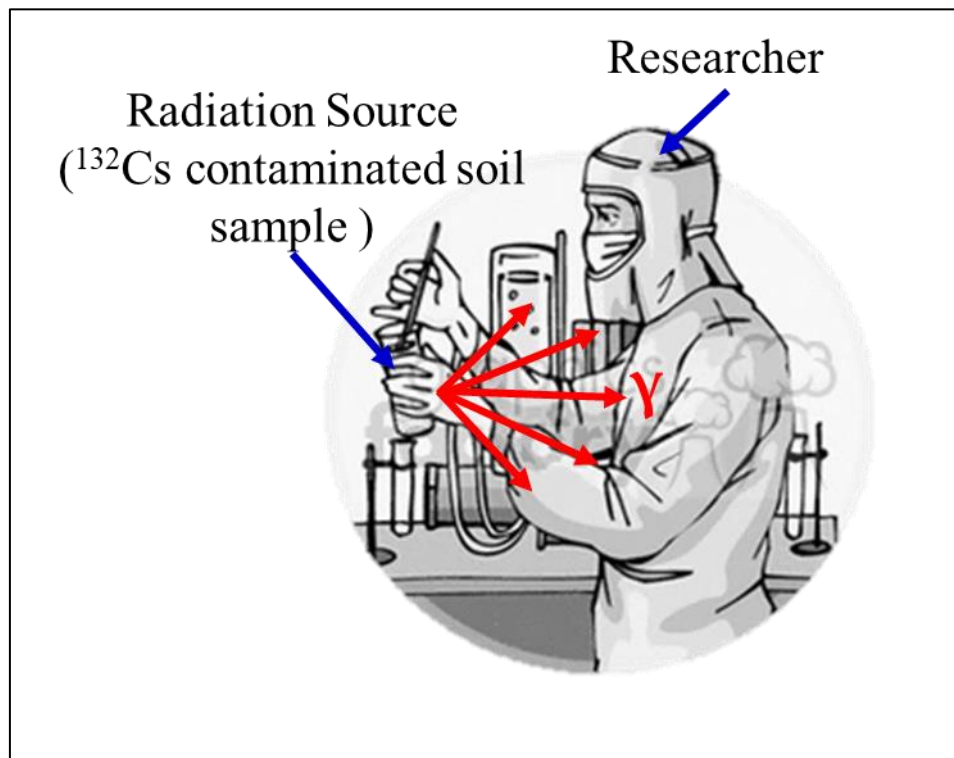


Fig. 6.1: Schematic view of the demonstration of how an ORW exposed to an external radiation source during handling radioactive substances for research purposes.

6.1.2 Dosimetric methodology and reference phantoms

This research reviewed the definition of the protection quantity ‘the equivalent dose’ and ‘the effective dose’ from the ICRP Publication 103 [46]. These quantities are calculated from the physical quantity absorbed dose for different organ/tissue of an ORW exposure to external γ -radiation from radioactive ^{132}Cs contaminated soil samples. In this research, the reference phantoms, JM-103 and JF-103, are used to compute the mean absorbed dose, D_T , in an organ/tissue T , from γ -radiation external to the body. The effective dose is then computed from the equivalent doses assessed for organ/tissue T of JM-103, H_T^M , and JF-103, H_T^F , according to the following equation:

$$E = \sum_T w_T \left[\frac{H_T^M + H_T^F}{2} \right] = \sum_T w_T \sum_R w_R \left[\frac{D_{T,R}^M + D_{T,R}^F}{2} \right], \quad (6-1)$$

where w_T and w_R is the tissue weighting factor for tissue T and the radiation weighting factor for radiation R , respectively. ICRP Publication 103 recommended these factors [46].

From the practical experience and the analogy of Fig. 5.1, the total procedure was implemented in PHITS. Implementation of JM-103 and JF-103 voxel phantoms to PHITS simulation for organ/tissue absorbed dose calculation described in Sec. 4.2.3 of Chapter 4. Since γ -radiation emitted from ^{132}Cs contaminated soil samples are irradiating the ORW’s body, the absorbed doses in organs/tissues can be calculated for the ‘AP’ irradiation geometry. Finally, the risk of radiation incidence can be calculated by using Eq. (6-1). The result will mean the whole-body effective dose.

6.2 Results of dose estimations

Absorbed dose coefficients (mGy/MBq) for organs/tissues of ORW were estimated by PHITS simulation in accordance with the ICRP Publication 103 [46]. The mean absorbed dose in an organ, or a tissue is defined as:

$$\bar{D}_T = \frac{\int_T D(x, y, z) \rho(x, y, z) dV}{\int_T \rho(x, y, z) dV} \quad (6-2)$$

where \bar{D}_T , T , $D(x, y, z)$, $\rho(x, y, z)$, and V is the mass-averaged absorbed dose of the entire target T , the target region (i.e., organ or tissue, bones), the absorbed dose as a function of target region position coordinates, the density as a function of target

region position coordinates, and volume of the target region, respectively. The absorbed dose is the target region and its geometry (size, shape, and position) dependent. This is why a personal dosimeter (e.g., TLD) cannot measure the organ/tissue dose specifically but can measure only the overall dose measurement by the quantity called personal dose equivalent. Therefore, to protect the critical organs to external sources of radiation exposure, the dosimetry of each body part is required for concern of radiation protection.

Occupational exposure due to an environmental tracer ^{132}Cs can cause the organ/tissue absorbed dose during its handling period. For the irradiation geometry AP, Table 6.1 shows the dosimetric results of the protection quantity, \bar{D}_T using Eq. (6-2) when γ -rays ($E_\gamma = 668 \text{ keV}$) interact into the ORW's whole-body from 100 cm apart for 1 hour. According to the ICRP Publication 103, the radiation weighting factor, $w_R = 1$ for the photon. So, the equivalent doses to organs/tissues will be the same as the absorbed dose to the respective organ/tissue. In an actual case, external radiation interact with the ORW is a single person phenomenon. So that the whole-body risk of radiation incidence is calculated on sex-specific rather than ICRP 2007 recommendations of the sex-averaged effective dose. Therefore, this research estimated the sex-specific whole-body effective dose for JM-103 and JF-103 separately by considering them as an ORW according to the old ICRP 1990 recommendations (see Table 6.1). Moreover, as a theoretical estimation, we calculated the sex-averaged whole-body effective dose by using Eq. (6-1) too. For ^{132}Cs contaminated soil sample, the sex-averaged whole-body effective dose is estimated at $3.29 \times 10^{-4} \text{ mSv}$ with 1.82% statistical error.

Table 6.1 shows that the absorbed dose coefficients for JM-103 were estimated higher than JF-103 in almost all organ/tissue with an exception in some parts such as adipose tissues, eye lens, gallbladder wall, muscles, etc. Because of the larger anatomical geometry of JM-103, a high amount of radiation energy can deposit on the large volume of the respective target regions. Ultimately the whole-body effective dose raised to the more radiological risk for JM-103 than the cases happening for JF-103. In contrast, this phenomenon is opposite to the radiation risk development events in the internal dosimetry of RI administration where small organ/tissue can process a more absorbed dose due to its lightweight. That means the mass of the organ/tissue is more important for the absorbed dose estimation in internal dosimetry than the volume and the flux of the inward incident radiation for an external dosimetry. The values of the effective doses in different aspects of the calculation procedure are shown in Table 6.1.

Table 6.1: Absorbed dose to organ/tissue of a person for an occupational exposure of ^{132}Cs . This physical quantity can proceed to calculate the protection quantity, ‘the sex-averaged effective dose’ based on ICRP Publication 103. ‘–’ means absorbed dose in the respective organs cannot be obtained due to the physiological characteristic of the reference phantom.

Organ/Tissue	Absorbed Dose (mGy/MBq)	
	JM-103	JF-103
Adipose tissues	3.24E-03	4.86E-03
Adrenals	2.80E-03	2.34E-03
Bones	3.91E-03	3.86E-03
Brain	2.37E-03	1.57E-03
Breasts	7.89E-03	5.41E-03
Bronchi	3.73E-03	3.34E-03
Esophagus	3.66E-03	2.88E-03
ET region	4.00E-03	2.00E-03
Eyes	1.77E-05	2.03E-03
Eye lenses	1.33E-04	2.72E-03
Gallbladder Content	6.96E-03	7.79E-03
Gallbladder wall	7.35E-03	8.25E-03
Heart Content	4.51E-03	3.48E-03
Heart wall	4.53E-03	3.47E-03
Left colon wall	3.41E-03	1.25E-03
Right colon wall	6.59E-03	6.68E-03
Kidneys	3.49E-03	3.28E-03
Lungs	4.51E-03	4.22E-03
Liver	6.23E-03	6.91E-03
Lymphatic nodes	4.28E-03	3.47E-03
Meninges	2.54E-03	1.75E-03
Muscles	3.28E-03	4.92E-03
Oral mucosa	3.03E-03	1.66E-03
Pancreas	4.21E-03	2.81E-03
Prostate	2.67E-03	–
Salivary gland	4.61E-03	2.37E-03
Skin	3.18E-03	9.81E-03
Small intestine Content	4.34E-03	2.71E-03
Small intestine wall	4.49E-03	2.88E-03
Spleen	1.78E-03	9.59E-04
Stomach Content	4.10E-03	1.89E-03
Stomach wall	4.61E-03	2.13E-03
Testes	4.42E-03	–

(continued on next page)

<i>(continued)</i>		
Thymus	4.58E-03	3.12E-03
Thyroid	5.83E-03	1.45E-03
Tongue	4.21E-03	2.18E-03
Trachea	4.28E-03	2.61E-03
Urinary Bladder Content	3.55E-03	1.65E-03
Urinary Bladder Wall	3.75E-03	1.74E-03
Effective dose (mSv)	3.75(± 0.09)E-04	2.83(± 0.03)E-04
Sex-averaged	3.29(± 0.06)E-04	
Effective dose (mSv)		

Estimation of organ/tissue absorbed dose is dependent on exposure geometry. A typical working environment can result in multiple exposure geometries. This means radiation dose calculated in AP geometry from occupational exposure of ^{132}Cs may vary from other geometries. From Table 6.1, the estimated absorbed dose in each organ/tissue is numerically much lower than the ICRP reported threshold doses for deterministic effects of radiation [137]. For example, for occupational exposure in planned exposure situations, the ICRP now recommends an equivalent dose limit for the lens of the eye of 20 mSv/year, averaged over defined periods of 5 years, with no single year exceeding 50 mSv. Since the ICRP emphasizes that protection should be optimized not only for whole-body exposures but also for exposures to specific tissues. However, the calculated sex-specific effective dose in this research does not exceed the recommended dose limit of early and late effects of radiation in normal tissues and organs concerning radiation protection (see Table 6.1).

In occupational dose monitoring programs, dosimeter badges are commonly used to assess compliance with prescribed exposure limits. Because the dosimeter badges measure the dose delivered at a specific point on the body, and not to the actual organ, a method has been developed by the ICRP to convert the regulatory compliance dose (monitored dose) to a dose to the affected organ or tissue.

This research has a different aspect of dose estimations than the monitoring of occupational exposure to external radiation. In the monitoring of occupational exposure to external radiation, individual dosimeter measures the personal dose equivalent, $H_p(10)$ (personal dose equivalent is an operational quantity defined by the ICRU). This measurement is taken as an assessment of the effective dose under the assumption of a uniform whole-body exposure. In contrast, this research has developed dose estimation procedures that can calculate organ/tissue absorbed dose of an ORW when the person exposed to the external radiation. Therefore, by using the developed procedure of dose estimation in occupational exposure to external radiation, organ/tissue-specific dosimetry is possible. Of course, the person-specific effective dose can be calculated from the estimated absorbed doses.

6.3 Conclusion

PHITS based dosimetry is a completely different method of radiation dosimetry from occupational exposure of external source, ^{132}Cs . It can estimate absorbed doses for organs/tissue of ORW rather than dose monitoring methodology without aiding a personal dosimeter. The ORW is a researcher who works with ^{132}Cs contaminated soil samples. This research can explain the radiation protection quantities in terms of the basic physical quantity, absorbed dose. Therefore, results generated by this PHITS-based occupational dose estimation method can apply to predict the critical organ dosimetry in radiation protection purposes.

7. Summary and Future Outlook

7.1 Summary and Conclusions

Radiation absorbed dose estimations for patients undergoing diagnostic examination and/or treatment in nuclear medicine performed via calculations, based on the human body model and the radiopharmaceutical behavior in the body. For patient-specific dosimetry, the dose calculations on an anatomical model depends on the individual physical properties of a patient recommended. A radiopharmaceutical is an entity made up of a radioisotope (RI) which shows a proper choice of RI allows the medical community better access to detail information on the characteristics of the different tumors with minimization of its relative biological effects on the normal organs/tissues. To study the applicability of radiation dose calculation to any administrated RIs aiming at their present or future applications, we developed a unique radiation dosimetry system from RI production to posttreatment of patients in this thesis. The developed PHITS-based dose calculation applied for: (a) the medical RI production by using the double-differential thick-target neutron yield (DDTTNY) of deuteron induced accelerator-based neutrons (b) the organ/tissue absorbed dose coefficient of the RI administrated patient, (c) the ambient dose equivalent, H^* (10), for the area or workplace monitoring by considering an RI administered patient as an external source of radiation after therapy period, and (d) the organ/tissue absorbed dose coefficient of a radiation worker for an occupational exposure from the external radiation source. Our calculation system can apply to any medical RIs. However, we calculated organ/tissue doses for ^{47}Sc -theranostic and ^{132}Cs -environmental tracer for the case study. Moreover, this development can estimate the organs/tissues absorbed doses of the Japanese averages and suggested that our developed method of radiation dosimetry can play an important role in the preclinical dose estimations for the Japanese and the Asian. The measured data from the established dosimetric method may contribute to benchmark the study of treatment planning for the RI administered patient in the nuclear medicine.

The deuteron induced accelerator-based neutron technique is one of the prominent ways to produce RIs. In this thesis, accelerator-based neutrons generated by 12, 20, and 30 MeV deuteron induced reactions on a thick $^{\text{nat}}\text{C}$ ($\varnothing 20$ mm, 4 mm^l). Generated neutrons passed through a vacuum collimator, and they irradiated multiple foils placed on the stage 10 cm downstream from the neutron source. Irradiated multiple foils made of $^{\text{nat}}\text{Ni}$, $^{\text{nat}}\text{In}$, ^{27}Al , ^{59}Co , and ^{93}Nb . Irradiation performed on a multi-layered foil composed of the above metal foils and placed at 0°, 10°, 20°, 30°, and 45° from the deuteron beam direction. The neutron energy spectra were unfolded by GRAVEL code. We compare the resultant DDTNYS with the results of the theoretical calculation code, DEURACS, and showed that the DEURACS calculation underestimates our results in the lower deuteron energy

range with increasing neutron emission energy. Further, other experimental data included, and also the systematics derived to predict the differential neutron yields at 0° and total neutron yield per incident deuteron over the wide range of energy. So, this study provides useful nuclear data of deuteron-induced reactions over a wide range of incident deuteron energy from 12 MeV to 30 MeV for ^{nat}C in the design of deuteron accelerator neutron sources.

For an instant, ^{132}Cs -an alternative tracer of ^{137}Cs , and theranostic nuclide ^{47}Sc can produce by using accelerator neutrons by deuterons. This thesis, at first, a tracer ^{132}Cs production experiment described; which produced by irradiating a 12-g of Cs_2CO_3 sample using accelerator-based neutrons by 30 MeV deuterons. The $^{133}\text{Cs}(n,2n)^{132}\text{Cs}$ reaction, initiated by irradiating 30 MeV deuterons on a thick ^{nat}C ($\varnothing 40$ mm, 4 mm^l), yielded 102.2 kBq/g of ^{132}Cs with a radioactive purity of 98% after irradiation. Next, we conducted a feasibility study of the produced ^{132}Cs . The cesium absorptions to andosol, haplic fluvisol, and gleyic fluvisol soil particles were measured by a NaI (TI) γ -ray detector. Almost 100% of the ^{132}Cs distributed within 40 mm from the surfaces of all soil samples. The results are consistent with earlier studies on ^{137}Cs soil absorption. Therefore, ^{132}Cs can replace ^{137}Cs as an environmental tracer.

The production yields and purities of an emergent theranostic medical RI, ^{47}Sc , is estimated by PHITS simulation. Recently, the use of ^{47}Sc for therapeutic purposes, as part of the $^{43}\text{Sc}/^{47}\text{Sc}$ or $^{44}\text{Sc}/^{47}\text{Sc}$ theranostic radionuclide pair, has attracted considerable attention in nuclear medicine. This thesis estimated the production amount and purities of ^{47}Sc via $^{47}\text{Ti}(n,p)$ route. We have performed feasibility studies to determine the suitability of the $\text{C}(d,n)$ accelerator-based neutrons at 12, 20, and 30 MeV of incident deuteron energy. Radioactivity purity and isotope purity are determined, assuming that 100% of nuclides other than Sc can be purified and separated. The radioactive and isotopic purity of ^{47}Sc was decreased with the increase of the incident deuteron energy because of more impurities were added in ^{47}Sc production. However, enough production amount can be obtained via the accelerator-based neutron method. Based on the results obtained from this proof-of-concept study, ^{47}Sc has the potential to be produced in a suitable quality for clinical applications, however, the quality of radioactivity still needs to be expanded to meet the requirements for radionuclide therapy.

In the next step, this thesis focused on the radiation dosimetric calculations by executing our established PHITS-based dosimetry method described in the first paragraph of this section. However, our developed method of dose estimation has been applied to the absorbed doses to organs/tissues in mGy/MBq and the effective dose coefficient calculation for some emergent medical RI like ^{47}Sc , $^{64,67}\text{Cu}$, ^{90}Y , $^{152,161}\text{Tb}$, ^{166}Ho , etc. with other frequently used RI (e.g., ^{18}F , ^{99m}Tc , $^{123,131}\text{I}$, etc.). Estimated results showed considerable dissimilarities to the ICRP recommended values sometimes. This made the importance of the new PHITS based dose estimations using JM-103 and JF-103.

However, in this thesis, the absorbed dose coefficient in mGy/MBq in different organs/tissues listed for some future prospective medical RIs prominent in nuclear medicine applications concerning their suitability of the uses as radiopharmaceuticals. These dose coefficients would be a guideline for the medical physics researchers rather than clinical reference, especially for the Asian people's body geometry. The ICRP/ICRU reference adults, AM and AF, have different anatomical and physiological characteristics than JM-103 and JF-103, so the results obtained in this thesis would be a reference for internal dosimetry in nuclear medicine for the Asian peoples.

For area or workplace monitoring of external radiation, a new technique is emerging. We applied our developed PHITS-based dosimetry technique for the calculation of an operational quantity called the ambient dose equivalent, $H^*(10)$. It is a unique method of area or workplace monitoring than the conventional method which uses conversion coefficients for the photon. Based on the ICRU definition for $H^*(10)$, we have done this thesis for the $H^*(10)$ calculation by using the PHITS universal source calculation of 'dump' files. Since the technique of universal radiation source calculation can play an important role in medical dosimetry research of clinical nuclear medicine application. So that the calculation results are predictable to the radiation safety issues, for the clinical staff who works in the nuclear medicine department, and the person who will take care of the patient after therapeutic or theranostic application. Meanwhile, this research validated $H^*(10)$ estimation by reading the universal radiation source files when a patient treated by ^{47}Sc -theranostic. Demonstration of the described method of $H^*(10)$ calculation for some theranostic radionuclides (e.g., ^{47}Sc , ^{64}Cu , and $^{64}\text{Cu}/^{67}\text{Cu}$) replies to the successful reading of the created universal radiation source.

Also, PHITS based dosimetry is a unique method of radiation dosimetry from occupational exposure of an external source, ^{132}Cs . It can estimate absorbed dose coefficients for organs/tissue of a reference person rather than the overall dose monitoring by a personal dosimeter. The reference person is a researcher who worked with ^{132}Cs contaminated soil samples. As of practical experience, during dealing with radioactive ^{132}Cs a researcher may expose to external radiation emitted by ^{132}Cs . This successful calculation can explain the radiation protection quantities in terms of the basic physical quantity, absorbed dose.

Finally, the work underlying this thesis has led to the following conclusions:

- The unfolding DDTTNYs can be measured systematically for deuteron bombardment on thick ^{12}C target at incident energies of 12, 20, and 30 MeV by multiple-foils activation method.
- The measured DDTTNYs can reproduce the theoretical calculation with DEURACS for all incident energies quantitatively at emission angles below 45° and suggested that DEURACS can be used for interpolation of the

lacked experimental DDTTNY in the deuteron energy range from 12 to 30 MeV for 0-45° of neutron emission angles.

- An environmental tracer ^{132}Cs production experiment is described; which is produced by irradiating a 12-g of Cs_2CO_3 sample using accelerator-based neutrons by 30 MeV deuterons via $^{133}\text{Cs}(n,2n)^{132}\text{Cs}$ reaction, and yielded 102.2 kBq/g of ^{132}Cs with a radioactive purity of 98% after irradiation.
- The cesium absorptions to andosol, haplic fluvisol, and gleyic fluvisol soil samples were measured by a NaI(Tl) γ -ray detector which concluded that ^{132}Cs can replace ^{137}Cs as an alternative environmental tracer.
- The production yields and purities of ^{47}Sc can be optimized by PHITS simulation which implied that the radioactive and isotopic purity is decreasing while incident deuteron energy is increasing because of more impurity is added in ^{47}Sc production.
- Absorbed dose calculations for a specific radiopharmaceutical in nuclear medicine can be implemented with PHITS-based simulation for more detailed Japanese voxelized reference phantoms, JM-103 and JF-103.
- Effective dose estimations dedicated to intravenous administration of nuclear medicine based on the definitions in ICRP Publication 103 can be performed with the JM-103 and JF-103 and the list of dose coefficients in mGy/MBq for some future prospective medical RIs were estimated using the internal dosimetry method developed in this thesis.
- PHITS-based external dosimetry for $H^*(10)$ can be performed by reading the universal radiation source calculation (i.e., ‘dump’ files) with the information on the transmitted particles from the patient’s body after nuclear medicine application.
- An occupational radiation dose for an external source of ^{132}Cs can be estimated by the absorbed dose to the organs/tissues of an occupational radiation worker by applying PHITS simulation.
- PHITS-based radiation dosimetry can precisely apply with the JM-103 and JF-103 to make radiation dose estimations more user friendly.

7.2 Suggestions for Future Work

In the future, three works are expected. First, the systematic measurements are necessary by using other promising neutron production reactions such as $^9\text{Be}(d,n)$ reactions. In the present research, a method for obtaining neutron data from the neutron-activation analysis, based on comparative measurements, was used to investigate the effect of an increase of deuteron energy on neutron generation in a converter target like $^{\text{nat}}\text{C}$. For both targets, we will perform measurements of the DDTNYS in the range from 12 MeV to 50 MeV to know the systematics. For further validation of the unfolding codes (GRAVEL), we will conduct measurements by the other method (e.g. MAXED [38], RooUnfold [39], and the ANN code [40]) to obtain DDTNYS. Therefore, systematic analysis of the DDTNYS with the many thick targets and the unfolding code can extend our findings to other RI productions.

Second, we will apply the ^{132}Cs product to cesium dynamics in different soil samples in the environment. This work will contribute to the environmental recovery near the Fukushima Dai-ichi Nuclear Power Plant accident. Additionally, we plan to measure the Cs transition from soils to plants using the ^{132}Cs tracer concept. We will further investigate the Cs dynamics in living organisms, providing valuable and much-needed data for understanding Cs dynamics in humans.

Finally, absorbed dose calculations for a specific radiopharmaceutical in diagnostic and/or therapeutic or theranostic nuclear medicine can be automated for more detailed Japanese voxelized reference phantoms, JM-103 and JF-103. The implementation of these phantoms into nuclear medicine will be much less time consuming using the framework presented in this thesis. Moreover, the small risk to later in life develop radiation-induced cancer from a radiopharmaceutical is currently estimated using the quantity, called the effective dose. The radiation weighting factors used to estimate the effective dose is set to 1 for photons and electrons from radionuclides in diagnostic nuclear medicine. However, for Auger electron emitters (e.g., ^{51}Cr , ^{67}Ga , $^{99\text{m}}\text{Tc}$, ^{111}In , etc.), ICRP confesses that a larger w_R maybe appropriate, even if no specific value is recommended. Humm *et al.* (1994) [212] recognized that DNA incorporated radionuclides emitting Auger electrons have a similar effect as α -particles and recommends a radiation weighting factor of 20 for stochastic effects. These factors are hence given for subcellular distributions, which is taken into account may have an impact on the effective dose. The subcellular distribution and microdosimetry could be of high importance for risk estimations. There is also a need to improve the estimation of stochastic effects for various population groups. One reason for this is the sex, age, and population unspecific nature of the effective dose protection unit [46]. It is questionable how well the data of the life span study applies to the exposure situations in theranostic nuclear medicine. The current risk estimates assume a linear no-threshold dose/risk model and a dose and dose rate effectiveness factor. Epidemiological studies based on dose data generated today and during the next decades are needed to improve

risk estimations for stochastic effects. Besides, an interesting future possibility is complete and automated segmentation of organs and structures in the CT- or MR-images from each patient. This will facilitate individual absorbed dose estimations and might, combined with a dose tracking system, generate sufficient epidemiological data for more accurate predictions of stochastic effects.

References

- [1] C. Woodford and P. Ashby, "Non-Destructive Testing and Radiation in Industry On behalf of the Australian Institute for Non-Destructive Testing."
- [2] B. Singh, J. Singh, and A. Kaur, "Applications of Radioisotopes in Agriculture," *Int. J. Biotechnol. Bioeng. Res.*, vol. 4, no. 3, pp. 167–174, 2013, [Online]. Available: <http://www.ripublication.com/ijbbr.htm>.
- [3] M. F. Patterson, "Food irradiation and food safety," *Rev. Med. Microbiol.*, vol. 4, no. 3, pp. 151–158, Jul. 1993, doi: 10.1097/00013542-199307000-00005.
- [4] G. Stöcklin, S. M. Qaim, and F. Rösch, "The Impact of Radioactivity on Medicine Metallic," *Radiochim. Acta*, vol. 70–71, no. s1, Jan. 1995, doi: 10.1524/ract.1995.7071.special-issue.249.
- [5] J. Krige, "Atoms for Peace, Scientific Internationalism, and Scientific Intelligence," *Osiris*, vol. 21, no. 1, pp. 161–181, Jan. 2006, doi: 10.1086/507140.
- [6] "JEMIMA Japan Electric Measuring Instruments Manufacturers' Association." <https://www.jemima.or.jp/en/index.html> (accessed Jun. 06, 2020).
- [7] IAEA, "Irradiation of bulbs and tuber crops," IAEA-TECDOC-937, IAEA, Vienna, Austria, p. 101, 1997.
- [8] S. Banerjee, M. R. Ambikalmajan Pillai, and N. Ramamoorthy, "Evolution of Tc-99m in diagnostic radiopharmaceuticals," *Semin. Nucl. Med.*, vol. 31, no. 4, pp. 260–277, Oct. 2001, doi: 10.1053/snuc.2001.26205.
- [9] A. Wyszomirska, "Iodine-131 for therapy of thyroid diseases. Physical and biological basis," *Nuclear Medicine Review*, vol. 15, no. 2, pp. 120–123, 2012.
- [10] J. J. P. De Lima, "Radioisotopes in medicine," *Eur. J. Phys.*, vol. 19, no. 6, pp. 485–497, 1998, doi: 10.1088/0143-0807/19/6/003.
- [11] D. Nayak and S. Lahiri, "Application of radioisotopes in the field of nuclear medicine," *J. Radioanal. Nucl. Chem.*, vol. 242, no. 2, pp. 423–432, Nov. 1999, doi: 10.1007/BF02345573.
- [12] "Enrico Fermi - Nobel Lecture: Artificial Radioactivity Produced by Neutron Bombardment." <https://www.nobelprize.org/prizes/physics/1938/fermi/lecture/> (accessed Jun. 06, 2020).
- [13] Y. Nagai *et al.*, "Generation of Radioisotopes with Accelerator Neutrons by

- Deuterons,” *J. Phys. Soc. Japan*, vol. 82, no. 6, p. 064201, Jun. 2013, doi: 10.7566/JPSJ.82.064201.
- [14] E. Musacchio González and G. Martín Hernández, “An accelerator-based Boron Neutron Capture Therapy (BNCT) facility based on the ${}^7\text{Li}(p,n){}^7\text{Be}$,” *Nucl. Instruments Methods Phys. Res. Sect. A Accel. Spectrometers, Detect. Assoc. Equip.*, vol. 865, pp. 148–151, Sep. 2017, doi: 10.1016/j.nima.2016.11.059.
 - [15] G. Yue, J. Chen, and R. Song, “Study of boron neutron capture therapy used neutron source with protons bombarding a thick ${}^9\text{Be}$ target,” *Med. Phys.*, vol. 24, no. 6, pp. 851–855, Jun. 1997, doi: 10.1118/1.597984.
 - [16] S. Kawase *et al.*, “Study of proton- and deuteron-induced spallation reactions on the long-lived fission product ${}^{93}\text{Zr}$ at 105 MeV/nucleon in inverse kinematics,” *Prog. Theor. Exp. Phys.*, vol. 2017, no. 9, Sep. 2017, doi: 10.1093/ptep/ptx110.
 - [17] J. Hartman and A. Barzilov, “DD and DT neutron generator yield measurements using EJ-299-33A detector,” in *2015 IEEE Nuclear Science Symposium and Medical Imaging Conference, NSS/MIC 2015*, Oct. 2016, pp. 1–4, doi: 10.1109/NSSMIC.2015.7581918.
 - [18] T. Kin, T. Kawagoe, S. Araki, and Y. Watanabe, “Production of high-purity medical radio isotope ${}^{64}\text{Cu}$ with accelerator-based neutrons generated with 9 and 12 MeV deuterons,” *J. Nucl. Sci. Technol.*, vol. 54, no. 10, pp. 1123–1130, Oct. 2017, doi: 10.1080/00223131.2017.1344585.
 - [19] T. Kin *et al.*, “New Production Routes for Medical Isotopes ${}^{64}\text{Cu}$ and ${}^{67}\text{Cu}$ Using Accelerator Neutrons,” *J. Phys. Soc. Japan*, vol. 82, no. 3, p. 034201, Mar. 2013, doi: 10.7566/JPSJ.82.034201.
 - [20] T. Kin *et al.*, “Development of Radioisotopes Production Method by Accelerator-Based Neutron: Activity at Kyushu University,” in *Proceedings of the Second International Symposium on Radiation Detectors and Their Uses (ISR2018)*, Jan. 2019, doi: 10.7566/jpscp.24.011031.
 - [21] T. Kin, Y. Sanzen, M. Kamida, Y. Watanabe, and M. Itoh, “Production of ${}^{92}\text{Y}$ via the ${}^{92}\text{Zr}(n,p)$ reaction using the $\text{C}(d,n)$ accelerator neutron source,” *EPJ Web Conf.*, vol. 146, p. 08009, Sep. 2017, doi: 10.1051/epjconf/201714608009.
 - [22] F. Minato and Y. Nagai, “Estimation of production yield of ${}^{99}\text{Mo}$ for medical use using neutrons from $\text{natC}(d,n)$ at $E_d = 40\text{MeV}$,” *J. Phys. Soc. Japan*, vol. 79, no. 9, p. 093201, Sep. 2010, doi: 10.1143/JPSJ.79.093201.
 - [23] Y. Nagai, “Medical isotope production using accelerator neutrons,” in *11th International Topical Meeting on Nuclear Applications of Accelerators, AccApp 2013*, 2013, pp. 47–49.

- [24] Y. Nagai and Y. Hatsukawa, “Production of ^{99}Mo for Nuclear Medicine by $^{100}\text{Mo}(n,2n)^{99}\text{Mo}$,” *J. Phys. Soc. Japan*, vol. 78, no. 3, p. 033201, Mar. 2009, doi: 10.1143/JPSJ.78.033201.
- [25] Y. Nagai *et al.*, “Production of an Isomeric State of ^{90}Y by Fast Neutrons for Nuclear Diagnostics,” *J. Phys. Soc. Japan*, vol. 78, no. 11, p. 113201, Nov. 2009, doi: 10.1143/jpsj.78.113201.
- [26] Y. Nagai, H. Makii, S. Namiki, O. Iwamoto, N. Iwamoto, and H. Sawahata, “Radioactive tracer ^{132}Cs (TRACs) for Fukushima nuclear power plant accident,” *J. Phys. Soc. Japan*, vol. 81, no. 8, p. 085003, Aug. 2012, doi: 10.1143/JPSJ.81.085003.
- [27] M. J. Saltmarsh, C. A. Ludemann, C. B. Fulmer, and R. C. Styles, “Characteristics of an intense neutron source based on the d+Be reaction,” *Nucl. Instruments Methods*, vol. 145, no. 1, pp. 81–90, Aug. 1977, doi: 10.1016/0029-554X(77)90559-6.
- [28] Y. Uwamino, T. Ohkubo, A. Torii, and T. Nakamura, “Semi-monoenergetic neutron field for activation experiments up to 40 MeV,” *Nucl. Inst. Methods Phys. Res. A*, vol. 271, no. 3, pp. 546–552, Sep. 1988, doi: 10.1016/0168-9002(88)90318-X.
- [29] EXFOR, “Experimental nuclear reaction data file,” *Energy Sci. Technol. Dept., BNL*, 2011, Accessed: Jun. 06, 2020. [Online]. Available: <https://www-nds.iaea.org/exfor/>.
- [30] S. Araki, “Study on secondary neutron and gamma-ray production from deuteron-induced nuclear reactions (Japanese),” Kyushu University, 2017.
- [31] J. P. Meulders, P. Leleux, P. C. Macq, and C. Pirart, “Fast neutron yields and spectra from targets of varying atomic number bombarded with deuterons from 16 to 50 MeV,” *Phys. Med. Biol.*, vol. 20, no. 2, pp. 235–43, Mar. 1975, doi: 10.1088/0031-9155/20/2/005.
- [32] T. Sato *et al.*, “Features of Particle and Heavy Ion Transport code System (PHITS) version 3.02,” *J. Nucl. Sci. Technol.*, vol. 55, no. 6, pp. 684–690, Jun. 2018, doi: 10.1080/00223131.2017.1419890.
- [33] T. Goorley *et al.*, “Features of MCNP6,” *Ann. Nucl. Energy*, vol. 87, pp. 772–783, Jan. 2016, doi: 10.1016/j.anucene.2015.02.020.
- [34] S. Agostinelli *et al.*, “GEANT4 - A simulation toolkit,” *Nucl. Instruments Methods Phys. Res. Sect. A Accel. Spectrometers, Detect. Assoc. Equip.*, vol. 506, no. 3, pp. 250–303, Jul. 2003, doi: 10.1016/S0168-9002(03)01368-8.
- [35] S. Nakayama, H. Kouno, Y. Watanabe, O. Iwamoto, and K. Ogata, “Theoretical model analysis of (d,xn) reactions on ^9Be and ^{12}C at incident energies up to 50 MeV,” *Phys. Rev. C*, vol. 94, no. 1, p. 014618, Jul. 2016,

doi: 10.1103/PhysRevC.94.014618.

- [36] Glenn G. Knoll, *Radiation Detection and Measurement (4th Edition)*, vol., no. John Wiley and Sons, Inc., 2010.
- [37] M. Matzke, “Unfolding of Pulse Height Spectra: The HEPRO Program,” *Phys. Tech. Bundesanstalt*, vol. 19, 1994.
- [38] M. Reginatto, “The ‘Multi-Channel’ Unfolding Programs in the UMG Package: MXD_MC33, GRV_MC33 and IQU_MC33,” Braunschweig, Germany, 2004. [Online]. Available: <http://www.tokai.rist.or.jp/rsicc/app/umg3.3.htm>.
- [39] T. Adye, “Unfolding algorithms and tests using RooUnfold,” in *Proceedings of the PHYSTAT 2011 Workshop on Statistical Issues Related to Discovery Claims in Search Experiments and Unfolding*, May 2011, pp. 313–318, [Online]. Available: <http://arxiv.org/abs/1105.1160>.
- [40] T. Kin, Y. Sanzen, M. Kamida, K. Aoki, N. Araki, and Y. Watanabe, “Artificial Neural Network for Unfolding Accelerator-based Neutron Spectrum by Means of Multiple-foil Activation Method,” in *2017 IEEE Nuclear Science Symposium and Medical Imaging Conference (NSS/MIC)*, Oct. 2017, pp. 1–2, doi: 10.1109/NSSMIC.2017.8532892.
- [41] ICRP, 1996. “Conversion Coefficients for use in Radiological Protection against External Radiation,” *ICRP Publication 74. Ann. ICRP 26 (3-4)*.
- [42] ICRP, 1975. “Report of the Task Group on Reference Man,” ICRP Publication 23 Pergamon Press, Oxford.
- [43] ICRP, 2002. “Basic Anatomical and Physiological Data for Use in Radiological Protection Reference Values,” *ICRP Publication 89. Ann. ICRP 32 (3-4)*.
- [44] ICRP, 2009. “Adult Reference Computational Phantoms,” *ICRP Publication 110. Ann. ICRP 39 (2)*.
- [45] M. Zankl and A. Wittmann, “The adult male voxel model ”Golem” segmented from whole-body CT patient data,” *Radiat. Environ. Biophys.*, vol. 40, no. 2, pp. 153–162, Jun. 2001, doi: 10.1007/s004110100094.
- [46] ICRP, 2007. “The 2007 Recommendations of the International Commission on Radiological Protection,” *ICRP Publication 103. Ann. ICRP 37 (2-4)*.
- [47] K. Sato and F. Takahashi, “The contemporary JAEA Japanese voxel phantoms,” *Radiat. Prot. Dosimetry*, vol. 149, no. 1, pp. 43–48, Mar. 2012, doi: 10.1093/rpd/ncr405.
- [48] G. Tanaka, H. Kawamura, R. V. Griffith, M. Cristy, and K. F. Eckerman, “Reference Man Models for Males and Females of Six Age Groups of Asian

- Populations,” *Radiat. Prot. Dosimetry*, vol. 79, no. 1, pp. 383–386, Oct. 1998, doi: 10.1093/oxfordjournals.rpd.a032432.
- [49] J. Knaster *et al.*, “Overview of the IFMIF/EVEDA project,” *Nucl. Fusion*, vol. 57, no. 10, p. 102016, Oct. 2017, doi: 10.1088/1741-4326/aa6a6a.
- [50] M. Fadil and B. Rannou, “About the production rates and the activation of the uranium carbide target for SPIRAL 2,” *Nucl. Instruments Methods Phys. Res. Sect. B Beam Interact. with Mater. Atoms*, vol. 266, no. 19–20, pp. 4318–4321, Oct. 2008, doi: 10.1016/j.nimb.2008.05.138.
- [51] N. Colonna *et al.*, “Measurements of low-energy (d,n) reactions for BNCT,” *Med. Phys.*, vol. 26, no. 5, pp. 793–798, 1999, doi: 10.1118/1.598599.
- [52] H. Tanaka *et al.*, “Characteristics comparison between a cyclotron-based neutron source and KUR-HWNIF for boron neutron capture therapy,” *Nucl. Instruments Methods Phys. Res. Sect. B Beam Interact. with Mater. Atoms*, vol. 267, no. 11, pp. 1970–1977, Jun. 2009, doi: 10.1016/j.nimb.2009.03.095.
- [53] “Research reactors and Accelerators / Japan Atomic Energy Agency / Nuclear Science Research Institute.” https://www.jaea.go.jp/english/04/ntokai/kasokuki/kasokuki_04.html (accessed Jun. 06, 2020).
- [54] “Ignite the Future of High-Tech R&D | The Nilaco Corporation.” <https://nilaco.jp/en/> (accessed Jun. 06, 2020).
- [55] J. F. Ziegler, M. D. Ziegler, and J. P. Biersack, “SRIM – The stopping and range of ions in matter (2010),” *Nucl. Instruments Methods Phys. Res. Sect. B Beam Interact. with Mater. Atoms*, vol. 268, no. 11–12, pp. 1818–1823, Jun. 2010, doi: 10.1016/j.nimb.2010.02.091.
- [56] “Nudat 2.” 2018, Accessed: Jun. 06, 2020. [Online]. Available: <https://www.nndc.bnl.gov/nudat2/>.
- [57] G. R. Gilmore, *Practical Gamma-Ray Spectrometry*. Chichester, UK: John Wiley & Sons, Ltd, 2008.
- [58] J.-C. Sublet, “The European Activation File: EAF-2010 neutron-induced cross-section library,” Oxfordshire, OX14 3DB, United Kingdom, 2010. [Online]. Available: https://tendl.web.psi.ch/bib_rochman/EAF2010.pdf.
- [59] A. Sonzogni and B. Pritychenko, “Q-value Calculator (QCalc),” *NNDC, Brookhaven National Laboratory*, 2003. <https://www.nndc.bnl.gov/qcalc/> (accessed Jun. 06, 2020).
- [60] V. Suman and P. K. Sarkar, “Neutron spectrum unfolding using genetic algorithm in a Monte Carlo simulation,” *Nucl. Instruments Methods Phys. Res. Sect. A Accel. Spectrometers, Detect. Assoc. Equip.*, vol. 737, pp. 76–

86, Feb. 2014, doi: 10.1016/j.nima.2013.11.012.

- [61] K. A. Weaver, J. D. Anderson, H. H. Barschall, and J. C. Davis, “Neutron Spectra from Deuteron Bombardment of D, Li, Be, and C,” *Nucl. Sci. Eng.*, vol. 52, no. 1, pp. 35–45, Sep. 1973, doi: 10.13182/NSE73-A23287.
- [62] K. Shin, K. Hibi, M. Fujii, Y. Uwamino, and T. Nakamura, “Neutron and photon production from thick targets bombarded by 30-MeV p, 33-MeV d, 65-MeV He3, and 65-MeV ions: Experiment and comparison with cascade Monte Carlo calculations,” *Phys. Rev. C*, vol. 29, no. 4, pp. 1307–1316, 1984, doi: 10.1103/PhysRevC.29.1307.
- [63] Y. Tajiri, Y. Watanabe, N. Shigyo, K. Hirabayashi, T. Nishizawa, and K. Sagara, “Measurement of double differential neutron yields from thick carbon target irradiated by 5-MeV and 9-MeV deuterons,” *Prog. Nucl. Sci. Technol.*, vol. 4, pp. 582–586, 2014, doi: 10.15669/pnst.4.582.
- [64] G. Lhersonneau *et al.*, “Neutron yield from carbon, light- and heavy-water thick targets irradiated by 40MeV deuterons,” *Nucl. Instruments Methods Phys. Res. Sect. A Accel. Spectrometers, Detect. Assoc. Equip.*, vol. 603, no. 3, pp. 228–235, May 2009, doi: 10.1016/j.nima.2009.02.035.
- [65] V. N. Kononov, M. V. Bokhovko, O. E. Kononov, N. A. Soloviev, W. T. Chu, and D. Nigg, “Accelerator-based fast neutron sources for neutron therapy,” *Nucl. Instruments Methods Phys. Res. Sect. A Accel. Spectrometers, Detect. Assoc. Equip.*, vol. 564, no. 1, pp. 525–531, Aug. 2006, doi: 10.1016/j.nima.2006.03.043.
- [66] M. Hagiwara *et al.*, “Experimental studies on the neutron emission spectrum and activation cross-section for 40 MeV deuterons in IFMIF accelerator structural elements,” *J. Nucl. Mater.*, vol. 329–333, pp. 218–222, Aug. 2004, doi: 10.1016/j.jnucmat.2004.04.026.
- [67] Z. Radivojevic *et al.*, “Neutron yields from thick ^{12}C and ^9Be targets irradiated by 50 and 65 MeV deuterons,” *Nucl. Instruments Methods Phys. Res. Sect. B Beam Interact. with Mater. Atoms*, vol. 183, no. 3–4, pp. 212–220, Oct. 2001, doi: 10.1016/S0168-583X(01)00729-7.
- [68] G. W. Schweimer, “Fast neutron production with 54 MeV deuterons,” *Nucl. Phys. A*, vol. 100, no. 3, pp. 537–544, Aug. 1967, doi: 10.1016/0375-9474(67)90122-4.
- [69] G. Lhersonneau *et al.*, “Neutron yield of thick ^{12}C and ^{13}C targets with 20 and 30 MeV deuterons,” *Eur. Phys. J. A*, vol. 52, no. 12, p. 364, Dec. 2016, doi: 10.1140/epja/i2016-16364-x.
- [70] G. Lhersonneau, T. Malkiewicz, P. Jones, S. Ketelhut, and W. H. Trzaska, “Neutron production by stopping 55 MeV deuterons in carbon and heavy water,” *Eur. Phys. J. A*, vol. 48, no. 9, p. 116, Sep. 2012, doi:

10.1140/epja/i2012-12116-4.

- [71] S. Ménard *et al.*, “Fast neutron forward distributions from C, Be, and U thick targets bombarded by deuterons,” *Phys. Rev. Spec. Top. - Accel. Beams*, vol. 2, no. 3, p. 033501, Mar. 1999, doi: 10.1103/PhysRevSTAB.2.033501.
- [72] N. Pauwels, F. Clapier, P. Gara, M. Mirea, and J. Proust, “Experimental determination of neutron spectra produced by bombarding thick targets: Deuterons (100 MeV/u) on ^9Be , deuterons (100 MeV/u) on ^{238}U and ^{36}Ar (95 MeV/u) on ^{12}C ,” *Nucl. Instruments Methods Phys. Res. Sect. B Beam Interact. with Mater. Atoms*, vol. 160, no. 3, pp. 315–327, Mar. 2000, doi: 10.1016/S0168-583X(99)00605-9.
- [73] T. J. Yasunari, A. Stohl, R. S. Hayano, J. F. Burkhart, S. Eckhardt, and T. Yasunari, “Cesium-137 deposition and contamination of Japanese soils due to the Fukushima nuclear accident,” *Proc. Natl. Acad. Sci.*, vol. 108, no. 49, pp. 19530–19534, Dec. 2011, doi: 10.1073/pnas.1112058108.
- [74] K. Adachi, M. Kajino, Y. Zaizen, and Y. Igarashi, “Emission of spherical cesium-bearing particles from an early stage of the Fukushima nuclear accident,” *Sci. Rep.*, vol. 3, no. 1, p. 2554, Dec. 2013, doi: 10.1038/srep02554.
- [75] Y. Onda, H. Kato, M. Hoshi, Y. Takahashi, and M.-L. Nguyen, “Soil sampling and analytical strategies for mapping fallout in nuclear emergencies based on the Fukushima Dai-ichi Nuclear Power Plant accident,” *J. Environ. Radioact.*, vol. 139, pp. 300–307, Jan. 2015, doi: 10.1016/j.jenvrad.2014.06.002.
- [76] H. Kato, Y. Onda, and T. Gomi, “Interception of the Fukushima reactor accident-derived ^{137}Cs , ^{134}Cs and ^{131}I by coniferous forest canopies,” *Geophys. Res. Lett.*, vol. 39, no. 20, p. 2012GL052928, Oct. 2012, doi: 10.1029/2012GL052928.
- [77] H. Kato, Y. Onda, and M. Teramage, “Depth distribution of ^{137}Cs , ^{134}Cs , and ^{131}I in soil profile after Fukushima Dai-ichi Nuclear Power Plant Accident,” *J. Environ. Radioact.*, vol. 111, pp. 59–64, Sep. 2012, doi: 10.1016/j.jenvrad.2011.10.003.
- [78] S. Hashimoto, T. Matsuura, K. Nanko, I. Linkov, G. Shaw, and S. Kaneko, “Predicted spatio-temporal dynamics of radiocesium deposited onto forests following the Fukushima nuclear accident,” *Sci. Rep.*, vol. 3, no. 1, p. 2564, Dec. 2013, doi: 10.1038/srep02564.
- [79] A. Konoplev *et al.*, “Behavior of accidentally released radiocesium in soil–water environment: Looking at Fukushima from a Chernobyl perspective,” *J. Environ. Radioact.*, vol. 151, pp. 568–578, Jan. 2016, doi: 10.1016/j.jenvrad.2015.06.019.
- [80] E. Browne and J. K. Tuli, “Nuclear Data Sheets for $A = 137$,” *Nucl. Data*

- Sheets*, vol. 108, no. 10, pp. 2173–2318, Oct. 2007, doi: 10.1016/j.nds.2007.09.002.
- [81] T. Iinuma, T. Nagai, T. Ishihara, K. Watari, and M. Izawa, “Cesium Turnover in Man following Single Administration of ^{132}Cs 1. Whole Body Retention and Excretion Pattern,” *J. Radiat. Res.*, vol. 6, no. 2, pp. 73–81, 1965, doi: 10.1269/jrr.6.73.
 - [82] J. S. McKee *et al.*, “Dynamic studies of positron-emitting putative tumor marker ^{132}Cs in mice show differential tumor and regional uptake,” *Cancer Detect. Prev.*, vol. 8, no. 1–2, pp. 87–93, 1985.
 - [83] “Cyclotron and Radioisotope Center (CYRIC).” <http://www.cyric.tohoku.ac.jp/english/index.html> (accessed Jun. 06, 2020).
 - [84] T. Wakui, M. Itoh, K. Shimada, H. P. Yoshida, T. Shinozuka, and Y. Sakemi, “Restoration of Accelerator Facilities Damaged by Great East Japan Earthquake at Cyclotron and Radioisotope Center, Tohoku University,” *Tohoku J. Exp. Med.*, vol. 233, no. 4, pp. 221–231, 2014, doi: 10.1620/tjem.233.221.
 - [85] A. V. Konoplev *et al.*, “Vertical distribution of radiocesium in soils of the area affected by the Fukushima Dai-ichi nuclear power plant accident,” *Eurasian Soil Sci.*, vol. 49, no. 5, pp. 570–580, May 2016, doi: 10.1134/S1064229316050082.
 - [86] S. Ootosaka, T. Nakanishi, T. Suzuki, Y. Satoh, and H. Narita, “Vertical and Lateral Transport of Particulate Radiocesium off Fukushima,” *Environ. Sci. Technol.*, vol. 48, no. 21, pp. 12595–12602, Nov. 2014, doi: 10.1021/es503736d.
 - [87] M. T. Teramage, Y. Onda, J. Patin, H. Kato, T. Gomi, and S. Nam, “Vertical distribution of radiocesium in coniferous forest soil after the Fukushima nuclear power plant accident,” *J. Environ. Radioact.*, vol. 137, pp. 37–45, Nov. 2014, doi: 10.1016/j.jenvrad.2014.06.017.
 - [88] K. Fujii, S. Ikeda, A. Akama, M. Komatsu, M. Takahashi, and S. Kaneko, “Vertical migration of radiocesium and clay mineral composition in five forest soils contaminated by the Fukushima nuclear accident,” *Soil Sci. Plant Nutr.*, vol. 60, no. 6, pp. 751–764, Nov. 2014, doi: 10.1080/00380768.2014.926781.
 - [89] J. Koarashi, M. Atarashi-Andoh, T. Matsunaga, T. Sato, S. Nagao, and H. Nagai, “Factors affecting vertical distribution of Fukushima accident-derived radiocesium in soil under different land-use conditions,” *Sci. Total Environ.*, vol. 431, pp. 392–401, Aug. 2012, doi: 10.1016/j.scitotenv.2012.05.041.
 - [90] T. Ohno *et al.*, “Depth profiles of radioactive cesium and iodine released from the Fukushima Daiichi nuclear power plant in different agricultural

- fields and forests,” *Geochem. J.*, vol. 46, no. 4, pp. 287–295, 2012, doi: 10.2343/geochemj.2.0204.
- [91] K. Tanaka *et al.*, “Vertical profiles of Iodine-131 and Cesium-137 in soils in Fukushima Prefecture related to the Fukushima Daiichi Nuclear Power Station Accident,” *Geochem. J.*, vol. 46, no. 1, pp. 73–76, 2012, doi: 10.2343/geochemj.1.0137.
- [92] K. Rosén, I. Öborn, and H. Lönsjö, “Migration of radiocaesium in Swedish soil profiles after the Chernobyl accident, 1987–1995,” *J. Environ. Radioact.*, vol. 46, no. 1, pp. 45–66, Oct. 1999, doi: 10.1016/S0265-931X(99)00040-5.
- [93] Md Kawchar Ahmed Patwary *et al.*, “Feasibility Study of Radioisotope ^{132}Cs Production Using Accelerator-Based Neutrons,” *Evergreen*, vol. 6, no. 4, pp. 280–284, Dec. 2019, doi: 10.5109/2547352.
- [94] K. Hashimoto and Y. Nagai, “Radionuclide Production,” in *Comprehensive Biomedical Physics*, vol. 8, Elsevier, 2014, pp. 219–227.
- [95] S. M. Qaim, “Nuclear data for medical radionuclides,” *J. Radioanal. Nucl. Chem.*, vol. 305, no. 1, pp. 233–245, Jul. 2015, doi: 10.1007/s10967-014-3923-2.
- [96] K. A. Domnanich *et al.*, “ ^{47}Sc as useful β^- -emitter for the radiotheragnostic paradigm: a comparative study of feasible production routes,” *EJNMMI Radiopharm. Chem.*, vol. 2, no. 1, p. 5, Dec. 2017, doi: 10.1186/s41181-017-0024-x.
- [97] C. Müller, K. A. Domnanich, C. A. Umbricht, and N. P. van der Meulen, “Scandium and terbium radionuclides for radiotheragnostics: current state of development towards clinical application,” *Br. J. Radiol.*, vol. 91, no. 1091, p. 20180074, Nov. 2018, doi: 10.1259/bjr.20180074.
- [98] B. Bartoś, A. Majkowska, S. Krajewski, and A. Bilewicz, “New separation method of no-carrier-added ^{47}Sc from titanium targets,” *Radiochim. Acta*, vol. 100, no. 7, pp. 457–462, Jul. 2012, doi: 10.1524/ract.2012.1938.
- [99] C. Muller *et al.*, “Promising Prospects for ^{44}Sc -/ ^{47}Sc -Based Theragnostics: Application of ^{47}Sc for Radionuclide Tumor Therapy in Mice,” *J. Nucl. Med.*, vol. 55, no. 10, pp. 1658–1664, Oct. 2014, doi: 10.2967/jnumed.114.141614.
- [100] C. Loveless, T. Carzaniga, J. Blanco, *et al.*, “Evaluation of cyclotron produced $^{43,44,47}\text{Sc}$ from titanium(0) and titanium oxide,” *J. Label. Compd. Radiopharm.*, vol. 62, pp. S123–S588, May 2019, doi: 10.1002/jlcr.3725.
- [101] S. C. Srivastava, “Paving the way to personalized medicine: production of some theragnostic radionuclides at Brookhaven National Laboratory,” *Radiochim. Acta*, vol. 99, no. 10, pp. 635–640, Oct. 2011, doi: 10.1524/ract.2011.1882.

- [102] M. Yagi and K. Kondo, "Preparation of carrier-free ^{47}Sc by the $^{48}\text{Ti}(\gamma, p)$ reaction," *Int. J. Appl. Radiat. Isot.*, vol. 28, no. 5, pp. 463–468, May 1977, doi: 10.1016/0020-708X(77)90178-8.
- [103] M. Mamtimin, F. Harmon, and V. N. Starovoitova, "Sc-47 production from titanium targets using electron linacs," *Appl. Radiat. Isot.*, vol. 102, pp. 1–4, Aug. 2015, doi: 10.1016/j.apradiso.2015.04.012.
- [104] S. Rane, J. T. Harris, and V. N. Starovoitova, " ^{47}Ca production for $^{47}\text{Ca}/^{47}\text{Sc}$ generator system using electron linacs," *Appl. Radiat. Isot.*, vol. 97, pp. 188–192, Mar. 2015, doi: 10.1016/j.apradiso.2014.12.020.
- [105] V. N. Starovoitova, P. L. Cole, and T. L. Grimm, "Accelerator-based photoproduction of promising beta-emitters ^{67}Cu and ^{47}Sc ," *J. Radioanal. Nucl. Chem.*, vol. 305, no. 1, pp. 127–132, Jul. 2015, doi: 10.1007/s10967-015-4039-z.
- [106] C. S. Loveless, L. L. Radford, S. J. Ferran, S. L. Queern, M. R. Shepherd, and S. E. Lapi, "Photonuclear production, chemistry, and in vitro evaluation of the theranostic radionuclide ^{47}Sc ," *EJNMMI Res.*, vol. 9, no. 1, p. 42, Dec. 2019, doi: 10.1186/s13550-019-0515-8.
- [107] S. M. Qaim, "Nuclear data for production and medical application of radionuclides: Present status and future needs," *Nucl. Med. Biol.*, vol. 44, pp. 31–49, Jan. 2017, doi: 10.1016/j.nucmedbio.2016.08.016.
- [108] T. Shimizu, H. Sakane, M. Shibata, K. Kawade, and T. Nishitani, "Measurements of activation cross sections of (n, p) and (n, α) reactions with d-D neutrons in the energy range of 2.1–3.1 MeV," *Ann. Nucl. Energy*, vol. 31, no. 9, pp. 975–990, Jun. 2004, doi: 10.1016/j.anucene.2003.12.005.
- [109] Y. Ikeda *et al.*, "Activation Cross Section Measurement at Neutron Energies of 9.5, 11.0, 12.0 and 13.2 MeV Using $^1\text{H}(^{11}\text{B}, n)^{11}\text{C}$ Neutron Source at JAERI," 1992, pp. 294–296.
- [110] S. M. Qaim, N. I. Molla, R. Wölflé, and G. Stöcklin, "Differential and Integral Cross Section Measurements of some $(n, \text{charged particle})$ Reactions on Titanium," 1992, pp. 297–300.
- [111] M. Viennot, M. Berrada, G. Paic, and S. Joly, "Cross-Section Measurements of (n, p) and $(n, np + pn + d)$ Reactions for Some Titanium, Chromium, Iron, Cobalt, Nickel, and Zinc Isotopes around 14 MeV," *Nucl. Sci. Eng.*, vol. 108, no. 3, pp. 289–301, Jul. 1991, doi: 10.13182/NSE87-157.
- [112] J. W. M. W. Mannhart, D.L. Smith, "Measurement of the $\text{Ti-47}(n, p)\text{Sc-47}$ reaction cross section (NEANDC-259-U)," *Nucl. Energy Agency OECD*, 1990, [Online]. Available: https://inis.iaea.org/search/search.aspx?orig_q=RN:21092355.

- [113] W. V. Hecker, J. R. Williams, W. L. Alford, and S. K. Ghorai, "Partial neutron cross sections for ^{47}Ti and ^{48}Ti between 14.3 and 19.1 MeV," *Nucl. Instruments Methods Phys. Res. Sect. B Beam Interact. with Mater. Atoms*, vol. 40–41, pp. 478–480, Apr. 1989, doi: 10.1016/0168-583X(89)91025-2.
- [114] H. L. Pai, "The (n,p) Cross sections of Titanium Isotopes for Neutron Energies between 13.6 MeV and 19.5 MeV," *Can. J. Phys.*, vol. 44, no. 10, pp. 2337–2352, Oct. 1966, doi: 10.1139/p66-191.
- [115] K. L. Kolsky, V. Joshi, L. F. Mausner, and S. C. Srivastava, "Radiochemical purification of no-carrier-added scandium-47 for radioimmunotherapy," *Appl. Radiat. Isot.*, vol. 49, no. 12, pp. 1541–1549, Dec. 1998, doi: 10.1016/S0969-8043(98)00016-5.
- [116] A. Boiardi *et al.*, "Intratumoral delivery of mitoxantrone in association with 90-Y radioimmunotherapy (RIT) in recurrent glioblastoma," *J. Neurooncol.*, vol. 72, no. 2, pp. 125–131, Apr. 2005, doi: 10.1007/s11060-004-1497-5.
- [117] M. Luster *et al.*, "Guidelines for radioiodine therapy of differentiated thyroid cancer," *Eur. J. Nucl. Med. Mol. Imaging*, vol. 35, no. 10, pp. 1941–1959, Oct. 2008, doi: 10.1007/s00259-008-0883-1.
- [118] J. S. Kim, "Combination Radioimmunotherapy Approaches and Quantification of Immuno-PET," *Nucl. Med. Mol. Imaging (2010)*, vol. 50, no. 2, pp. 104–111, Jun. 2016, doi: 10.1007/s13139-015-0392-7.
- [119] F. Kraeber-Bodere, J. Barbet, and J.-F. Chatal, "Radioimmunotherapy: From Current Clinical Success to Future Industrial Breakthrough?," *J. Nucl. Med.*, vol. 57, no. 3, pp. 329–331, Mar. 2016, doi: 10.2967/jnumed.115.167247.
- [120] S. M. Larson, J. A. Carrasquillo, N.-K. V. Cheung, and O. W. Press, "Radioimmunotherapy of human tumours," *Nat. Rev. Cancer*, vol. 15, no. 6, pp. 347–360, Jun. 2015, doi: 10.1038/nrc3925.
- [121] S. H. L. Frost *et al.*, "Comparison of ^{211}At -PRIT and ^{211}At -RIT of Ovarian Microtumors in a Nude Mouse Model," *Cancer Biother. Radiopharm.*, vol. 28, no. 2, pp. 108–114, Mar. 2013, doi: 10.1089/cbr.2012.1281.
- [122] J. Zaheer, H. Kim, Y.-J. Lee, J. S. Kim, and S. M. Lim, "Combination Radioimmunotherapy Strategies for Solid Tumors," *Int. J. Mol. Sci.*, vol. 20, no. 22, p. 5579, Nov. 2019, doi: 10.3390/ijms20225579.
- [123] A. Yordanova *et al.*, "Theranostics in nuclear medicine practice," *Onco. Targets. Ther.*, vol. Volume 10, pp. 4821–4828, Oct. 2017, doi: 10.2147/OTT.S140671.
- [124] S. S. Kelkar and T. M. Reineke, "Theranostics: Combining Imaging and Therapy," *Bioconjug. Chem.*, vol. 22, no. 10, pp. 1879–1903, Oct. 2011, doi: 10.1021/bc200151q.

- [125] M. Pacilio *et al.*, “Dosimetry of bone metastases in targeted radionuclide therapy with alpha-emitting ^{223}Ra -dichloride,” *Eur. J. Nucl. Med. Mol. Imaging*, vol. 43, no. 1, pp. 21–33, Jan. 2016, doi: 10.1007/s00259-015-3150-2.
- [126] L. Mango, “Theranostics: A Unique Concept to Nuclear Medicine,” *Arch. Cancer Sci. Ther.*, vol. 1, no. 1, pp. 001–004, Feb. 2017, doi: 10.29328/journal.hjcsr.1001001.
- [127] ICRP, 2008. “Nuclear Decay Data for Dosimetric Calculations,” *ICRP Publication 107. Ann. ICRP 38* (3).
- [128] ICRP, 2006. “Human Alimentary Tract Model for Radiological Protection,” *ICRP Publication 100. Ann. ICRP 36* (1-2).
- [129] ICRP, 2016. “The ICRP computational framework for internal dose assessment for reference adults: specific absorbed fractions,” *ICRP Publication 133. Ann. ICRP 45*(2), 1–74.
- [130] A.S. Mollah, M.R. Quddus, and S.M. Iqbal “Internal radiation dose assessment in nuclear medicine practices by using locally developed IRDE software,” *Bangladesh J. Nucl. Med.*, vol. 21, no. 1, pp. 26–30, 2018.
- [131] S. Lamart, L. de Carlan, E. Blanchardon, and D. Franck, “Automatic application of ICRP biokinetic models in voxel phantoms for in vivo counting and internal dose assessment,” *Radiat. Prot. Dosimetry*, vol. 127, no. 1–4, pp. 240–244, Jun. 2007, doi: 10.1093/rpd/ncm345.
- [132] C. L. D. Villoing, “NCINM: a computational phantom-based dosimetry tool for patients undergoing nuclear medicine procedures,” *J. Nucl. Med.*, vol. 60, no. 1, p. 1634, 2019, [Online]. Available: http://jnm.snmjournals.org/content/60/supplement_1/1634.
- [133] N. S. Jarvis and A. Birchall, “LUDEP 1.0, A Personal Computer Program to Implement the New ICRP Respiratory Tract Model,” *Radiat. Prot. Dosimetry*, vol. 53, no. 1–4, pp. 191–193, May 1994, doi: 10.1093/oxfordjournals.rpd.a082274.
- [134] M. G. Stabin, R. B. Sparks, and E. Crowe, “OLINDA/EXM: the second-generation personal computer software for internal dose assessment in nuclear medicine,” *J. Nucl. Med.*, vol. 46, no. 6, pp. 1023–7, Jun. 2005, [Online]. Available: <http://www.ncbi.nlm.nih.gov/pubmed/15937315>.
- [135] M. Andersson, L. Johansson, D. Minarik, S. Mattsson, and S. Leide-Svegborn, “An internal radiation dosimetry computer program, IDAC 2.0, for estimation of patient doses from radiopharmaceuticals,” *Radiat. Prot. Dosimetry*, vol. 162, no. 3, pp. 299–305, Dec. 2014, doi: 10.1093/rpd/nct337.
- [136] W. Rühm *et al.*, “Dose-rate effects in radiation biology and radiation

- protection,” *Ann. ICRP*, vol. 45, no. 1_suppl, pp. 262–279, Jun. 2016, doi: 10.1177/0146645316629336.
- [137] ICRP, 2012, “ICRP Statement on Tissue Reactions / Early and Late Effects of Radiation in Normal Tissues and Organs – Threshold Doses for Tissue Reactions in a Radiation Protection Context,” *ICRP Publication 118. Ann. ICRP 41(1/2)*.
- [138] International Commission on Radiation Units and Measurements (ICRU), “ICRU Report 85a - Fundamental Quantities And Units For Ionizing Radiation (Revised),” *J. ICRU*, 2011.
- [139] W. E. Bolch, K. F. Eckerman, G. Sgouros, and S. R. Thomas, “MIRD Pamphlet No. 21: A Generalized Schema for Radiopharmaceutical Dosimetry-Standardization of Nomenclature,” *J. Nucl. Med.*, vol. 50, no. 3, pp. 477–484, Feb. 2009, doi: 10.2967/jnumed.108.056036.
- [140] P. B. Zanzonico, “Internal radionuclide radiation dosimetry: a review of basic concepts and recent developments,” *J. Nucl. Med.*, vol. 41, no. 2, pp. 297–308, Feb. 2000, [Online]. Available: <http://www.ncbi.nlm.nih.gov/pubmed/10688115>.
- [141] G. L. DeNardo, M. E. Juweid, C. A. White, G. A. Wiseman, and S. J. DeNardo, “Role of radiation dosimetry in radioimmunotherapy planning and treatment dosing,” *Crit. Rev. Oncol. Hematol.*, vol. 39, no. 1–2, pp. 203–218, Aug. 2001, doi: 10.1016/S1040-8428(01)00109-3.
- [142] D. R. Fisher, “Internal dosimetry for systemic radiation therapy,” *Semin. Radiat. Oncol.*, vol. 10, no. 2, pp. 123–132, Apr. 2000, doi: 10.1016/S1053-4296(00)80049-1.
- [143] M. G. Stabin, “Developments in the internal dosimetry of radiopharmaceuticals,” *Radiat. Prot. Dosimetry*, vol. 105, no. 1–4, pp. 575–580, Jul. 2003, doi: 10.1093/oxfordjournals.rpd.a006306.
- [144] D. K. Kontogeorgakos, P. A. Dimitriou, G. S. Limouris, and L. J. Vlahos, “Patient-specific dosimetry calculations using mathematic models of different anatomic sizes during therapy with ^{111}In -DTPA-D-Phe1-octreotide infusions after catheterization of the hepatic artery,” *J. Nucl. Med.*, vol. 47, no. 9, pp. 1476–82, Sep. 2006, [Online]. Available: <http://www.ncbi.nlm.nih.gov/pubmed/16954556>.
- [145] X. G. Xu and K. F. Eckerman, Eds., *Handbook of Anatomical Models for Radiation Dosimetry*. CRC Press, 2009.
- [146] W. S. Snyder, M. R. Ford, G. G. Warner, *et al.*, “Tabulation of dose equivalent per microcurie-day for source and target organs of an adult for various radionuclides,” Oak Ridge, TN (United States), Nov. 1975. doi: 10.2172/4182057.

- [147] M. Cristy and K. F. Eckerman, "Specific absorbed fractions of energy at various ages from internal photon sources: 3, Five-year-old," Oak Ridge, TN (United States), Apr. 1987. doi: 10.2172/6263443.
- [148] ICRP, 1975. "Report of the Task Group on Reference Man," *ICRP Publication 23*. Pergamon Press, Oxford.
- [149] W. P. Segars, G. Sturgeon, S. Mendonca, J. Grimes, and B. M. W. Tsui, "4D XCAT phantom for multimodality imaging research," *Med. Phys.*, vol. 37, no. 9, pp. 4902–4915, Aug. 2010, doi: 10.1118/1.3480985.
- [150] I. G. Zubal, C. R. Harrell, E. O. Smith, Z. Rattner, G. Gindi, and P. B. Hoffer, "Computerized three-dimensional segmented human anatomy," *Med. Phys.*, vol. 21, no. 2, pp. 299–302, Feb. 1994, doi: 10.1118/1.597290.
- [151] I. Clairand, L. G. Bouchet, M. Ricard, M. Durigon, M. Di Paola, and B. Aubert, "Improvement of internal dose calculations using mathematical models of different adult heights," *Phys. Med. Biol.*, vol. 45, no. 10, pp. 2771–2785, Oct. 2000, doi: 10.1088/0031-9155/45/10/304.
- [152] N. Petoussi-Henss, M. Zankl, U. Fill, and D. Regulla, "The GSF family of voxel phantoms," *Phys. Med. Biol.*, vol. 47, no. 1, pp. 89–106, Jan. 2002, doi: 10.1088/0031-9155/47/1/307.
- [153] M. Caon, "Voxel-based computational models of real human anatomy: a review," *Radiat. Environ. Biophys.*, vol. 42, no. 4, pp. 229–235, Feb. 2004, doi: 10.1007/s00411-003-0221-8.
- [154] M. Zankl, J. Becker, U. Fill, N. Petoussi-Henss, and K. F. Eckerman, "GSF male and female adult voxel models representing ICRP reference man - The present status," in *Monte Carlo 2005 Topical Meeting*, 2005.
- [155] "US-Joint Reassessment of Atomic Bomb Radiation Dosimetry in Hiroshima and Nagasaki (DS86)," *Nature*, Jul. 2003, doi: 10.1038/news030728-8.
- [156] K. Saito *et al.*, "Construction of a computed tomographic phantom for a Japanese male adult and dose calculation system," *Radiat. Environ. Biophys.*, vol. 40, no. 1, pp. 69–76, Mar. 2001, doi: 10.1007/s004110000082.
- [157] K. Saito, S. Koga, Y. Ida, T. Kamei, and J. Funabiki, "Construction of a Voxel Phantom Based on CT Data for a Japanese Female Adult and Its Use for Calculation of Organ Doses from External Electrons," *Japanese J. Heal. Phys.*, vol. 43, no. 2, pp. 122–130, 2008, doi: 10.5453/jhps.43.122.
- [158] K. Sato, H. Noguchi, Y. Emoto, S. Koga, and K. Saito, "Japanese adult male voxel phantom constructed on the basis of CT images," *Radiat. Prot. Dosimetry*, vol. 123, no. 3, pp. 337–344, Feb. 2007, doi: 10.1093/rpd/nci101.
- [159] K. Sato, H. Noguchi, Y. Emoto, S. Koga, and K. Saito, "Development of a Japanese Adult Female Voxel Phantom," *J. Nucl. Sci. Technol.*, vol. 46, no.

- 9, pp. 907–913, Sep. 2009, doi: 10.1080/18811248.2009.9711599.
- [160] ICRP, 1991. “1990 Recommendations of the International Commission on Radiological Protection,” *ICRP Publication 60. Ann. ICRP 21 (1-3)*.
 - [161] J. T. Bushberg, J. A. Seibert, E. M. Leidholdt, J. M. Boone, and E. J. Goldschmidt, “The Essential Physics of Medical Imaging,” *Med. Phys.*, vol. 30, no. 7, pp. 1936–1936, Jul. 2003, doi: 10.1118/1.1585033.
 - [162] A. Hata *et al.*, “Effect of Matrix Size on the Image Quality of Ultra-high-resolution CT of the Lung,” *Acad. Radiol.*, vol. 25, no. 7, pp. 869–876, Jul. 2018, doi: 10.1016/j.acra.2017.11.017.
 - [163] Oxford University, “Home: Oxford English Dictionary,” *Oxford University Press*. 2005, Accessed: Jun. 06, 2020. [Online]. Available: <https://www.oed.com/>.
 - [164] ICRP, 1977. “Recommendations of the ICRP,” *ICRP Publication 26. Ann. ICRP 1 (3)*.
 - [165] ICRP, 2015. “Radiation Dose to Patients from radiopharmaceuticals: A Compendium of Current Information Related to Frequently Used Substances,” *ICRP Publication 128. Ann. ICRP 44(2S)*.
 - [166] “Tc-99m pertechnetate | Radiology Reference Article | Radiopaedia.org.” <https://radiopaedia.org/articles/tc-99m-pertechnetate?lang=us> (accessed Jun. 06, 2020).
 - [167] K. F. Eckerman, R. W. Leggett, M. Cristy, *et al.*, “User’s Guide to the DCAL System,” Oak Ridge (USA), 2006. [Online]. Available: <https://www.epa.gov/sites/production/files/2015-02/documents/dcal-manual.pdf>.
 - [168] K.F. Eckerman, *et al.*, “Federal Guidance Report No. 12,” 1993.
 - [169] ICRP, 1988. “Radiation Dose to Patients from Radiopharmaceuticals,” *ICRP Publication 53. Ann. ICRP 18 (1-4)*.
 - [170] ICRP, 1992. “Radiological Protection in Biomedical Research,” *ICRP Publication 62. Ann. ICRP 22 (3)*.
 - [171] ICRP, 1998. “Radiation Dose to Patients from Radiopharmaceuticals (Addendum to ICRP Publication 53),” *ICRP Publication 80. Ann. ICRP 28 (3)*.
 - [172] ICRP, 2008. “Radiation Dose to Patients from Radiopharmaceuticals - Addendum 3 to ICRP Publication 53,” *ICRP Publication 106. Ann. ICRP 38 (1-2)*.
 - [173] ICRP, 2019. “Radiological protection in therapy with radiopharmaceuticals,” *ICRP Publication 140. Ann. ICRP 48(1)*.

- [174] K. J. Kearfott, "ICRU Report 67: Absorbed-Dose Specification in Nuclear Medicine," *Health Phys.*, vol. 85, no. 1, p. 113, Jul. 2003, doi: 10.1097/00004032-200307000-00023.
- [175] "Internal Radiation Dose in Diagnostic Nuclear Medicine HD Roedler, A Kaul, GJ Hine. Berlin, Verlag H. Hoffmann, 1978. US distribution: Verlag H. Hoffmann, 961 Gapter Road, Boulder, CO 80303," *J. Nucl. Med.*, vol. 20, no. 7, pp. 812–812, 1979.
- [176] A. R. Benedetto, "NCRP Report No. 70, Nuclear Medicine-Factors Influencing the Choice and Use of Radionuclides in Diagnosis and Therapy by National Council on Radiation Protection and Measurements," *Med. Phys.*, vol. 10, no. 5, pp. 721–721, Sep. 1983, doi: 10.1118/1.595414.
- [177] L. Johansson, S. Mattsson, B. Nosslin, and S. Leide-Svegborn, "Effective dose from radiopharmaceuticals," *Eur. J. Nucl. Med.*, vol. 19, no. 11, Nov. 1992, doi: 10.1007/BF00175858.
- [178] ARSAC, "Notes for guidance on the clinical administration of radiopharmaceuticals and use of sealed radioactive sources. Administration of Radioactive Substances Advisory Committee.," *Nucl. Med. Commun.*, vol. 21 Suppl, pp. S1-93, Jan. 2000, [Online]. Available: <http://www.ncbi.nlm.nih.gov/pubmed/10732169>.
- [179] "RADAR Home." <http://www.doseinfo-radar.com/RADARHome.html> (accessed Jun. 06, 2020).
- [180] C. S. Adcock, E. Florez, K. A. Zand, A. Patel, C. M. Howard, and A. Fatemi, "Assessment of Treatment Response Following Yttrium-90 Transarterial Radioembolization of Liver Malignancies," *Cureus*, Jun. 2018, doi: 10.7759/cureus.2895.
- [181] C. Müller *et al.*, "Preclinical investigations and first-in-human application of ¹⁵²Tb-PSMA-617 for PET/CT imaging of prostate cancer," *EJNMMI Res.*, vol. 9, no. 1, p. 68, Dec. 2019, doi: 10.1186/s13550-019-0538-1.
- [182] N. Gracheva *et al.*, "Production and characterization of no-carrier-added ¹⁶¹Tb as an alternative to the clinically-applied ¹⁷⁷Lu for radionuclide therapy," *EJNMMI Radiopharm. Chem.*, vol. 4, no. 1, p. 12, Dec. 2019, doi: 10.1186/s41181-019-0063-6.
- [183] C. Müller *et al.*, "Terbium-161 for PSMA-targeted radionuclide therapy of prostate cancer," *Eur. J. Nucl. Med. Mol. Imaging*, vol. 46, no. 9, pp. 1919–1930, Aug. 2019, doi: 10.1007/s00259-019-04345-0.
- [184] N. J. M. Klaassen, M. J. Arntz, A. Gil Arranja, J. Roosen, and J. F. W. Nijssen, "The various therapeutic applications of the medical isotope holmium-166: a narrative review," *EJNMMI Radiopharm. Chem.*, vol. 4, no. 1, p. 19, Dec. 2019, doi: 10.1186/s41181-019-0066-3.

- [185] R. C. Bakker *et al.*, “Intratumoral injection of radioactive holmium-166 microspheres in recurrent head and neck squamous cell carcinoma,” *Nucl. Med. Commun.*, vol. 39, no. 3, pp. 213–221, Mar. 2018, doi: 10.1097/MNM.0000000000000792.
- [186] ICRP, 2012. “Compendium of Dose Coefficients based on ICRP Publication 60,” *ICRP Publication 119. Ann. ICRP 41(Suppl.)*.
- [187] J. Gustafsson, G. Brolin, M. Cox, M. Ljungberg, L. Johansson, and K. S. Gleisner, “Uncertainty propagation for SPECT/CT-based renal dosimetry in ¹⁷⁷Lu peptide receptor radionuclide therapy,” *Phys. Med. Biol.*, vol. 60, no. 21, pp. 8329–8346, Nov. 2015, doi: 10.1088/0031-9155/60/21/8329.
- [188] H. D. Roedler, “Accuracy of internal dose calculations with special consideration of radiopharmaceutical biokinetics,” *Int. J. Nucl. Med. Biol.*, vol. 10, no. 1, pp. 37–38, Jan. 1983, doi: 10.1016/0047-0740(83)90032-3.
- [189] K. Norrgren, S. L. Svegborn, J. Areberg, and S. Mattsson, “Accuracy of the Quantification of Organ Activity from Planar Gamma Camera Images,” *Cancer Biother. Radiopharm.*, vol. 18, no. 1, pp. 125–131, Feb. 2003, doi: 10.1089/108497803321269403.
- [190] M. G. Stabin, “Uncertainties in Internal Dose Calculations for Radiopharmaceuticals,” *J. Nucl. Med.*, vol. 49, no. 5, pp. 853–860, Apr. 2008, doi: 10.2967/jnumed.107.048132.
- [191] M. Andersson, S. Mattsson, L. Johansson, and S. Leide-Svegborn, “A biokinetic and dosimetric model for ionic indium in humans,” *Phys. Med. Biol.*, vol. 62, no. 16, pp. 6397–6407, Jul. 2017, doi: 10.1088/1361-6560/aa779f.
- [192] S. Hashimoto and T. Sato, “Estimation method of systematic uncertainties in Monte Carlo particle transport simulation based on analysis of variance,” *J. Nucl. Sci. Technol.*, vol. 56, no. 4, pp. 345–354, Apr. 2019, doi: 10.1080/00223131.2019.1585989.
- [193] B. P. Chu, “Safety Reports Series No. 63, Release of Patients After Radionuclide Therapy,” *Health Phys.*, vol. 104, no. 1, p. 117, Jan. 2013, doi: 10.1097/HP.0b013e31826f551f.
- [194] IAEA, “International Basic Safety Standards for Protection against Ionizing Radiation and for the Safety of Radiation Sources,” Vienna, 1996.
- [195] ICRP, 2007. “Radiation Protection in Medicine,” *ICRP Publication 105. Ann. ICRP 37 (6)*.
- [196] National Council on Radiation Protection and Measurements, “Management of Radionuclide Therapy Patients,” MD, 2006.
- [197] J. A. Siegel, C. S. Marcus, and R. B. Sparks, “Calculating the absorbed dose

- from radioactive patients: the line-source versus point-source model.,” *J. Nucl. Med.*, vol. 43, no. 9, pp. 1241–4, Sep. 2002, [Online]. Available: <http://www.ncbi.nlm.nih.gov/pubmed/12215565>.
- [198] J. A. Siegel and R. B. Sparks, “Radioactivity Appearing at Landfills in Household Trash of Nuclear Medicine Patients: Much Ado About Nothing?,” *Health Phys.*, vol. 82, no. 3, pp. 367–372, Mar. 2002, doi: 10.1097/00004032-200203000-00009.
 - [199] E. Lubin, “Definitive improvement in the approach to the treated patient as a radioactive source,” *Journal of Nuclear Medicine*, vol. 43, no. 3, pp. 364–365, 2002.
 - [200] National Council on Radiation Protection and Measurements, “Dose Limits for Individuals Who Receive Exposure from Radionuclide Therapy Patients,” MD, 1995.
 - [201] S. Mattsson and C. Bernhardsson, “Release of Patients After Radionuclide Therapy: Radionuclide Releases to the Environment from Hospitals and Patients,” in *Radiation Protection in Nuclear Medicine*, Berlin, Heidelberg: Springer Berlin Heidelberg, 2013, pp. 139–148.
 - [202] ICRP, 2004. “Release of Patients after Therapy with Unsealed Radionuclides,” *ICRP Publication 94. Ann. ICRP 34 (2)*.
 - [203] ICRU, “Report 39,” *J. Int. Comm. Radiat. Units Meas.*, vol. os20, no. 2, p. NP-NP, Feb. 1985, doi: 10.1093/jicru/os20.2.Report39.
 - [204] ICRP, 2015. “Occupational Intakes of Radionuclides: Part 1,” *ICRP Publication 130. Ann. ICRP 44(2)*.
 - [205] ICRP, 2016. “Occupational Intakes of Radionuclides: Part 2,” *ICRP Publication 134. Ann. ICRP 45(3/4), 1–352*.
 - [206] ICRP, 2017. “Occupational Intakes of Radionuclides: Part 3,” *ICRP Publication 137. Ann. ICRP 46(3/4)*.
 - [207] ICRP, 2019. “Occupational Intakes of Radionuclides: Part 4,” *ICRP Publication 141. Ann. ICRP 48(2/3)*.
 - [208] A. Birchall *et al.*, “IMBA Professional Plus: a flexible approach to internal dosimetry,” *Radiat. Prot. Dosimetry*, vol. 125, no. 1–4, pp. 194–197, Dec. 2006, doi: 10.1093/rpd/ncl171.
 - [209] N. Ishigure, “Development of software for internal dose calculation from bioassay measurements,” *Radiat. Prot. Dosimetry*, vol. 109, no. 3, pp. 235–242, Jul. 2004, doi: 10.1093/rpd/nch048.
 - [210] K. Manabe, K. Sato, and F. Takahashi, “Estimating internal dose coefficients of short-lived radionuclides in accordance with ICRP 2007

recommendations,” *J. Nucl. Sci. Technol.*, vol. 56, no. 5, pp. 385–393, May 2019, doi: 10.1080/00223131.2019.1585988.

- [211] WHO, “Health risk assessment from the nuclear accident after the 2011 Great East Japan earthquake and tsunami, based on a preliminary dose estimation,” 2013. [Online]. Available: https://apps.who.int/iris/bitstream/handle/10665/78218/9789241505130_eng.pdf;jsessionid=BAD5BCF73244D49609AD264646F3C385?sequence=1.
- [212] J. L. Humm, R. W. Howell, and D. V. Rao, “Dosimetry of Auger-electron-emitting radionuclides: Report No. 3 of AAPM Nuclear Medicine Task Group No. 6,” *Med. Phys.*, vol. 21, no. 12, pp. 1901–1915, Dec. 1994, doi: 10.1118/1.597227.

Acknowledgements

This work was carried out at the Watanabe-Kin laboratory, Department of Advanced Energy Engineering Science (AEES), Interdisciplinary Graduate School of Engineering Sciences (IGSES), Kyushu University, under the supervision of Associate Professor Tadahiro KIN. I would like to express a lot of thanks to many people for their help in the present work.

First and foremost, I would like to express my sincere gratitude to my supervisor, Associate Professor Tadahiro KIN. Without his guidance and persistent help, this thesis would not have been possible. I have learned a lot from him not only nuclear and radiation physics itself but also logical thinking and sincere attitude towards physics, engineering, and scientific research. His comments and supports are always valuable and precious.

I am greatly thankful to my research advisor, Professor Yukinobu WATANABE. He has strongly afforded to help me throughout the years of my studies. Without him, this work would not be possible to complete. I always appreciate his kindness and supports.

My great thanks are also expressed to Professor Keisuke MAEHATA and Associate Professor Kazunari KATAYAMA for careful reading of this thesis and valuable comments. I am grateful to these professors for developing my understanding of many important parts of this thesis.

It has been a great pleasure for me to work together with RI group members. With Mr. Katsumi Aoki, Mr. Masaya Yamaguchi, Mrs. Mikhail Mary Alfonse George, Mr. Masaki Kamida, Mr. Kosuke Yoshinami, Mr. Naoto Araki, and all members of the RI group, we are the great team-work who always work hard together to perform this research enjoyable. They have not hesitated in training and helping me when I needed it.

Furthermore, I would like to thank all other members studied in the Watanabe-Kin laboratory for their warmhearted help, especially, Assistant Professor Shoichiro Kawase, Dr. Keita Nakano, Ms. Hikaru Sato, Mr. Seiya Manabe, Mr. Shunsuke Sato, Mr. Hayato Takeshita, Mr. Junya Kuroda, Mr. Tomohiro Komori, Mr. Keiichirou Shiokawa, Mr. Takumi Mahara, Ms. Miyuki Uematsu, Mr. Naoya Okamoto, Mr. Yuji Shinjo, Mr. Yu Horai, Mr. Tatsuhiko Miyatake, Mr. Takuya Murota, Ms. Misaki Saitsu, Mr. Ryohei Takahashi, and Mr. Hiroya Fukuda, and also Ms. Kullapha, Mr. Nagata, Mr. Naoki Yamaguchi. My thanks are also given to Ms. Rumiko Koga and Ms. Megumi Ogami for their help with office work.

I would like to thank Mr. Masateru HAYASHI, Dr. Azumu, Dr. Makoto SASANO, and all group members of the Advanced Sensing Technology Group of

Mitsubishi Electric Corporation for their great hospitality during my stay in Mitsubishi Electric Corporation at the time of my industrial internship.

I also wish to thank the Kyushu university Intellectual Exchange and Innovation Program (IEI Program) organizer to make a scope to join in the Ph. D. program and the International Student support center Chikushi campus, AEES departmental office staff for their tireless help in many aspects related to my study.

I gratefully acknowledge the Japanese Government (Monbukagakusho: MEXT) Scholarship for their financial support to complete my study. I would like to pay my gratitude to all Japanese taxpayers for their eternal contribution to this financial support.

I want to thank the authority of Comilla University (CoU), Bangladesh, and my colleagues in the Department of Physics of CoU for official support in study leave purposes.

My great thanks expressed to my parents, wife, family, and friends to support me with their love. They are the source of my motivation and power. Without their supports, I could not finish this work.

Finally, it is a pleasure to express my gratitude to everyone who supports me to complete this thesis.